Günther Bauer · Wolfgang Richter (Eds.)

Optical Characterization of Epitaxial Semiconductor Layers

With 271 Figures

Springer

Contents

6. High Resolution X-Ray Diffraction

Alois Krost, Günther Bauer, Joachim Woitok

Conventional high resolution X-Ray diffraction has been developed into a powerful tool for the nondestructive *ex-situ* investigation of epitaxial layers, of heterostructures and superlattice systems:
The information which is obtained from diffraction patterns concerns the composition and uniformity of epitaxial layers, their thicknesses, the built-in strain and strain relaxation, and the crystalline perfection related to their dislocation density. Furthermore information on interfaces like interdiffusion and intermixingis obtained under certain circumstances as well. For the analysis of the diffraction patterns from epilayers, heterostructures and multilayers, the kinematical diffraction theory, although being still useful for a quick inspection of the data, in general can no longer be used for the quantitative description of the experiments. Instead dynamical theory is applied which takes into account extinction, multiple scattering, and the slight deviation of the refractive index from one.
The instrumentation has also been improved continuously and simple powder diffractometers using a focussing path for the X-Rays were replaced by double- and triple -axis spectrometers equipped with multiple crystal or channel cut monochromators and analyzers. Apart from investigations under normal Bragg conditions grazing angle incidence techniques both for the determination of layer thicknesses as well as for precise information on lattice constants of thin films have also been employed. X-Ray topography is used for imaging purposes of layers grown on large wafers.

There are a number of excellent reviews on the analysis of epitaxial layers by X-Ray diffraction: In the early reviews by Segmüller and Murakami [6.1] and Paine [6.2] the various diffractometer methods are described whereas in the most extensive one [6.3] the emphasis is on the mathematical description of the strain state of epitaxial layers, of inhomogeneous strain on periodic multilayers as well as on grazing incidence techniques. For the latter technique the latest developments are summarised by Segmüller [6.4] and Schiller et al. [6.5]. Tanner [6.6, 6.7] and Halliwell [6.8] highlight the Double-Crystal Diffractometer (DCD) for the analysis of thicknesses and strains of epitaxial layers whereas Fewster [6.9–6.11] describes the advantage of triple-axis spectrometers. Picraux et al. and Ryan et al. [6.13] gave a complete survey of the amount of information which can be extracted from high resolution X-Ray diffraction (HRXRD) including especially reciprocal lattice scans and the use of triple axis spectrometers whereas Wie [6.14] focus on the characterization of heterostructure interfaces and the analysis of diffuse scattering in the Bragg diffraction geometry. A summary of most recent developments can also be found in [6.15, 6.16].

In the first Section an overview on basic scattering geometries and advanced instrumentation which is nowadays commercially available is given. It follows a Section on kinematical and dynamical theory. The dependence of Bragg reflection intensities on thicknesses is described in Sect. 6.3 and in Sect. 6.4 strain phenomena and partial relaxation of strain are discussed. The application of HRXRD to single heterostructures is treated in Sect. 6.5 and the topic of Sect. 6.6 are multilayers including Ewald sphere constructions for the interpretation of DCD diffractograms, interdiffusion, lattice plane tilts, terracing and mosaic spread. The triple axis spectrometers have led to extensive studies of layers and multilayers through scans in the reciprocal lattice (Sect. 6.7). Further new developments like the analysis of periodic quantum wires or dots and the real time X-Ray diffraction for strain relaxation phenomena and growth processes are described in Sect. 6.8. The three final Sections are devoted to grazing incidence techniques including specular and anomalous reflection as well. Grazing incidence diffraction (GID) is a surface sensitive method which yields information on film properties parallel to surfaces or interfaces and achieves even monolayer sensitivity. New developments include also a contribution of high resolution X-Ray diffraction to topography for the analysis of layers on wafers. We refer to a recent review by Köhler [6.18] on this topic. Both the spectrometric tools as well as the crystalline quality of the materials investigated have reached fantastic limits already in the early 1970s: i.e. the full width at half maximum (*FWHM*) of a Si (422) asymmetric Bragg reflection corresponds to 0.16" [6.17]. In order to perform such a measurement an experimental resolution of 0.016" is required. Such an accuracy corresponds e.g. to an angular position of the earth on its orbit around the sun between two positions which are 3.7 km apart from each other. (The mean distance earth - sun is $1.5 \cdot 10^8$ km).

X-Ray standing wave technique which is especially interesting for surface and interface analysis, since the position of atoms which are either adsorbed or being constituents of thin epilayers can be determined with high accuracy is not presented here. A comprehensive review on this field is given by Malgrange and Ferret [6.19].

New instrumentation and the possibility to use high intensity synchrotron sources will lead in the near future to new *in-situ* applications as well as to transmission spectroscopy (Laue case) of HRXRD. However, the main purpose of this review is the demonstration of methods and results obtained on epitaxial systems with up to date but conventional laboratory instrumentation.

6.1 Principal Scattering Geometries

In this Section basic scattering geometries and advanced instrumentations are described such as double-crystal diffraction, triple-axis spectrometers etc.

6.1.1 $\omega - 2\Theta$-Scan and ω-Scan (Rocking-curve)

Any measurement of lattice spacing is in principle determined by Bragg's law [6.20]

$$2d_{hkl} \cdot \sin\Theta_B = n\lambda \tag{6.1}$$

where d_{hkl} is the spacing of lattice planes with Miller indices (hkl) and Θ_B is the corresponding Bragg angle. This equation follows from kinematic diffraction theory and neglects the fact that the refractive index of matter for X-Rays is less than 1 by a few parts in 10^{-6} and so the incident beam is refracted to an internal angle slightly smaller than the external one. In Fig. 6.1 the scattering geometry is shown. φ denotes the angle between the lattice plane (hkl) and the surface, $\mathbf{k}_i$ is the incident and $\mathbf{k}_s$ the scattered wavevector. In principle, the electric vector of the incident beam can be polarised perpendicularly (σ) or parallel (π) with respect to the incident plane.

The Bragg diffraction is called "symmetric" if $\varphi = 0$, i.e. the reflecting lattice planes are parallel to the surface. For $\varphi \neq 0$ the Bragg diffraction is defined as "asymmetric". The asymmetry factor is given by:

$$b = \frac{\gamma_i}{\gamma_s} = -\frac{\sin(\omega_+)}{\sin(\omega_-)} = -\frac{\sin(\Theta + \varphi)}{\sin(\Theta - \varphi)} \tag{6.2}$$

where γ_i and γ_s are the direction cosines of the incident (i) and scattered (s) wave with respect to the surface normal (o).

The corresponding Ewald sphere construction is shown in Fig. 6.2. $\mathbf{G}_{hkl}$ denotes the reciprocal lattice vector and ω is the angle between the incident

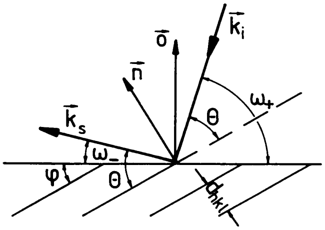

Fig. 6.1. Scattering geometry. $\mathbf{k}_i$: incident wavevector, $\mathbf{k}_s$: scattered wavevector, $\mathbf{o}$: surface normal, $\mathbf{n}$: normal on reflecting planes, Θ : Bragg-angle, φ : angle between surface and reflecting plane

wavevector $\mathbf{k}_i$ and the surface plane:

$$\mathbf{k}_s = \mathbf{k}_i + \mathbf{G}_{hkl} \tag{6.3}$$

In Fig. 6.2 two possible scans for measuring the intensity of a Bragg reflection due to the reciprocal lattice point (hkl) are indicated:

(i) conventional powder diffractometers use a "$\Theta - 2\Theta$"-scan for measuring symmetric Bragg reflections ($\varphi = 0, \omega^+ = \omega^- = \omega = \Theta$). For such a scan, the detector is rotated twice as fast and in the same direction around the diffractometer axis as the sample. In reciprocal space, this conventional motion of sample and detector corresponds to a change of $\mathbf{k}_s$ in the following way: the tip of the vector $\mathbf{k}_s$ moves along the reciprocal lattice vector $\mathbf{G}_{hkl}$. During this motion the angle ω between the incident beam and the sample surface changes. For asymmetric (hkl) Bragg reflections ($\omega = \Theta \pm \varphi$), +: corresponds to the high incidence and − to the low incidence) the corresponding $\omega - 2\Theta$ scan direction runs also radial from the origin (000) of the reciprocal space along $\mathbf{G}_{hkl}$ (Fig. 6.2a).

(ii) In the ω-scan, the detector is fixed in position with wide open entrance slits and the sample is rotated, i.e. ω changes. In reciprocal space, this corresponds to a path as indicated in Fig. 6.2b by the bold arrow. The scan direction is transversal in reciprocal space. Thus the so-called rocking-curve is obtained.

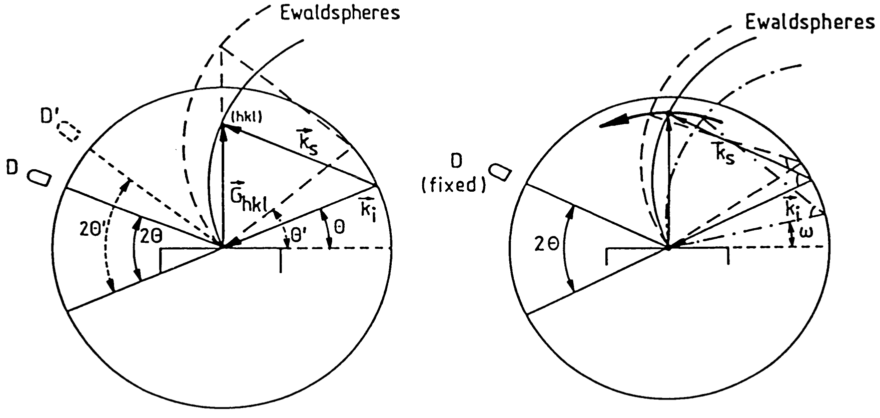

Fig. 6.2a. Ewald sphere construction (for symmetric reflections, i.e. reflecting planes are parallel to the surface) for the $\omega - 2\Theta$-scan geometry. Θ: angle between incident X-Rays and surface plane, $\mathbf{G}_{hkl}$: reciprocal lattice vector, (hkl): reciprocal lattice point, D: detector (on diffractometer circle in real space), **b** Ewald sphere construction for an ω-scan, the bold arrow indicates the movement in the reciprocal lattice

In Figs. 6.2a,b both the diffractometer circle (real space) as well as Ewald-spheres (reciprocal space) are shown. As can be seen, the two scan directions are perpendicular to each other. In contrast to a conventional focussing setup, e.g. Bragg-Brentano-, Seeman Bohlin-, Johanson-, etc. -configuration (e.g. [6.1,6.21]), the sample is illuminated by an intentionally perfect parallel beam.

The practical resolution of lattice constant determination of a perfect crystal is $\Delta d/d = 10^{-5}$. In epitaxial systems typically lattice constant variations between 10^{-2} and 10^{-4} have to be measured. The corresponding angular changes $\Delta\theta$ in the Bragg angle follow from the differentiation of Bragg's law:

$$\frac{\Delta d}{d} = \frac{\Delta\lambda}{\lambda} - \frac{\Delta\Theta}{\tan\Theta} \tag{6.4}$$

For high precision measurements of lattice constants and strains, the sample and X-Ray spectrometer should be temperature stabilised. In Table 6.1 we give some characteristic values which impose practical limitations on resolution:

Table 6.1. Characteristic examples and values for spectral resolution in X-Ray Diffraction (XRD) [6.22]

lattice perfection	$\Delta d/d \geq 10^{-7}$
thermal expansion coefficient	$\alpha = 10^{-6}K^{-1}$
X-Ray reflection (Fig. 6.10)	$\Delta\theta = 2'' \approx 10^{-5}$
line width of Cu$K_{\alpha 1}$ radiation	$\Delta\lambda/\lambda = 3 \cdot 10^{-4}$
separation Cu$K_{\alpha 1} - K_{\alpha 2}$	$\Delta\lambda/\lambda = 2.5 \cdot 10^{-3}$
single-crystal diffractometer with slit collimator	$\Delta\theta = 0.1° \approx 10^{-2}$

6.1.2 Double-Crystal Diffraction

In order to measure the X-Ray reflection of a single crystalline bulk sample as a function of the angle ω (the so-called "rocking-curve") the wavelength spread $\Delta\lambda$ has to be minimized. The method most often used is the Double-Crystal Diffraction (DCD) which was already described in [6.23, 6.24]. The first crystal is often a dislocation-free Ge or Si crystal sometimes cut for using an asymmetric Bragg diffraction for extremely high resolution (see below). The second crystal is a sample to be investigated in the so-called ($+m$, $-n$) [6.25] scattering geometry (which is usually named double-crystal setting) (Fig. 6.3). The dispersion of a double-crystal spectrometer is defined by

$$\frac{\delta\omega}{\delta\lambda} = \frac{\delta\Theta_B^{II} - \delta\Theta_B^{I}}{\delta\lambda} \tag{6.5}$$

In the symmetric case ($+n$, $-n$) the dispersion is zero. This is the mode which is used in the DCD.

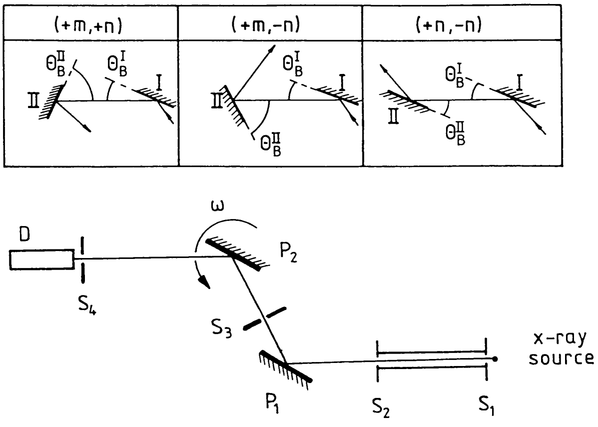

Fig. 6.3. Double-Crystal Spectrometer (DCS). Upper half: schematic presentation of X-Ray optics used in DCS (m, n represent modes corresponding to diffraction orders), with different dispersions; lower half: setup for DCS, $S_1 \dots S_4$ denote slits, P_1 and P_2 monochromator crystal and sample, respectively

The divergent "polychromatic" radiation impinging on the first crystal is reflected according to the corresponding Bragg angles. The second crystal positioned in the equivalent ($-\Theta_B$) Bragg position reflects all wavelengths if it is oriented parallel to the first one (Fig. 6.3). Thus in the ($+n$, $-n$) geometry the X-Ray diffraction is nondispersive, i.e. X-Rays with different wavelengths are diffracted at the same ω setting if both the first crystal and the sample have the same lattice constant.

In the other configuration, the setup is dispersive, i.e. in the ($+m$, $+n$) position a reflection profile results which depends on the divergence of the primary radiation. It is evident that the proper choice of an asymmetric first reflection diminishes the *FWHM* of the reflection profile. Keeping the sample fixed, a beam with small divergence results which is used in triple-crystal and five-crystal (Bartels monochromator) arrangements.

The analysis of the diffraction condition of the double-crystal apparatus and others was performed by Bubakova [6.26] using DuMond's diagrams [6.25], which are in principle graphic presentations of Braggs law $\lambda(\Theta)$ taking into account the spectral broadening of the Bragg reflections. Successive reflections are easily represented. An in depth discussion can be found in DuMond's paper [6.25], including the operation principles of a four-crystal monochromator.

In DCD usually the ($+m$, $-n$) configuration is chosen since for heteroepitaxy the line width of the epilayers is much larger than those from the substrates so that extremely high resolution is unnecessary.

The ($+m$, $-n$) configuration, however, works only dispersionless if the primary monochromator and the sample to be investigated have the same lattice constant, which is a severe limitation of the applicability of this method. It should be mentioned that in order to achieve minimum *FWHM* line, a careful adjustment of the DCD is required [6.26–6.31].

Commercial instruments offer a stepping accuracy on the Θ-axis of one arcsec. This can be achieved by a tangent arm with a micrometer drive, which offers high accuracy over a limited angular range. The angular dispersion of the incident X-Ray beam is typically less than 10 arcsec due to the diffraction from the highly perfect primary crystal.

6.1.3 The 4+1 Crystal Diffractometer

DuMond [6.25] has proposed a four-crystal monochromator which has later been used by Beaumont and Hart [6.32] for wavelength selection of synchrotron radiation. Bartels [6.33] first realised a compact 4-crystal monochromator for high resolution X-Ray diffraction work. It uses 4 Ge crystals between the source and the sample which are cut and oriented in such a way that either (220) or (440) reflected intensities are transmitted (Fig. 6.4).

In the five-crystal diffractometer equipped with a Bartels monochromator, the first two crystals are in the $(+n, -n)$ setting and thus the whole spectral distribution passes as in the DCD. However, the third crystal is in a $(+n, +n)$ position with respect to the second one and thus only a small wavelength range can pass. The fourth crystal positioned with respect to the third one in a $(+n, -n)$ mode reflects the X-Rays in a direction which is parallel to the X-Rays emitted from the source. The successive diffractions produce an extremely monochromatic X-Ray beam ($\approx$ 5% of the intrinsic width of the $\mathrm{CuK}_{\alpha 1}$ line). The wavelength spread $\Delta\lambda/\lambda$ is $2.3 \cdot 10^{-5}$. In the Ge (440) setting the horizontal divergence is 5 arcsec whereas in the (220) setting which yields a factor of 30 higher intensity the intrinsic rocking-curve width is 12 arcsec.

The main advantage is the tunable parallel beam arrangement for a 2Θ scan ranging up to 160° with no loss in resolution in the (440) setting. Arbitrary sample materials can be investigated, independent of the monochromator ma-

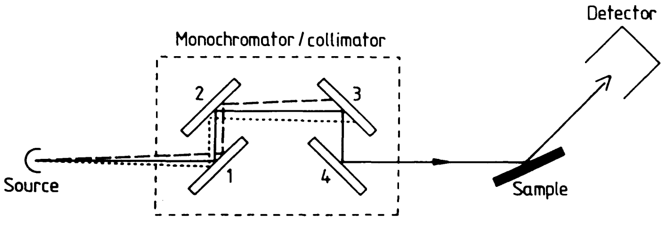

Fig. 6.4. 4 + 1 crystal diffractometer [6.33]. The four Ge crystals use either (220) ($\Delta\theta$ = 12") or (440) reflections ($\Delta\theta$ = 5"). Dash-dotted line: $\lambda_0 \pm \Delta\lambda$

terial. One problem is the vertical divergence (perpendicular to the diffraction plane, i.e. the plane defined by incident and diffracted beams) since it reduces the resolution of the instrument and induces an experimental error. Thus a slit arrangement at the exit of the four-crystal spectrometer is necessary (Soller-slit). It is important to note that the X-Ray beam leaving the four-crystal monochromator in the (440)-setting is nearly completely σ-polarised. Rocking-curves of almost any lattice planes in any direction can be measured. With a suitable goniometer absolute lattice constant determinations are also possible by applying Bond's method [6.34]. Using a similar four-crystal monochromator equipped with 15° asymmetric cut Ge-crystals van der Sluis was able to enhance the intensity by a factor of 3.8 as compared to the original design [6.35].

An alternative beam conditioner is the so-called Channel-Cut Collimator (CCC) which utilizes multiple reflections from parallel crystal planes which are fabricated by cutting a channel into a single crystal. The multiple reflected X-Ray beam leaving the CCC is conditioned with respect to its wavelength and angular dispersion before it is finally monochromated [6.36]. For measurements of extremely narrow reflections the beam divergence may be too large and arrangements with asymmetric reflections should be used [6.37,6.38].

6.1.4 Triple-Axis Spectrometer

Renninger [6.39,6.40] suggested the use of a triple-axis spectrometer in order to measure the asymmetric form of the dynamical reflection profile of a single crystal. With a triple-axis spectrometer several arrangements are possible, which were analysed by Godwod [6.29] and Lefeld-Sosnowska [6.41].

For the investigation of semiconductor heterostructures, a spectrometer setting is used as shown in Fig. 6.5a. Recently, the triple-axis spectrometer system has been further upgraded by using a four-crystal spectrometer as a monochromator in front of the specimen and behind it a two-crystal analyser (Fig. 6.5b). Alternatively to the four-crystal monochromator in another realisation two channel-cut crystals can be adjusted using either eight symmetric (022) reflections from Si or two asymmetrically cut (022) channels with four reflections for high divergence or high internsity purposes (c). A channel-cut crystal is used as an analyser, too. In such an instrument up to thirteen reflections are performed by the X-Ray beam before reaching the detector. In so far this apparatus is also a High-Resolution Multiple-Crystal Multiple-Reflection Diffractometer (HRMCMRD) as described in Sect. 6.1.6.

The advantages of the triple-axis spectrometer are the following:

a) Improved angular resolution (see e.g. figs. 6.34 and 6.35) permits the observation of weak diffraction satellites. This feature also makes the triple-axis spectrometer quite useful for the analysis of extremely thin layers. E.g. using Ge(111) monochromators and analyser crystals Ryan et al. [6.42] have reported a wavevector resolution of $5 \cdot 10^{-4}\text{Å}^{-1}$.

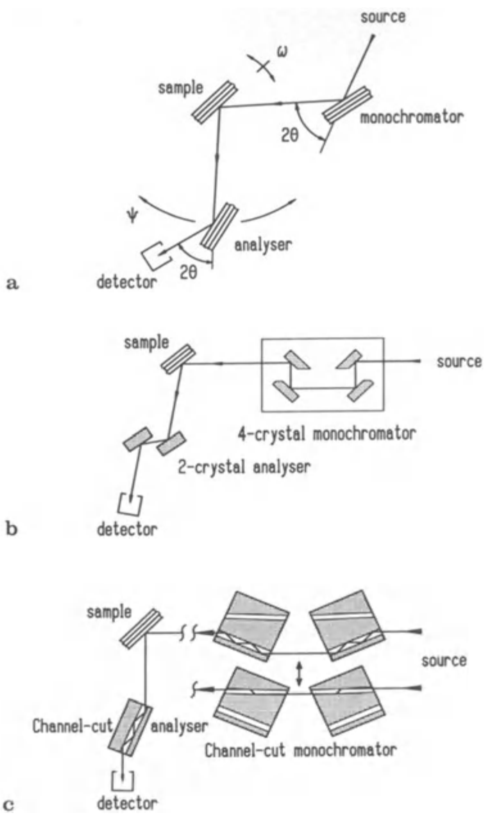

Fig. 6.5a. The triple-axis spectrometer is an extension of the DCS where an analyser crystal is inserted between the sample and the detector, **b** 4 + 1 + 2 spectrometer consisting of a 4-crystal Bartels monochromator for either (220) or (440) setting, the sample and a two-crystal analyser [6.11], **c** triple-axis diffractometer using either 8 symmetric (022) reflections from Si (5" divergence beam $\Delta\lambda/\lambda = 5.5 \cdot 10^{-5}$) or two asymmetrically cut Si (022) channels (4 reflections; 12" divergence) [6.36]

b) Mapping of the reciprocal lattice space: in order to measure intensity contour maps, keeping one of the Miller indices, e.g. l in the reciprocal lattice fixed, and varying h by $\pm\Delta h$, k by $\pm\Delta k$, the instrument just described is used in the following way: the third crystal (2Θ) is scanned for a sequence of different angular positions ω of the sample. A two-dimensional intensity map is thus obtained by measuring a number of $\omega - 2\Theta$ scans along the vector $\mathbf{q}_{\|}[hkl]$ for a (hkl) reflection for different ω offsets (ω-scan direction: perpendicular to $\mathbf{q}_{\|}[hkl]$) (Fig. 6.6). In Fig. 6.6 the reciprocal space maps thus obtained are shown. The conversion of a peak intensity position (ω,

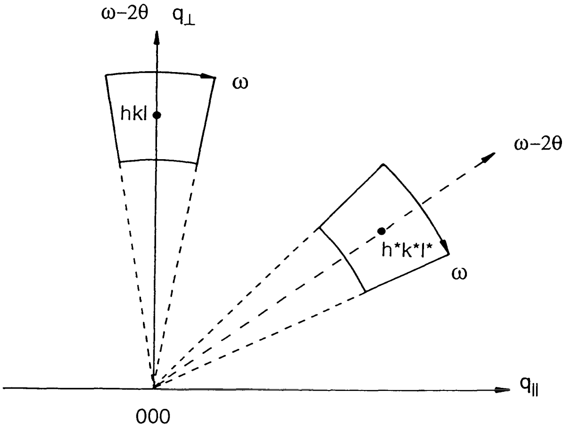

Fig. 6.6. Scans in reciprocal space for two different reciprocal lattice points *hkl* and *h*k*l**

2Θ) in reciprocal space coordinates is given by [6.43, 6.44]:

$$q_{\perp} = \frac{2}{\lambda} \sin\Theta \cos(\omega - \Theta) \tag{6.6}$$

$$q_{\|} = \frac{2}{\lambda} \sin\Theta \sin(\omega - \Theta) \tag{6.7}$$

For the investigation of epilayers, the substrate reflections are used as an internal standard because the absolute values of the angular scale of the diffractometer are unknown. The vector components $q_{\perp}$ and $q_{\|}$ refer to directions perpendicular and parallel to the growth plane. The region which is accessible in reciprocal space mappingdepends on the geometry (reflection or transmission), on the wavelength used as well as on the lattice constants of the epitaxial layer and the substrate. In Fig. 6.7 the region indicated by "C" is accessible for Bragg reflection measurements which is the most common case for the investigation of epitaxial layers. For this example, for the layer the lattice constant of GaAs and the $\mathrm{CuK}_{\alpha 1}$ wavelength was used.

c) The instrument can be used to measure X-Ray reflectivity from the surfaces of semiconductors and amorphous materials and thus one can get information on surface roughness and film thickness.

d) The triple-axis diffractometer allows Bragg plane tilts and dilatations to be determined independently. Thus effects of wafer curvature and mosaicity can be separated [6.6]. A triple-axis spectrometer is most useful for the study of less perfect epitaxial layers and superlattices since, in this mode,

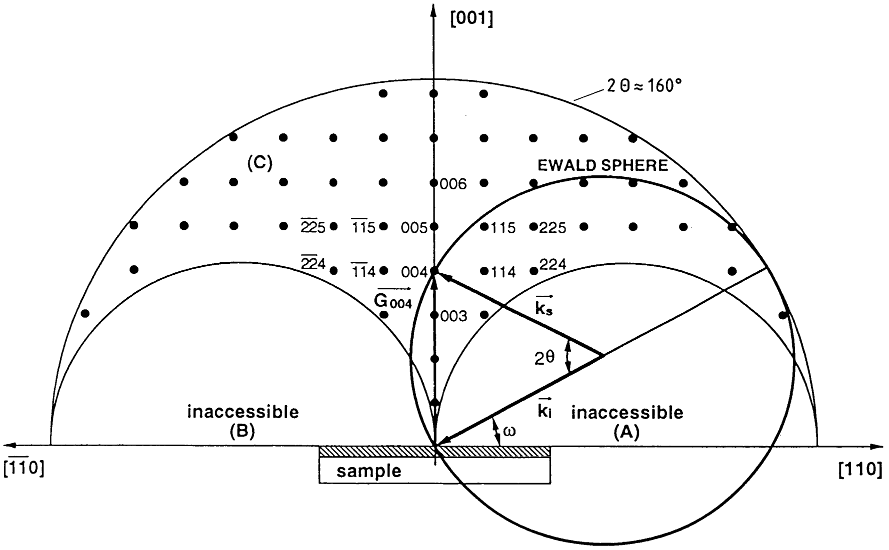

Fig. 6.7. Reciprocal space map showing accessible range for Bragg reflection measurements. The radius of the outer semicircle is limited by the maximum diffractometer angle ($2\theta \approx 160°$). The two inner regions defined by the two semicircles are not accessible in the Bragg case

not only scans as they are performed with double-crystal spectrometers but also reciprocal lattice grids are measured. A combination consisting of the 4+1+2 or channel-cut arrangement (Fig. 6.5c) offers the advantage of a reduction of the background (due to fluorescence) and a signal-to-noise ratio of $10^5 \dots 10^6$ is obtainable [6.45].

e) Diffuse scattering e.g. originating from distorted interfaces can easily be separated from coherent Bragg scattering.

The disadvantage is the following: In comparison to a double-crystal spectrometer, the analyser crystals reduce the intensity and thus longer measurement times result unless the irradiance is increased by using a rotating anode source which provides an higher intensity. The adjustment procedure is quite difficult [6.29] and detailed information on the spectrometer theory is necessary. These difficulties can be avoided by the use of a double-crystal spectrometer equipped with a Position-Sensitive Detector (PSD) [6.46–6.48], placed on the 2Θ arm of that spectrometer (see Fig. 6.49).

Despite the fact that the sample is rotated in the conventional ω-direction, the PSD collects the scattered X-Rays simultaneously over a 2Θ range of 10°. However, it does not integrate over that range but resolves the scattered intensities with a resolution of 70 arcsec.

The main advantage is the fact that during a normal ω-scan using the PSD, information on the scattered intensity in 2Θ-direction is also obtained without any increase in measurement time. A disadvantage results from the reduced dynamic range of the PSD, which is smaller than that of a conventional X-Ray counting system by about two orders of magnitude. Another disadvantage is the relatively poor angular resolution, which causes artifacts in the reciprocal space maps.

Thompson et al. [6.48] have shown that a DCD equipped with a PSD directly yields a separation of mosaic structure from strain effects in rather imperfect layer systems (zone-melt recrystallised silicon sandwiched between SiO_2 layers on Si). The data can be collected within the same amount of time necessary for an ordinary rocking-curve analysis. Thus the combination of a DCD with a PSD offers an alternative to the reciprocal space mapping performed as outlined above.

Picraux et al. [6.12, 6.49] have recently demonstrated that such an instrument is particularly useful for the investigation of strained layers SL's. Although the resolution is much poorer, especially for the 2Θ-scan ($\varDelta 2\Theta =$ 70 arcsec), and thus poorer than the resolution in $\varDelta\omega$ which is a few arcsec, intensity mapping of the reciprocal space is possible. This is done by transforming $\varDelta\Theta$ and $\varDelta\omega$ into $\mathbf{G}_{\parallel}$ and $\mathbf{G}_{\perp}$ using

$$|\mathbf{G}| = \left(G_{\perp}^2 + G_{\parallel}^2\right)^{\frac{1}{2}} = \frac{4\pi \sin(\Theta_B + \varDelta\Theta)}{\lambda} \tag{6.8}$$

$$\frac{G_{\parallel}}{G_{\perp}} = \tan(\varphi - \varDelta\Theta + \varDelta\omega) \tag{6.9}$$

The advantage is a quicker determination of intensity contours at the expense of resolution.

Intensity contour maps provide interesting information on the states of strain of the epitaxial films, i.e. on asymmetries in the distribution of strains and on mosaicity. In real space the resolution is mainly determined by the dimensions of the source aperture. By using a DCD in combination with a microfocus X-ray tube and a narrow detector slit Itoh et al. [6.50] were able to analyze the mosaicity of GaN/(0001)-sapphire and GaAs/ZnSe films.

6.1.5 Renninger Scans

In a Renninger scan a crystal is rotated about the normal to a set of diffracting planes while diffraction from those planes is measured [6.51]. The principle of the technique is illustrated in Fig. 6.8. In such scans an intensity modulation due to multiple-beam interaction is observed which has been evaluated e.g. for accurate measurements of lattice constants and structure factors [6.52, 6.53]. Recently this technique has been applied to characterise epitaxial ZnSe/GaAs structures [6.54]. Morelhao et al. [6.55, 6.56] used a hybrid multiple diffraction in a Renninger scan to study the mosaic spread of a GaAs layer grown on

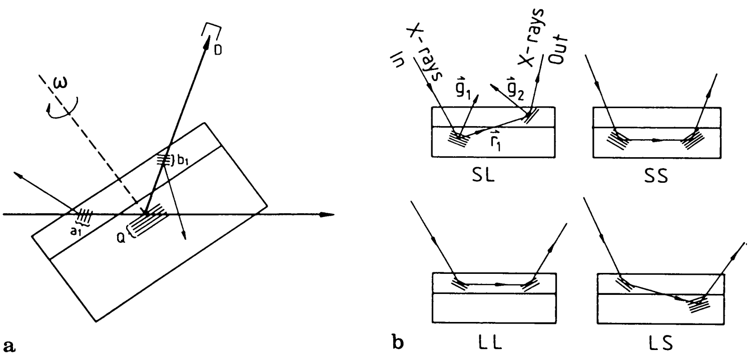

Fig. 6.8a. Renninger scan geometry for detection of modulation of diffracted intensity from substrate lattice planes (Q) due to diffraction within the epilayer a_l and b_l [6.54], **b** Geometry for hybrid multiple diffraction in Renninger scans of layer (L) on substrate (S) epitaxial systems [6.55]

a Si substrate. Hybrid diffractions occur when the beam first diffracted by a substrate or layer plane is rescattered by another substrate or layer plane towards the detector. These type of measurements are evaluated with the aid of Kossel diagrams (see e.g. [6.57]).

6.1.6 High-Resolution Multiple-Crystal Multiple-Reflection Diffractometer (HRMCMRD)

One of the latest developments in HRXRD instrumentation is the HRMCMRD spectrometer (Fig. 6.5c), which is in principle a $4+1+3$ instrument using a total of 8 reflections [6.58, 6.9, 6.10].

The principal setup is shown in Fig. 6.9. It combines the possibilities of the four-crystal monochromators and a multiple-reflection analyser crystal to perform reciprocal lattice scans as well as X-Ray topographs in the same region of the sample.

Fewster has demonstrated that this diffractometer is particularly useful for distinguishing between the residual strain and the mosaic spread in imperfect crystals and avoids misinterpretation of rocking-curves obtained with DCD. As already discussed, the analyser crystal selects the angular range of the diffracted beam reaching the detector. For the analyser a symmetric (220) reflection from a perfect Ge crystal was used and the reduction of the tail intensities in the analyser reflectivity profiles for a twofold and threefold reflection were compared [6.25, 6.59, 6.58]. The benefits of this instrument are the large dynamic intensity range (1 count/s to $10^5 \ldots 10^6$ counts/s) and the size of the diffraction space probe (10") which is very useful for diffraction mapping in the reciprocal space. Further it avoids the so-called star pattern

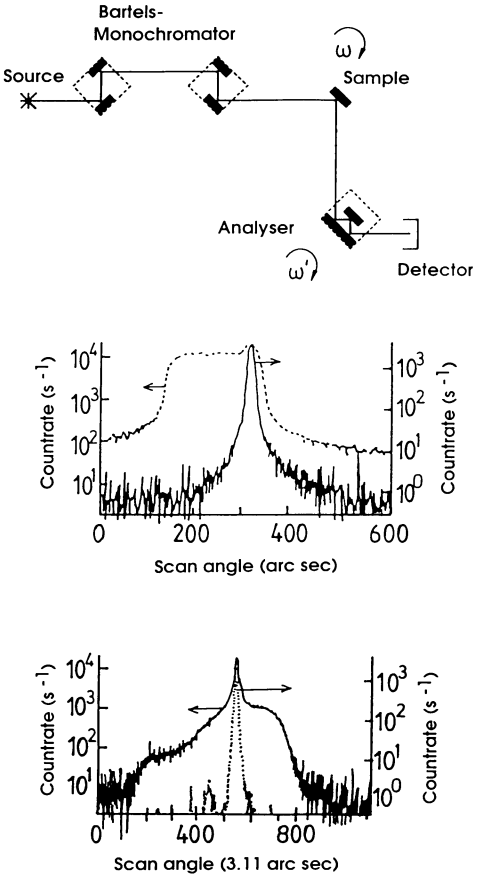

Fig. 6.9. Upper panel: High-Resolution Multiple-Crystal Multiple-Reflection Diffractometer (HRMCMRD) [6.59, 6.58]. Central panel: comparison of a (004) diffraction profile for a mosaic GaAs crystal as obtained with the 4 + 1 diffractometer (dashed line) and the HRMCMRD (solid line). Lower panel: similar comparison for a (004) diffraction from a ZnSe-layer on GaAs (4 + 1) diffractometer (solid line) and from an $\omega - 2\Theta$ scan obtained with the HRMCMRD (dotted line)

around the reciprocal lattice points found in three-crystal three-reflection spectrometers caused by the transfer function [6.60].

In Fig. 6.9 the (4 + 1) and HRMCMRD results are compared for two different material systems: a GaAs substrate, exhibiting mosaicity and a ZnSe epilayer on a GaAs substrate. Clearly, the application of the HRMCRD leads to a tremendous reduction of the linewidth, but, due to third analyzer, reflected intensity is lost in comparison to the (4 + 1) instrument, and thus the measuring time is increased.

6.2 Kinematical and Dynamical Theory

For the investigation of epitaxial layers deposited on comparatively thick substrates, the X-Ray diffraction is monitored in reflection geometry which is called "Bragg-case". The "Laue-case" denotes the measurement of diffracted intensities in transmission which will be not further considered here.

There are two theories describing the scattering of X-Rays (and electrons, neutrons) in crystals: the simpler kinematical and the dynamical theory. For thick perfect crystals one needs the latter one developed by Darwin [6.61], Ewald [6.62] and von Laue [6.63]. In this Darwin-Ewald-Laue theory for a perfect crystal, an exact solution of the wave equation within the crystal is attempted by expressing the wave field by Bloch functions with coefficients which are invariant with respect to the space coordinates. The wave field excited in the crystal can be expressed by a sum of two or more of these wave fields with slightly different values of $\mathbf{k}_i$. As a result the incident and diffracted waves show an amplitude and phase modulation (Pendellösung) effect, first observed in the Laue-case by Kato and Lang [6.64] and in the Bragg-case by Batterman and Hildebrandt [6.65]. The theory was modified by Prins [6.66] for the case of absorption. A general description of the dynamical theory can be found e.g. in the books of Zachariasen [6.67] and Pinsker [6.57]. With recent advances in epitaxial crystal growth technology nearly perfect single crystalline films have become abundantly available and, therefore, the necessity for applying dynamical theory for such systems arose taking into account the finite thickness and interfacial boundaries.

If the interference conditions are fulfilled, a diffracted beam is produced which leads to a weakening of the incoming wave, a process which is called extinction. In this case, at each lattice plane, a part of the incident beam is reflected so that the incident beam arriving at the next plane has a smaller amplitude. Since with increasing depth from the crystal surface this process is repeated many times, the incident beam is finally reduced to negligible amplitude at a depth corresponding to the extinction length (6.22). The extinction length in the case of strong interference depends on the angles of incidence and of emergence of the X-Rays, the X-Ray wavelength, and the structure factor as well as the Debye-Waller factor (Sect. 6.3). The extinction length is typically a factor of ten smaller than the penetration depth due to normal absorption caused by the photoelectric effect. It is of the order of $1 \dots 10\,\mu$m for the materials of interest [6.33].

Therefore only a layer with a thickness smaller than the extinction length contributes to the diffracted intensity in the Bragg-case. The finite width of this layer is the origin of the width of a Bragg diffraction peak along the $\omega - 2\Theta$ scan direction (Darwin width) in dynamical theory.

In the kinematical theory, the crystal potential is treated as a small perturbation (first Born approximation) which is adequate in cases when the extinction length is large compared to the total thickness. It is also adequate for nonperfect (mosaic) crystals. In the kinematical theory the incident wave with wavevector **k** remains unattenuated whereas the reflected wave with wavevector $\mathbf{k}+\mathbf{G}$ ($\mathbf{G}$ denotes a reciprocal lattice vector) is assumed to be weak, but increases in intensity with increasing thickness (i.e. proportional to the square of the thickness). Its application is thus limited to cases for which the thickness is smaller than the extinction length. Moreover, for all calculations inside the crystals, the vacuum wavelength is used. This assumption does not hold e.g. for precision measurements of lattice constants, where the deviations of the refractive index from 1 (in the order of 10^{-6} to 10^{-5}) have to be taken into account. The possibility of multiple scattering, which becomes important in highly perfect crystals of large coherency distances, is neglected.

An alternative description applicable to crystals with small distortions was first given by Takagi [6.68, 6.69] and later by Taupin [6.70]. The Takagi-Taupin formalism is the one which is used nowadays almost exclusively for the calculation of dynamic scattering effects in high resolution X-Ray diffraction. The wave excited in the crystal is expressed by a single sum, but the coefficients are considered as a slowly varying function of depth position instead of being constant as would be in the case of kinematical theory. In the two-beam approximation the change of the amplitude of the incident wave D_i and scattered wave D_s with the depth z into the crystal are given by the Takagi-Taupin equations:

$$\frac{\mathrm{i}\,\lambda\gamma_s}{\pi}\frac{\partial D_s}{\partial z} = \Psi_i D_s + C\Psi_s D_i - \alpha_s D_s \tag{6.10}$$

$$\frac{\mathrm{i}\,\lambda\gamma_i}{\pi}\frac{\partial D_i}{\partial z} = \Psi_i D_i + C\Psi_{\bar{s}} D_s \tag{6.11}$$

with the notations $\alpha_s(\omega) = -2\lambda(\Theta - \Theta_B)/(d_{hkl})$ and $\Psi_{i,s} = -\lambda r_e F_s/\pi V$, r_e being the electron radius, $F_{i,s}$ are the complex structure factors, and V is the volume of the unit cell. γ_i and γ_s are the direction cosines of the incident and scattered beams with respect to the internal surface normal. i, s denote a certain reflection (hkl) and consequently $F_{\bar{s}}$ is the structure factor for $(\bar{h}\,\bar{k}\,\bar{l})$. C denotes the polarisation factor ($C = 1$ for σ-polarisation and $C = |\cos 2\Theta_B|$ for π-polarisation). Combining these two equations for the Bragg-case a differential equation for the amplitude ratio D_s/D_i results:

$$-\mathrm{i}\frac{dX}{dT} = X^2 - 2\eta X + 1 \tag{6.12}$$

where X, η, T are complex quantities given by

$$X = \sqrt{\frac{F_{\bar{s}}}{F_s}}\sqrt{\left|\frac{\gamma_s}{\gamma_i}\right|}\frac{D_s}{D_i} \tag{6.13}$$

$$
\begin{aligned}
\eta &= \frac{-b(\Theta-\Theta_B)\sin 2\Theta_B - \frac{1}{2}\Gamma F_0(1-b)}{\sqrt{|b|C\Gamma\sqrt{F_sF_{\bar{s}}}}} && (6.14)\\
T &= \frac{\pi C\Gamma\sqrt{F_sF_{\bar{s}}}\,d}{\lambda\sqrt{|\gamma_i\gamma_s|}} && (6.15)
\end{aligned}
$$

where $\Gamma = r_e\lambda^2/\pi V$, $b = \gamma_i/\gamma_s$. d is the crystal thickness, and F_0 the structure factor for (000). The departure from the Bragg angle Θ_B determines the deviation parameter η. The solution of the differential equation is given by

$$
X_d = \eta + \sqrt{\eta^2-1}\,\frac{S_1+S_2}{S_1-S_2} \qquad (6.16)
$$

where

$$
S_{1,2} = \left(X_0 - \eta \pm \sqrt{\eta^2-1}\right)\,\exp\left(\mp \mathrm{i}\,T\sqrt{\eta^2-1}\right) \qquad (6.17)
$$

For layered structures the recursion X_d usually starts with the infinite thick substrate ($d \longrightarrow \infty$) [6.71]:

$$
X_\infty = \eta - \operatorname{sign}(\operatorname{Re}(\eta))\sqrt{\eta^2-1} \qquad (6.18)
$$

The reflectivity R_s is finally given by

$$
R_s = \left|\frac{\gamma_s}{\gamma_i}\right|\cdot\left|\frac{D_s}{D_i}\right|^2 = \left|\frac{F_s}{F_{\bar{s}}}\right|\,|X|^2 \qquad (6.19)
$$

The rocking-curve of the sample is determined by the reflectivity R_s as a function of the deviation parameter η.

Recently, on highly strained superlattices small discrepancies between the experimental and theoretical angular positions of higher-order satellite peaks have been observed using the conventional deviation parameter (6.14) in the Takagi-Taupin equations [6.72,6.74,6.73]. One reason was assumed to be the linear approximation

$$
\sin\Theta - \sin\Theta_B \approx (\Theta-\Theta_B)\cos\Theta_B \qquad (6.20)
$$

for the conventional deviation parameter. Indeed, for symmetric reflections a higher-order approximation gives the correct Bragg positions for the superlattice peaks [6.73,6.74]. For asymmetric reflections, however, only a new deviation parameter based on the solution of the dynamical equations for the amplitudes of the electric field in the crystal gives the correct result. Unlike the conventional solution, the new deviation parameter takes into account the scattering geometry before reducing the dispersion relation of 4th degree to second degree in the wavevector [6.75]. Thus a deviatiation parameter results which describes all scattering geometries correctly.

In order to illustrate the influence of the different orientations on the shape of the reflectivity as a function of ω in Fig. 6.10, we compare the reflectivity curve for a (333) Bragg diffraction with that of a (115) crystal diffraction. Since for both Bragg diffractions $h^2 + k^2 + l^2 = 27$ the only difference are their anisotropy factors b (6.2).

Especially, in the case of thin films Pendellösung fringes are caused by the interference of the wave fields. These fringes will be further modulated if two or more layers with different lattice parameters scatter the X-Rays. Then the wave fields originating from the single layers interfere as well and affect the Pendellösung fringes. Consequently, the interference phenomena in multilayers are extremely useful for the investigation of structural properties even of ultrathin layers (buried layers of monolayer thickness and heterointerfaces).

Recently, Chen and Bhattacharya [6.76] have shown that the Darwin-Prins formulation [6.77] of the dynamical X-Ray scattering is equivalent to the

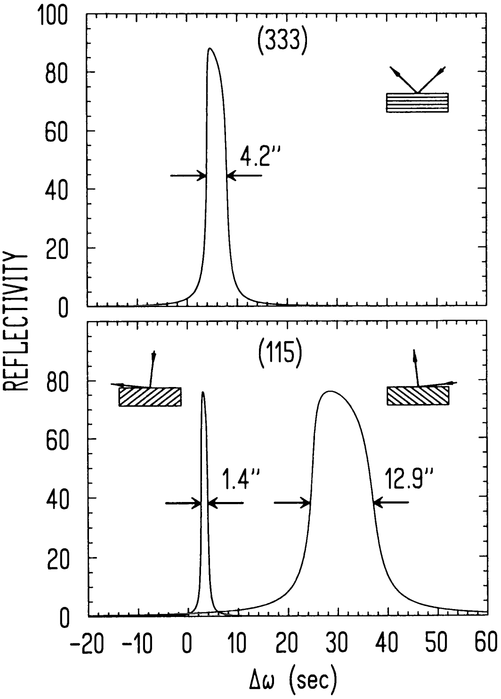

Fig. 6.10. Calculated reflectivity curves for σ-polarised Cu$K_{\alpha 1}$ radiation of (111) oriented Ge for symmetric (333) and asymmetric (115) and ($\bar{1}\bar{1}5$) glancing incidence and glancing exit reflections (see Fig. 6.17). The latter ones demonstrate the influence of the asymmetry factor on the *FWHM*. σ-polarised radiation is the relevant one in most experiments. For π-polarised radiation the peak shape appears nearly symmetric around a central maximum [6.86]

Takagi-Taupin approach under the assumption that the crystal is a continuous medium. The computer programs nowadays available for fitting diffraction data of epitaxial films and an arbitrary number of epitaxial layers (even with different lattice parameters as a function of depth) are based on the Takagi-Taupin formalism. Sometimes further simplifying assumptions are made in so called "semi-kinematical theories". The original formulation is due to Petrashen [6.78, 6.79] for distorted crystals. Tapfer and Ploog [6.80, 6.81] have further developed this method for obtaining precise information on chemical composition, thickness, strain profile, and interface quality of heterostructures and multilayers. A first iteration of Taupin's equations for the amplitude ratio of the incident and diffracted waves $\mathbf{k}_i$ and $\mathbf{k}_s$ is used. This approach is valid if the thickness of the deformed layers is small compared with the extinction length. The main advantage of this procedure is the reduction of computation time for the simulation of diffraction curves. In the spirit of this "semi-kinematical" approach, the thin epitaxial film is treated kinematically whereas for the thick substrate a dynamical calculation is performed. Originally, for epitaxial layers, superlattices [6.82–6.84] and ion-implanted semiconductors [6.85] the kinematical model was quite successfully applied in analysing the measured rocking-curves. In [6.3], the kinematical method is described in detail and the limits of its applicability are discussed. Bartels et al. [6.71] have used the criterion that the observed peak reflectivities must be less than about 10% to 6% in order that the kinematical theory can be applied. Therefore, close to the $i = 0$ central peak of a superlattice or close to the substrate peak, an intensity analysis based on the kinematical approach may yield improper results. In recent years it was observed that there are small but important discrepancies in the Bragg peak position of a thin epilayer or the zeroth order superlattice peak in the results from the kinematical and the dynamical models [6.8,6.87–6.89].

These discrepancies are very important for practical applications since from the angular distance of the Bragg peaks of the epilayer and that of the substrate lattice strain and changes in chemical composition are deduced. It was shown that in most cases a combination of kinematical theory for the layers and dynamical theory for the substrate can be used for the simulation of rocking-curves of the thin layer samples. However, an important point is the matching condition for the phases at the layer to substrate boundary. According to Wie and Kim [6.90] matching conditions for the amplitudes (dynamical amplitude for the substrate, kinematical amplitude for the epitaxial layer $\hat{=}$ Amplitude Boundary Conditions (ABC)) have to be used instead of the previously taken Intensity Boundary Conditions (IBC). Even with this recent improvement, it can be dangerous to use the previously accepted rule (e.g. [6.71, 6.3]) according to which for epitaxial films with less than 10% X-Ray reflectivity power, the full dynamical and the kinematical calculations yield identical results. Kim and Wie [6.90] have made a comparison of calculated X-Ray scattering results for AlGaAs/GaAs, GaInAs/InP heterostructures and a superlattice sample AlGaAs/GaAs using the semikinematical and a full dynamical calculation. Both the Bragg peak profile and the peak positions agree for both types of models using the amplitude boundary condition, if e.g. a layer sequence CAC of AlGaAs (C)/GaInAs (A)/AlGaAs (C) is deposited on a GaAs substrate. However, in the case where one of the layers is identical in chemical composition to the substrate (e.g. GaAs (B)/GaAlAs (A)/ GaAs substrate (B)), a semi-kinematical model is no longer adequate because the substrate peak (B) is calculated dynamically and a layer peak (also B, of the same chemical composition) is treated kinematically. Thus, in general, nowadays the dynamical theory should be applied.

Already in 1986, Macrander et al. [6.91] came to that conclusion and performed simulations of graded layers, which have no discontinuity in lattice constant at the interfaces. For such structures dynamical simulations are also required. The authors employed a computational procedure for the simulation of superlattice rocking-curves based on the Abeles' matrix method [6.92]. This method was originally developed for optics in the visible range (see Chapter on FIR spectroscopy).

In another method, used by Tapfer et al. [6.93], a recurrence formalism is used to calculate the diffraction pattern based on the work by Vardanyan et al. [6.94]. This is also a dynamical diffraction theory for (layered) crystals of arbitrary thicknesses which takes into account multiple reflection and the interference of the wave fields from the various layers and from the substrate, including the exact boundary conditions at the heterointerfaces and including lattice strain as well. (Also in the Takagi-Taupin formalism the effects of strain can be taken into account). Tapfer et al. [6.88, 6.93] have recently extended the theory by Varadanyan et al. [6.94] for very small glancing angles where the refraction effect cannot be neglected. In strongly mismatched heterostructure systems, the crystalline quality can be poor and even mosaic structured. In such a case (e.g. CdTe/GaAs, GaAs/Si) diffraction within one mosaic crystal is independent from the adjacent ones and the kinematical approach is well suited. A further approach due to Wie and Kim [6.95, 6.90] starts with the Takagi-Taupin equations, but solves the dynamical recursive formulae in the Bragg-case with the use of a matrix formalism which is particularly convenient for large period superlattices since then the algorithm is faster than the recursive formula approach.

Very recently the Darwin theory of dynamical diffraction was extended by Caticha for the symmetric Bragg case [6.96] to include the regions between Bragg peaks as well as situations of grazing and normal angles of incidence. In the modified theory the diffracting crystal is built up of N plates, the surface of which are normal to the z direction. The layers of thickness d are separated by infinitesimal gaps. The electric field in each gap is treated as a superposition of an incident and reflected plane wave, thus an involved many-beam dynamical diffraction calculation reduces to a two-beam calculation. It is shown that the theory reproduces the two-beam Laue dynamical theory in the vicinity of the Bragg peaks and the reflectivities between the Bragg peaks in agreement with the kinematical theory, which was exclusively used in this angular range so far.

6.3 Thickness Dependence of Bragg Reflections from Thin Films

Both intensity and Full Width of Half Maximum (*FWHM*) of Bragg reflections strongly depend on the thickness of the measured crystal. This dependence is caused by different effects: due to the photoeffect the penetrating X-Ray intensity is always weakened, independently of Bragg condition. This process is described by an exponential law. The absorption depth d_{abs} is defined as the thickness of a layer that reduces the intensity by a factor of e:

$$d_{\text{abs}} = \left(\mu\left(\frac{1}{|\gamma_i|} + \frac{1}{|\gamma_s|}\right)\right)^{-1} \tag{6.21}$$

where μ is the linear absorption coefficient and $\gamma_{i,s}$ are the direction cosines as defined in (6.2). The absorption depth is of the order $< 100\,\mu$m.

As already discussed in the previous Chapter, in case interference conditions are fulfilled, the intensity is additionally weakened due to the production of diffracted beams. This process is called *primary* extinction and is described by the extinction length d_{ext}

$$d_{\text{ext}} = \frac{V\sqrt{|\gamma_i \cdot \gamma_s|}}{r_e \lambda |F_s'|} \tag{6.22}$$

where F_s' contains only contributions of the real part of the structure factors. The extinction depth is of the order of $< 10\,\mu$m. Apart from the primary extinction there is *secondary* one, which is important in X-ray diffraction from polycrystalline materials or powders [6.97]. It results from the fact that a certain grain within the sample is illuminated by a smaller intensity, if a grain which differs in orientation is situated above oriented, scatters in Bragg condition. The reflectivity of InP epitaxial layers is shown in Fig. 6.11 as a function of layer thickness taking only extinction into account.

Thus, even without absorption, X-Rays penetrate only several thousand atomic layers into a single-crystalline film. This leads to the finite broadening of the reflected X-Ray intensity since just a finite number of scattering centres contributes:

$$FWHM = \frac{2.12 \cdot \lambda \cdot \gamma_s}{\pi d_{\text{ext}} \sin 2\theta_B} \tag{6.23}$$

In Fig. 6.12 the reflectivity of thin InP crystals including absorption is shown.

The reflected X-Ray intensity is thus determined both by primary extinction as well as by absorption. The *FWHM* of a rocking-curve is generally

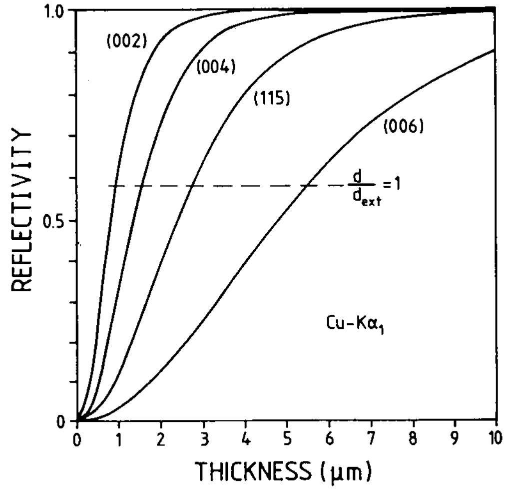

Fig. 6.11. Reflectivity versus layer thickness of an (001) oriented InP epitaxial layer for different Bragg reflections. Absorption assumed to be zero. d_{ext}: extinction depth [6.33]

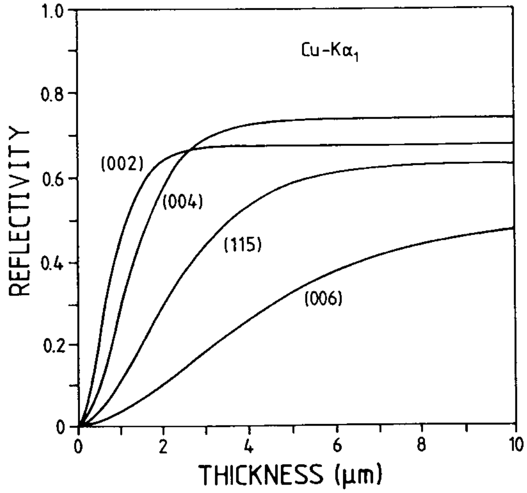

Fig. 6.12. As Fig. 6.11 but taking absorption and extinction into account [6.33]

taken as a measure for the crystal quality. For perfect crystals with thicknesses below the extinction length additional broadening occurs which increases with decreasing thickness.Therefore the proper interpretation of a half-width obtained from a thin film requires knowledge of the film thickness. It's worth mentioning that the *FWHM* of a certain Bragg peak is linked to the structure factor of the material. For a Bragg peak with high structure factor the number of contributing lattice planes is comparatively small and, consequently, the *FWHM* is large.

With an incident angle corresponding to a reflection position (Bragg angle), the extinction essentially determines the penetration depth of X-Rays in the perfect crystal. For practical applications it is quite useful to have the effects just described in mind. In Fig. 6.13 the *FWHM* versus film thickness is plotted for $\mathrm{CuK}_{\alpha 1}$ radiation and a Bragg angle $\theta = 31.6°$ (InP, (004)). Consequently, a comparison of the width of X-Ray intensities, even from the same symmetric Bragg diffraction but from different films without specifying the thicknesses, can only be performed if the thickness dependence of the *FWHM* is taken into account.

In addition, broadening due to the experimental setup occurs. In an experimental setup the measured reflectivity $I(\omega)$ as a function of ω is the autocorrelation of $R(\theta)$:

$$I(\omega) \sim \int_{-\infty}^{\infty} R(\theta)R(\theta-\omega)\,d\theta \tag{6.24}$$

where the $(+n, -n)$ scattering geometry is assumed and the two crystals are exactly parallel. Thus $I(\omega)$ should be a symmetric function around ω_o. In a detector not the ideal intensity distribution $I(\omega)$ is recorded, but the intensity resulting from a convolution of $R(\theta)$ with a function depending on the special experimental setup $C(\theta, \alpha, \Phi, \Delta\lambda)$ where α denotes the horizontal divergence $(-\alpha_m, +\alpha_m$: few degrees) and Φ the vertical divergence $(-\Phi_m, +\Phi_m$ such that $\sin\Phi_m \approx \Phi_m)$ [6.26]. Due to those influences, $I(\omega)$ is in practice broader than $R(\theta)$.

Besides these broadening effects, reflectivity measurements of thin films exhibit Pendellösung fringes originating from the fact that the diffracted intensity oscillates periodically with thickness. The intensity modulation of the

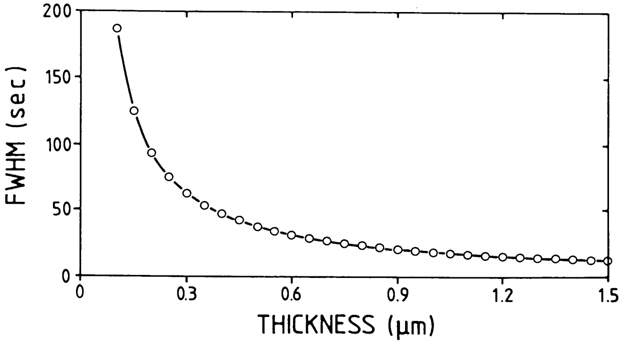

Fig. 6.13. *FWHM* of the (004) reflection of InP versus layer thickness for $\mathrm{CuK}_{\alpha 1}$ radiation [6.98]

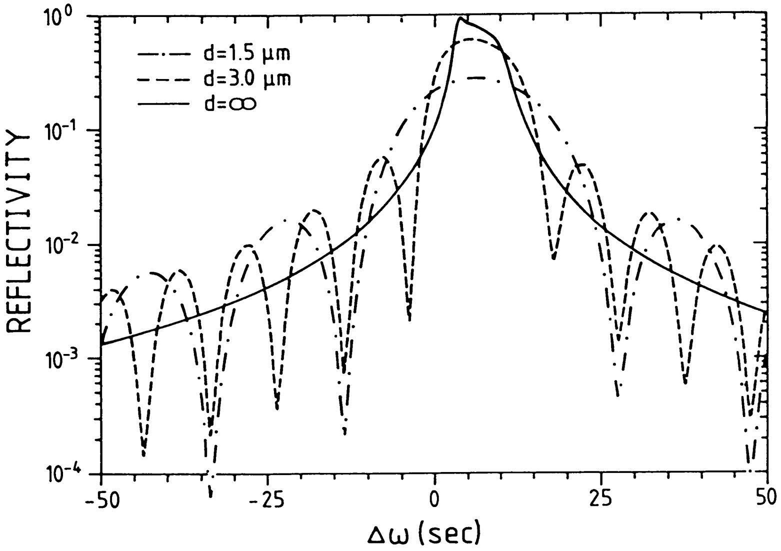

Fig. 6.14. Calculated rocking-curves for InP (004) Bragg reflection for three different thicknesses for CuK$_{\alpha 1}$ radiation [6.86]

reflected waves critically depends on the boundary planes of the crystalline film and its homogeneity. According to Bartels [6.33] for thin films with a thickness D small compared to the extinction thickness d_{ext} (neglecting absorption) the *FWHM* is:

$$FWHM = \frac{\lambda \cdot \gamma_s}{D \cdot \sin 2\theta} \tag{6.25}$$

The oscillation period of the reflected intensity is directly connected with the thickness as shown in Fig. 6.14 for a (004) diffraction of (001) oriented InP crystals.

6.4 Strain Phenomena

Until now only free-standing films have been discussed. In practice epitaxially grown heterostructures have to be analysed. Information about the composition of alloy semiconductor layers, its gradients and its state of strain is required. In the case of large strain values a tilt of the layer planes relatively to the substrate can occur which has to be distinguished from similar effects for layers grown on misoriented substrates.

6.4.1 Strains in Epitaxial Layers

For about 20 years strains in epitaxial layers have been studied by various X-Ray methods. The lattice constant of a thin film which grows coherently on a single-crystalline substrate is modified parallel to the growth direction. Due to strain the crystallographic properties of single crystal films become anisotropic and the measured X-Ray diffraction phenomena have to be analysed in order to deduce the lattice parameters and the reduction of symmetry due to strain (Fig. 6.15). It is assumed that the film is much thinner than the substrate and that therefore the substrate remains unstrained [6.99].

In most cases the growth direction is a [001] direction, sometimes also an [111] or an [110] direction is chosen. By X-Ray measurements information is obtained on the strains which are related to the stresses in a cartesian coordinate system by the following equation (for cubic symmetry) [6.100]

$$\begin{pmatrix} \sigma_{xx} \\ \sigma_{yy} \\ \sigma_{zz} \\ \sigma_{yz} \\ \sigma_{xz} \\ \sigma_{xy} \end{pmatrix} = \begin{pmatrix} C_{11} & C_{12} & C_{12} & \cdot & \cdot & \cdot \\ C_{12} & C_{11} & C_{12} & \cdot & \cdot & \cdot \\ C_{12} & C_{12} & C_{11} & \cdot & \cdot & \cdot \\ \cdot & \cdot & \cdot & C_{44} & \cdot & \cdot \\ \cdot & \cdot & \cdot & \cdot & C_{44} & \cdot \\ \cdot & \cdot & \cdot & \cdot & \cdot & C_{44} \end{pmatrix} \begin{pmatrix} \epsilon_{xx} \\ \epsilon_{yy} \\ \epsilon_{zz} \\ \epsilon_{yz} \\ \epsilon_{xz} \\ \epsilon_{xy} \end{pmatrix} \tag{6.26}$$

where the C_{ij} are the stiffness coefficients. For growth along z-direction with x, y in the plane of the film the stress tensor component σ_{zz} is always zero

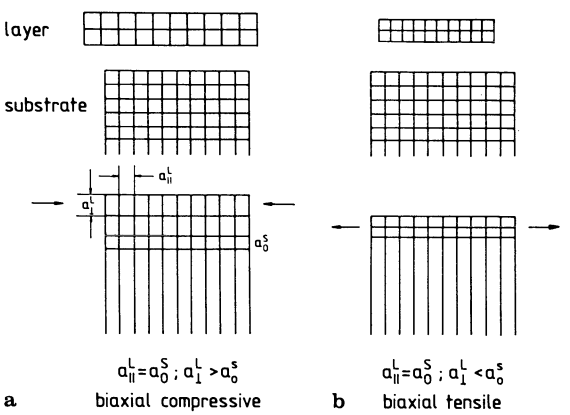

Fig. 6.15. Schematic illustration of the origin of biaxial compressive ($a_L > a_S$) (**a**) and biaxial tensile strain ($a_L < a_S$) (**b**). The in-plane lattice constants remain unchanged and the $a_{\perp}$ lattice constants are either increased (compressive in plane strain) or decreased (tensile in plane strain). Diagram corresponds to a tetragonal distortion

and thus

$$\sigma_{zz} = 0 = C_{12}\epsilon_{xx} + C_{12}\epsilon_{yy} + C_{11}\epsilon_{zz} \tag{6.27}$$

This yields a relation between $\epsilon_{zz}, \epsilon_{xx}$ and ϵ_{yy} provided that the elastic stiffnesses are known. Assuming a tetragonal distortion [6.101] the in-plane lattice spacings along the x [100] and y [010] direction are that of the substrate a_0^S, whereas the lattice spacing along the growth direction is modified (Fig. 6.16). In this case there exists a finite angle $\Delta\varphi$ between the [101] directions of the substrate and film. As can be seen from Fig. 6.16 for tetragonal distortion $\Delta\varphi_1 = \Delta\varphi_2$ results.

The statements given above can be expressed in the following way: If there are no forces in growth direction, then $\sigma_{zz} = 0$. For biaxial tension or compression $\sigma_{xx} = \sigma_{yy}$ and thus

$$\sigma_{zz} = C_{11}\epsilon_{zz} + C_{12}\epsilon_{xx} + C_{12}\epsilon_{yy} = 0 \tag{6.28}$$

$$\sigma_{xx} = C_{11}\epsilon_{xx} + C_{12}\epsilon_{yy} + C_{12}\epsilon_{zz} \tag{6.29}$$

$$\sigma_{yy} = C_{12}\epsilon_{xx} + C_{11}\epsilon_{yy} + C_{12}\epsilon_{zz} \tag{6.30}$$

and thus it follows $\epsilon_{xx} = \epsilon_{yy}$. Therefore in the strained case the lattice constants of the film in x and y direction are:

$$a_x = a_y = a_{\|} \tag{6.31}$$

For tetragonal distortion and pseudomorphic growth the face diagonals in the xy-plane [110] and $[\bar{1}10]$ are of the same length. The components of the strain tensor are given by:

$$\epsilon_{xx} = \epsilon_{yy} = \frac{a_0^S - a_0^L}{a_0^L} \tag{6.32}$$

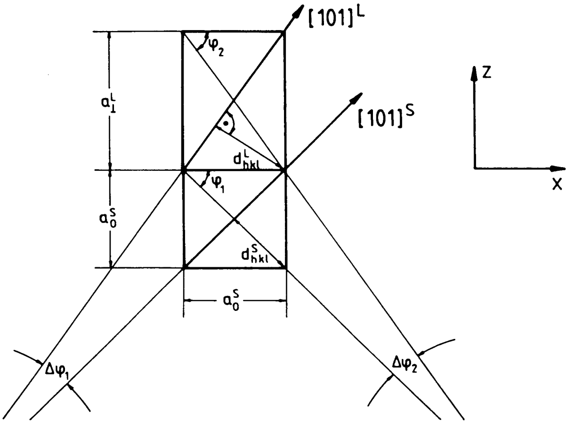

Fig. 6.16. Definition of angles in tetragonal distortion: for layer L on substrate S

and

$$\epsilon_{zz} = \frac{a_z^L - a_0^L}{a_0^L} \tag{6.33}$$

where a_z^L is equivalent to $a_\perp$. It is important to note that in the X-Ray investigation of thin epitaxial films on comparatively thick substrates usually no absolute measurements of the lattice parameters of both the film and the substrate are made but that the measurements are made relative to the substrate.

Therefore, apart from the conventional definition of the components of the strain tensor, following the work of Hornstra and Bartels [6.102] it has become convenient to define an X-Ray strain which compares lattice constants in the strained film with that of the unstrained substrate (parallel means within the surface plane, perpendicular means along the surface normal, i.e. along the growth direction):

$$\epsilon_\parallel^L = \frac{a_\parallel^L - a_0^S}{a_0^S} \tag{6.34}$$

$$\epsilon_\perp^L = \frac{a_\perp^L - a_0^S}{a_0^S} \tag{6.35}$$

Using (6.32) these X-Ray strains ϵ^L of the films are related to the actual strain in the epitaxial layer ϵ_L, which would be measured relative to an unstrained epitaxial film, by the following equation:

$$\epsilon_L = \left(\epsilon^L + 1\right) \frac{a_0^S}{a_0^L} - 1 \tag{6.36}$$

where a_0^L is the lattice constant of the unstrained layer. $\epsilon_L^\perp$ and $\epsilon_L^\parallel$ are related to each other via the elastic constants of the epitaxial layer (for [001] oriented samples):

$$\epsilon_\perp^L = \left(1 + \frac{2C_{12}}{C_{11}}\right) \frac{a_0^L - a_0^S}{a_0^S} - \frac{2C_{12}}{C_{11}} \epsilon_\parallel^L \tag{6.37}$$

(note: the relation for the X-ray strains is different from that for the actual strain ϵ_L)

$$\epsilon_L^\perp = -\frac{2C_{12}}{C_{11}} \epsilon_L^\parallel \tag{6.38}$$

Using symmetric X-Ray diffraction, information on a_z^L is obtained. From (6.37) the unstrained lattice constant of the layer which is important for determining e.g. the composition of alloys is then given by the following relation:

$$a_0^L = \frac{C_{11}}{C_{11} + 2C_{12}} \left(a_z^L - a_0^S\right) + a_0^S \tag{6.39}$$

(Here the contribution resulting from $\epsilon_{\|}^{L}$ is zero). For growth direction along [111] and [110] similar relations are given by Segmüller and Murakami [6.99], Ortner [6.103] and Anastassakis [6.104].

Only in the case of pseudomorphic growth and a simple heterolayer sufficient information can be extracted from the symmetric X-Ray diffraction alone. Usually the growth of heterolayers changes from pseudomorphic to non-pseudomorphic beyond a certain critical thickness, and partial strain relaxation occurs. Therefore $a_{\|}^{L} \neq a_{0}^{S}$. In order to determine the state of strain, in addition to symmetric reflections, asymmetric ones are needed: the definition of angles for such an asymmetric situation is given in Fig. 6.17.

In the rocking-curve the angular difference $\Delta\omega$ between the Bragg diffractions (hkl) of the layer and the substrate is due to two components:

$$\Delta\theta_B = \theta_B^S - \theta_B^L \tag{6.40}$$

and

$$\Delta\varphi = \varphi^S - \varphi^L \tag{6.41}$$

The angular separation between the diffraction peaks is either $\Delta\theta_B + \Delta\varphi$ or $\Delta\theta_B - \Delta\varphi$ in reflection geometry A or B, respectively. Thus:

$$\Delta\omega_A = \Delta\theta_B + \Delta\varphi \tag{6.42}$$

$$\Delta\omega_B = \Delta\theta_B - \Delta\varphi \tag{6.43}$$

According to Bartels [6.33] the difference $\Delta\theta_B$ which corresponds to the differences in lattice spacing and $\Delta\varphi$ which determines the difference in lattice plane orientation is used to calculate $(\Delta a/a)_\perp$ and $(\Delta a/a)_\|$

$$\left(\frac{\Delta a}{a}\right)_\perp = \Delta\varphi \tan\varphi - \Delta\theta_B \cot\theta_B \tag{6.44}$$

$$\left(\frac{\Delta a}{a}\right)_\| = -\Delta\varphi \cot\varphi - \Delta\theta_B \cot\theta_B \tag{6.45}$$

where

$$\Delta\theta_B = \theta^S - \theta^L = \frac{1}{2}(\Delta\omega_A + \Delta\omega_B) \tag{6.46}$$

$$\Delta\varphi = \varphi^S - \varphi^L = \frac{1}{2}(\Delta\omega_A - \Delta\omega_B) \tag{6.47}$$

The Eqs. (6.44, 6.45) are approximations for small $\Delta\theta$ and $\Delta\varphi$. For large strains the errors in $(\Delta a/a)_\perp$ and $(\Delta a/a)_\|$ are of the order of several percent. In order to determine $\Delta\theta_B$ and $\Delta\varphi$ independently of each other, measurements in the geometries A and B have to be performed.

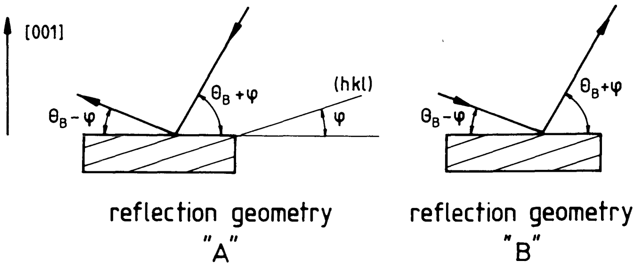

Fig. 6.17. Definition of diffraction geometry for asymmetric Bragg diffraction. φ: angle between plane (hkl) and sample surface, θ_B: Bragg angle. With the help of reflection geometries A ("high incidence") and B ("low incidence") strain, tilt and terracing measurements are performed

In order to confirm whether an epitaxial film on a (001) surface is tetragonally distorted, several asymmetric Bragg reflections have to be measured, e.g. those belonging to a [110] zone. Meyerheim [6.98] used a GaAs/$Ga_{0.4}Al_{0.6}As$ structure and investigated the asymmetric (117), (115), (112), (335) and (444) diffraction and the symmetric (004) diffraction. From the latter the value of $(\Delta a/a)_\perp$ was determined using (6.44).

The differentiated Bragg equation

$$\left(\frac{\Delta d}{d}\right)_{llh} = \frac{\Delta\omega_A + \Delta\omega_B}{2\tan\theta_{llh}} \tag{6.48}$$

yields the value of the distortion normal to the lattice plane (llh). The following relations hold [6.102]:

$$\frac{\Delta\varphi}{(\Delta d/d)_\perp} = \cos\varphi\sin\varphi \tag{6.49}$$

$$\frac{(\Delta d/d)_{llh}}{(\Delta d/d)_\perp} = \cos^2\varphi \tag{6.50}$$

In Fig. 6.18 the measured values of these expressions are plotted vs. φ and compared with the trigonometric functions. The agreement between the measured and calculated values proves the validity of the models for the tetragonal distortion in this case.

There remains a further problem: namely whether or not under certain conditions a more general distortion, e.g. a monoclinic, triclinic or orthorhombic one, can be observed. In the case of anisotropic and inhomogeneous strain relaxation of $In_xGa_{1-x}As$/GaAs structures Grundmann et al. [6.105] and Giannini et al. [6.106] have suggested such a distortion. Such a deformation would lead to non-equivalent angles $\Delta\varphi_1 \neq \Delta\varphi_2$ (Fig. 6.19).

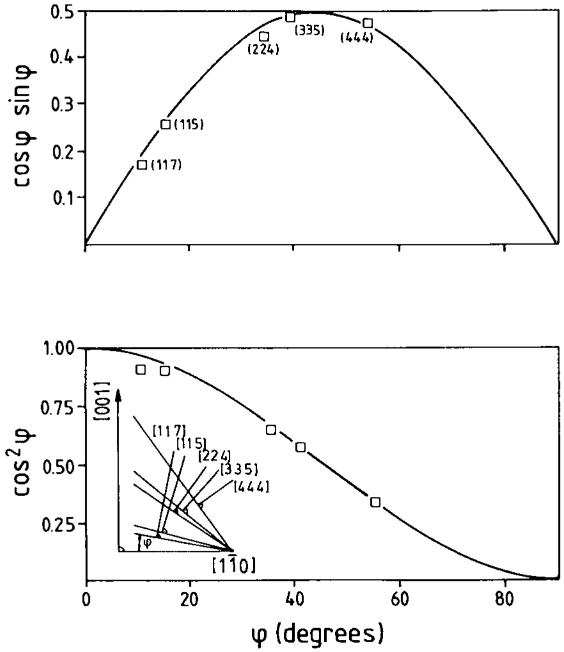

Fig. 6.18. Determination of elastic tetragonal distortion for a GaAs / $Ga_{0.4}Al_{0.6}As$ heterostructure. Measurement quantities are $\Delta\varphi$ and $\Delta d/d_{hkl}$: upper half: $\cos\varphi \sin\varphi (= \Delta\varphi/(\Delta d/d))$ versus φ. lower half: $\cos^2\varphi (= ((\Delta d/d)_{hkl})/(\Delta d/d))$ versus φ for 5 Bragg diffractions where $\Delta d/d$ denotes the misfit to the direction of the surface normal [6.98]

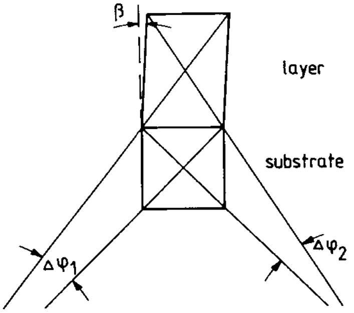

Fig. 6.19. Illustration of monoclinic distortion of cubic layer with respect to the substrate. In contrast to tetragonal distortion in Fig. 6.15 angles $\Delta\varphi_1 \neq \Delta\varphi_2$

For the $Al_{0.6}Ga_{0.4}As$/GaAs structures the equivalence $\Delta\varphi_1 = \Delta\varphi_2$ of which was checked by measurement of the (115) and ($\bar{1}\bar{1}5$) Bragg reflection as shown in Fig. 6.20 for the A and B geometries. Since the experimental result of Fig. 6.20 proves that:

$$(\Delta\omega_A - \Delta\omega_B)_1 - (\Delta\omega_A - \Delta\omega_B)_2 = \Delta\varphi_1 - \Delta\varphi_2 = 0 \tag{6.51}$$

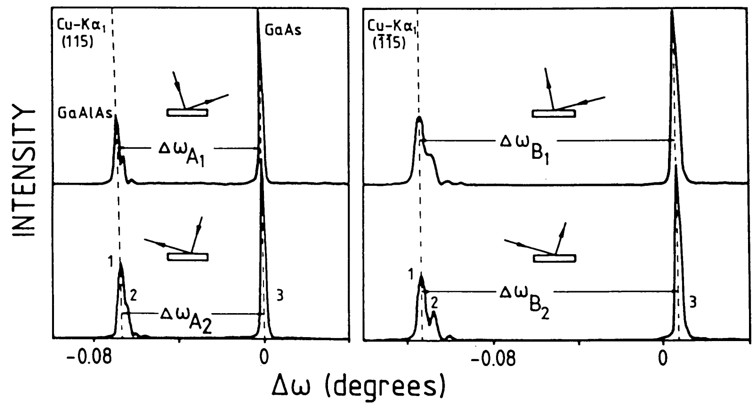

Fig. 6.20. Method for confirming the tetragonal distortion using (115) and ($\bar{1}\bar{1}5$) Bragg reflections in scattering geometries A and B (Fig. 6.17), [6.98]

the distortion is tetragonal in this case. The monoclinic angle β is given after Bartels and Nijman [6.109] by

$$\beta = \frac{\Delta\varphi_1 - \Delta\varphi_2}{\sin^2\varphi} - \frac{1}{2} \tag{6.52}$$

Meyerheim [6.98] has suggested that, based on the symmetry of a (001) plane which is D_{4v}, no monoclinic distortion is possible. However, for planes which have no higher symmetry than C_2 or C_s [like a (211) plane] it can occur and therefore also for other vicinal surface planes.

In many cases the strains in epitaxial layers are of the order of 10^{-4} to 10^{-2}. However, high resolution X-Ray techniques are capable of determining even much smaller strain values, as low as 10^{-5}. Segmüller [6.4] has reported the observation of changes in the lattice strain in AlGaAs layers heavily doped with Sn grown on a GaAs substrate due to the emission of electrons from deep level (DX-) centres upon illumination. The angular distance between high and low conductivity state changed by $\Delta\theta = -0.0010° \pm 0.0003°$ for the (400) reflection using a Cu $\mathrm{K}_{\alpha 1}$ radiation from a spot focus $1 * 1\,\mathrm{mm}^2$. The measurements were performed with a triple-axis spectrometer at low temperatures (15 K) and the strain normal to the surface was deduced which corresponded to a change of lattice parameter a of $\Delta a/a = +(14 \pm 4) \cdot 10^{-6}$. The lattice strain results from the population of the conduction band with electrons ejected from the DX centers (lattice expansion due to conduction band filling), with a concentration of about $1.5 \cdot 10^{18}\,\mathrm{cm}^{-3}$ and partly from the strain contribution from the emptied DX centres.

This beautiful example shows the standard of high resolution X-Ray diffraction which has been achieved nowadays.

6.4.2 Partial Relaxation of Strain

With increasing layer thickness the elastic energy increases. Beyond a critical value misfit dislocations are formed and the strain is partly relieved [6.110–6.112]. In such a case, for [001] growth direction, the lattice parameters of the layer are still such that $a_x = a_y$ but different from the substrate.

We define a parameter δ

$$\delta = \frac{a_{\|}^L - a_0^S}{a_0^S} \tag{6.53}$$

as a quantity measuring the partial strain relief. For complete strain relaxation $a_{\|}^L = a_0^L$ holds, where a_0^L is the unstrained lattice parameter of the layer material.

In order to determine a_0^L in such a case [for (001) growth] we use

$$a_0^L = \frac{C_{11}}{C_{11} + 2C_{12}} [a_{\perp}^L - a_{\|}^L] + a_{\|}^L \tag{6.54}$$

which corresponds to (6.39). The measurement thus proceeds like in the pseudomorphic case using asymmetrical Bragg reflections in A and B geometry as described above.

Partial strain relief leads to a graded strain profile. If reciprocal lattice scans can be performed, then the determination of the lattice constants of epitaxials layers irrespective of their strain status is straightforward as shown in the following. We consider for simplicity the growth of an epilayer along the [001] direction on a (001) substrate and assume that a_L (bulk) is larger than a_S and that the layer growth is pseudomorphic. The in-plane lattice constant of the layer is identical to that of the substrate and a tetragonal distortion occurs (Fig. 6.21).

In the partially relaxed situation (Fig. 6.21 central part) the in-plane lattice constant of the layer is larger that of the substrate but there is still

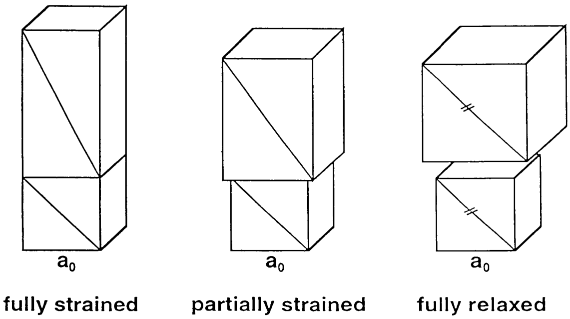

Fig. 6.21. Scheme of different strain status for an epilayer on a substrate

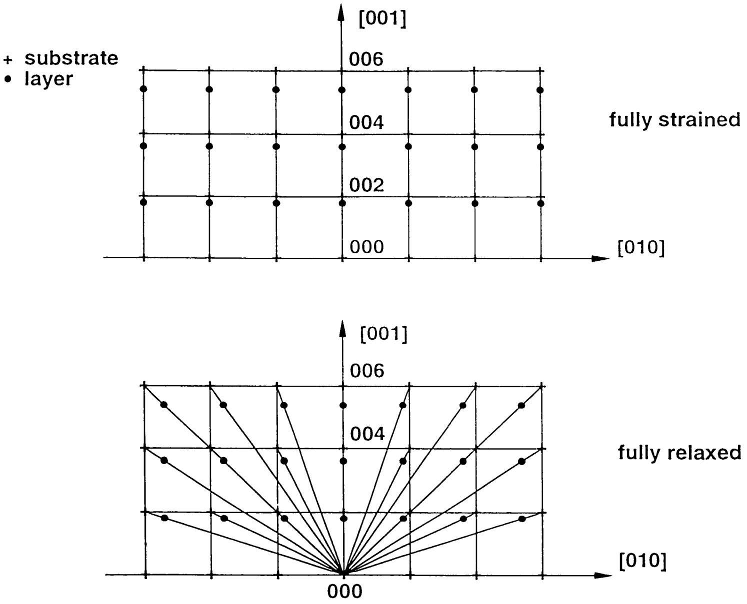

Fig. 6.22. Scheme of different strain status for an epilayer on a substrate in the reciprocal lattice

a tetragonal distortion whereas in the fully relaxed case the layer is cubic with its bulk lattice constant a_L different from a_S. In the reciprocal lattice in Fig. 6.22 the situation for pseudomorphic growth (fully strained) and for the case of full relaxation (lower part) are shown.

Since for pseudomorphic growth the in-plane lattice constants are identical, the tetragonal distortion of the layer becomes apparent from the relative positions of the layer reciprocal lattice point maxima with respect to those of the substrate. In this special cross section through the reciprocal lattice, the lattice constant of the layer along growth direction is larger than its equilibrium bulk value and larger than that of the substrate. For the fully relaxed case, the layer has regained its cubic structure and consequently any given direction within the substrate is parallel to the corresponding one within the layer as shown in the lower part of Fig. 6.22. In Fig. 6.23 we demonstrate how reciprocal space maps can be used to determine independently of each other the in-plane ($a_{\|}$) and perpendicular lattice constants ($a_{\perp}$) of an epitaxial layer without any knowledge of the elastic constants. As an example we use $\mathrm{Si}_{1-x}\mathrm{Ge}_x$ on (001) Si substrate.

For pseudomorphic layer growth the symmetrical (002) and asymmetrical (202) reciprocal lattice points of the SiGe layer are situated below, i.e. along the [001] direction, the corresponding ones of the Si substrate $\left(a_{\|}(\mathrm{Si}) = a_{\|}(\mathrm{SiGe}), a_{\perp}(\mathrm{SiGe}) > a_{\perp}(\mathrm{Si})\right)$. If the relaxation process starts, the

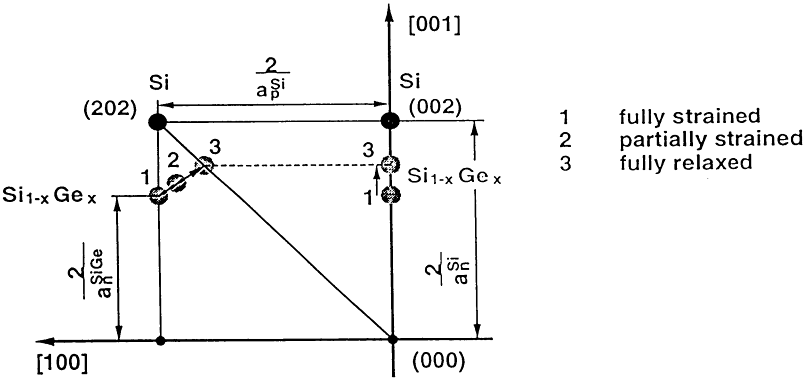

Fig. 6.23. Evaluation of lattice constants for $Si_{1-x}Ge_x$ on Si(001) without any knowledge of elastic constants

SiGe reciprocal lattice points move from the positions marked "1" to the positions "2". In the fully relaxed case, the $Si_{1-x}Ge_x$ REciprocal Lattice Points (RELP's) are at positions "3" (the [202] directions in the Si substrate and the SiGe epilayer are parallel to each other and therefore the (202) RELP of the $Si_{1-x}Ge_x$ layer lies on the line connecting the center (000) of the reciprocal lattice and the (202) RELP of the Si substrate). Finally, the reciprocal maps are ideal for detecting any crystallographic layer tilt. Using a map around a symmetrical reflection one immediately recognizes whether the layer (00*n*) RELP is situated on the line connecting the (000) origin with the substrate (00*n*) peak. If this is not the case (as shown in Fig. 6.24) the tilt angle is immediately apparent. Consequently, reciprocal space maps offer appreciable advantage for the identification of the strain status as well as of a possible tilt of epitaxial layers.

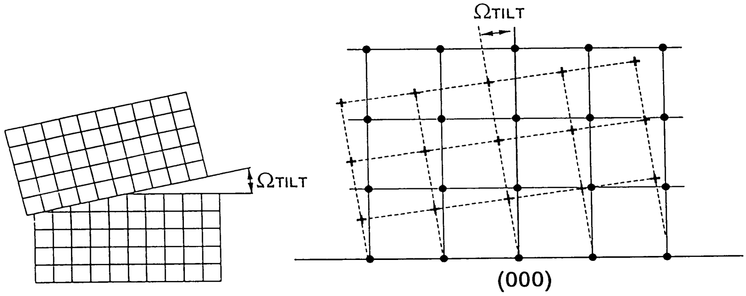

Fig. 6.24. Scheme for evaluation of tilt angle between epilayer and substrate by reciprocal lattice scans

6.5 Rocking-Curves from Heterostructures

As has been shown above in a rocking-curve from a single heterostructure, two peaks appear since the lattice constant of substrate and layer are normally different. Even if the film has the same crystalline perfection as the substrate, its diffraction peak is much broader due to the finite thickness effect discussed above. The angular distance $\Delta\omega$ between the two peaks yields direct information on chemical composition in the case of alloy semiconductors.

6.5.1 Single Heterostructures

In Fig. 6.25 a sequence of calculated diffraction patterns of AlGaAs/GaAs structures is shown for two Al contents (10% and 20%) and two different AlGaAs thicknesses ($d = 2\,\mu$m and $d = 1\,\mu$m). For the thinner AlGaAs layer the finite thickness fringes are clearly visible, as well as the shift of the AlGaAs peak due to the different chemical composition. The interpretation of X-Ray scattering from more than one epitaxial layer has usually to be based on a careful analysis, because the amplitudes of the scattered waves interfere with each other and produce complicated patterns (Fig. 6.25 lower right corner).

However, it should be pointed out that for layers with thicknesses below about $1\,\mu$m, the X-Ray diffraction method for a simultaneous determination

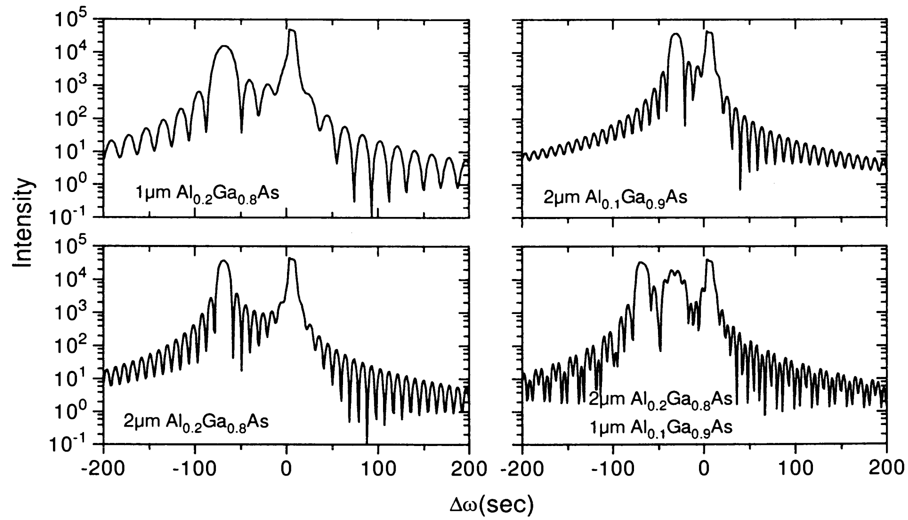

Fig. 6.25. Calculated diffraction pattern for AlGaAs layers of different compositions and thicknesses on a GaAs substrate. The lattice mismatch and finite thickness are reflected in a broadening of the main peaks and the appearance of interference fringes at characteristic positions

of alloy composition and mismatch based on the measurement of separation of diffraction peaks in the high resolution diffractograms has to be handled with care. Fewster and Curling [6.87] have reported the occurrence of a considerable peak shifting for identical mismatch between layer and substrate but different thicknesses. As the layer thickness is reduced, the layer peak shifts towards the substrate peak. Fewster and Curling [6.87] have shown that the observed peak shifts can be simulated within the solution of the Takagi-Taupin equations, but not within the kinematical approach.

This effect occurs if the layer grows coherently on the substrate, i.e. for comparatively low interfacial misfit dislocation density. As a numerical example, Fewster and Curling have shown that for a 0.2 μm layer of $In_{0.524}Ga_{0.476}As$ on InP substrate a 10% error in mismatch would occur when derived from the peak position. Consequently, care should be taken if the composition of submicrometer layers has to be determined with an accuracy better than 10%. A reliable determination of strain and knowledge of relaxation or measurements of asymmetric Bragg reflections and alloy composition thus requires the simulation of diffraction profiles.

Subtle phenomena can be deduced from the Pendellösung fringes of heterostructures as shown by Tapfer et al. [6.93]. In Fig. 6.26 three different Bragg reflections a symmetrical (004), and two oblique ones (311) and (422)

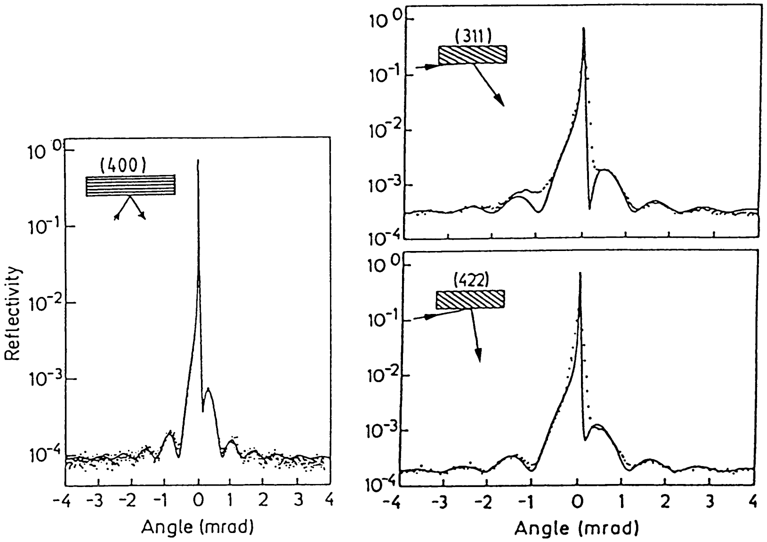

Fig. 6.26. Experimental (dotted line) and simulated (solid line) diffraction pattern of the symmetrical (400) and the asymmetrical (311) and (422) diffraction patterns of a 140 nm thick Si cap-layer deposited on 3 monolayers of Ge on Si(100) substrate. All patterns were simulated with the same parameter set [6.93]

are shown for a structure with a layer sequence: Si substrate, 3 monolayers Ge (= 0.437 nm), and on top a 140 nm thick Si layer. The Ge layers still grow pseudomorphic since its thickness is below the critical one for the formation of misfit dislocations. The Si substrate and the Si cap layer are separated by the strained Ge layers. The origin of the oscillations observed in Fig. 6.26 is the following: because the strained lattice constant of the 3 Ge monolayers in growth direction is different from the silicon one, the waves diffracted from the Si cap layer are phase shifted with respect to those diffracted from the Si substrate. The angular distance between two interference fringes is related to the cap layer thickness [6.93]. The observed spectra are compared with calculated ones based on the dynamical diffraction theory. For the same sample also asymmetric (311) and (422) diffraction patterns are shown in order to determine unambiguously the strain status. The symmetrical (004) reflection is sensitive to the lattice strain perpendicular to the layers while the two asymmetrical ones are influenced both by the lattice strain parallel and perpendicular to the layers. All three diffractograms were interpreted with the same parameter set and indeed, for the parallel strain $\epsilon_{xx} = 0$ was found, which shows that the distortion of the three Ge monolayers along the [001] direction is tetragonal. This example clearly demonstrates that the experimental data can only be understood on the basis of a rather elaborate model calculation. On the other hand it demonstrates the sensitivity of X-Ray diffraction for monolayer resolution.

6.5.2 Composition Gradients

Often the intensity oscillations accompanying the Bragg reflection of an epitaxial layer are asymmetrical. Such a behaviour always occurs if there are composition (or strain) gradients as assumed in Fig. 6.27. The calculated intensities are shown for a diffraction pattern from an one micron thick $\mathrm{In}_x\mathrm{Ga}_{1-x}\mathrm{As}$ layer deposited on InP with $x = 0.537$ corresponding to a lattice mismatch of $\Delta a/a$ of $+5 \cdot 10^{-4}$. Introducing a composition gradient the fringes become strongly asymmetric with an enhancement of the fringes on the left hand side of the peak. The In content was varied from 54.0% to 53.7% over the first $0.5\,\mu m$ and kept constant of the top $0.5\,\mu m$. An experimental example of a layer peak of 620 nm InGaAs on InP with a 1000 nm InP cap layer indicating both the composition gradient from the layer and the cap is shown in Fig. 6.28. A detailed discussion of these phenomena are given, e.g., in [6.113–6.116].

6.5.3 Characterisation of Epitaxial Layers Grown Tilted Relative to the Substrates

Often, epitaxial layers are grown on off-oriented substrates, the surface normal of which deviates from a low index crystallographic direction by as much as

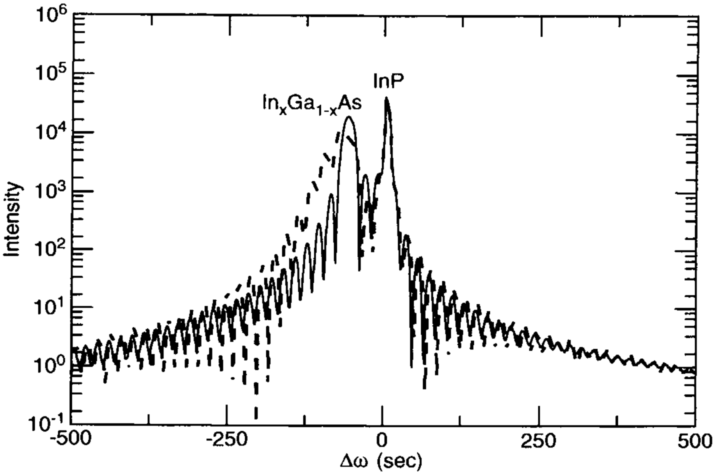

Fig. 6.27. Influence of composition gradient on reflectivity spectra. Full line: simulation of diffraction pattern of strained $In_{0.537}Ga_{0.463}As$ (1 μm) deposited on InP ($CuK_{\alpha 1}$, (004) diffraction). Finite thickness fringes are visible on both sides of the InGaAs peak. Dotted line: influence of a composition gradient within the InGaAs layer. Layer peak shape and fringe structure become asymmetric

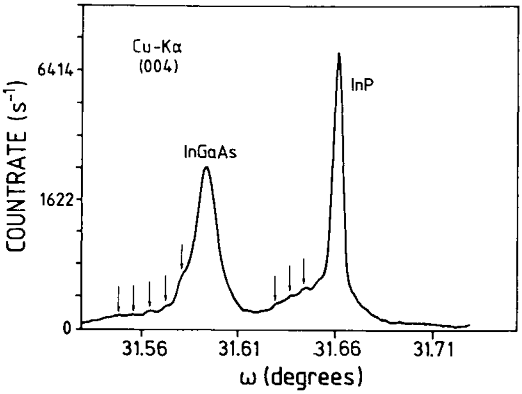

Fig. 6.28. Experimental diffraction pattern of a 620 nm thick InGaAs layer deposited on InP with a 1 μm thick InP cap layer. Finite thickness fringes yield $d = 620$ nm, asymmetric increase of reflection profile on the low angle side of the main diffraction peak indicates composition gradient [6.13]

a few degrees. As a consequence the asymmetric geometry has to be taken into account. On the other hand, epitaxial layers can also grow tilted with respect to the substrate. In both cases the experimental rocking-curves are similar and therefore difficult to distinguish. They can only be separated by use of more advanced techniques such as reciprocal space mapping. Further information on this topic is given in Sect. 6.7.

In Fig. 6.29 the diffraction pattern is shown of an $Al_xGa_{1-x}As$ layer with $x = 0.2$, grown on GaAs with a 2 degree misorientation in the nearest [110] direction. For diffraction conditions where the misorientation direction lies in the diffraction plane towards the incident X-Ray beam the full line results, whereas for the opposite orientation the dashed line would be observed. For a symmetrical Bragg reflection the asymmetry and/or tilt is easily verified by rotating the film around its surface normal: the diffraction feature exhibits a periodic modulation of peak positions. Nagai [6.118, 6.117] observed for the first time in InGaAs/GaAs layers that the epitaxial orientation was inclined relative to the substrate crystal.

He presented a model in which the tilt is a consequence of the surface steps and of the lattice mismatch. In this model the miscut direction of the substrate and the tilt direction of the epilayer are parallel to each other, the misorientation angle between the (001) planes and the substrate surface being α and the tilt angle between the substrate and epilayer planes 2β (Fig. 6.30). If the relative lattice mismatch is $\Delta a/a$, then $\tan 2\beta = \tan\alpha \cdot \Delta a/a$ (where for small α, $\cos\alpha = 1$ was taken [6.119]). The effect of the misorientation

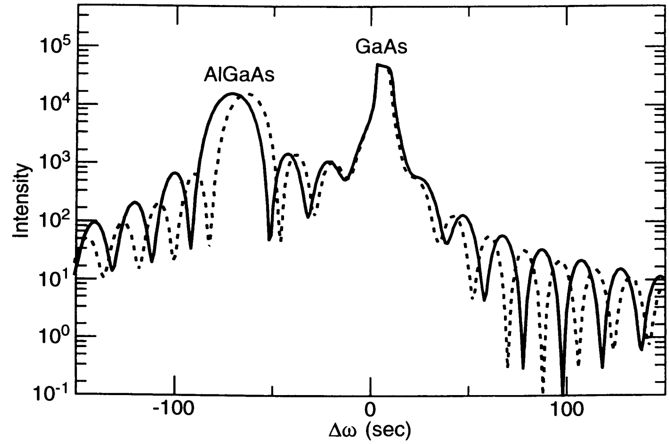

Fig. 6.29. Influence of misoriented GaAs substrate (miscut: 2°) on $Al_xGa_{1-x}As$ diffraction pattern: full line: miscut direction lies towards the incident beam and dashed line away from it. Analysis of the pattern yields two different x-values of 0.19 and 0.21 whereas the true value is 0.2

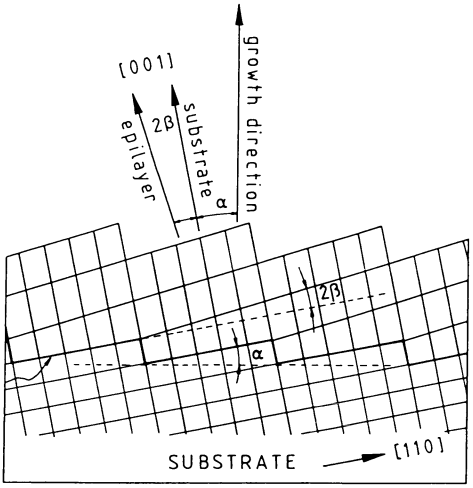

Fig. 6.30. Nagai's model for the growth of tilted layers on misoriented substrates; α is the miscut angle, 2β the tilt angle between substrate and epilayer [6.119]

angle and the step-edge orientation on the diffraction pattern of GaAs/AlAs superlattices has been studied by Auvray et al. [6.120] in order to evaluate the interface quality of the superlattice. They found that the $[\bar{1}10]$ step-edge orientation yields the best interfaces.

The validity of Nagai's model was confirmed by Neumann et al. [6.121] for the growth of GaAsSb/GaAs superlattices on GaAs, and by Auvray et al. [6.119] for $Al_xGa_{1-x}As$/GaAs heterostructures and for AlAs/GaAs superlattices. Pesek at al. [6.122,6.123] have recently studied among other systems the epitaxial orientation of ZnSe with respect to a GaAs substrate and have found that the tilt directions of the substrate and of the epilayer are not parallel but that an azimuthal rotation exists between the directions of the relative tilt and the substrate miscut. They concluded that Nagai's model is only valid for small-misfit systems where the formation of misfit dislocations is yet excluded.

In Fig. 6.31 the determination of the tilt from X-Ray data is reproduced for ZnSe/GaAs as an example [6.122]. Similar effects are of importance in the anisotropic strain relaxation of epilayer quantum well systems, e.g. [6.105, 6.124].

6.6 Multilayer Structures

In this Section the application of HRXRD to multilayers including Ewald spheres constructions for the interpretation of DCD diffractograms and scans

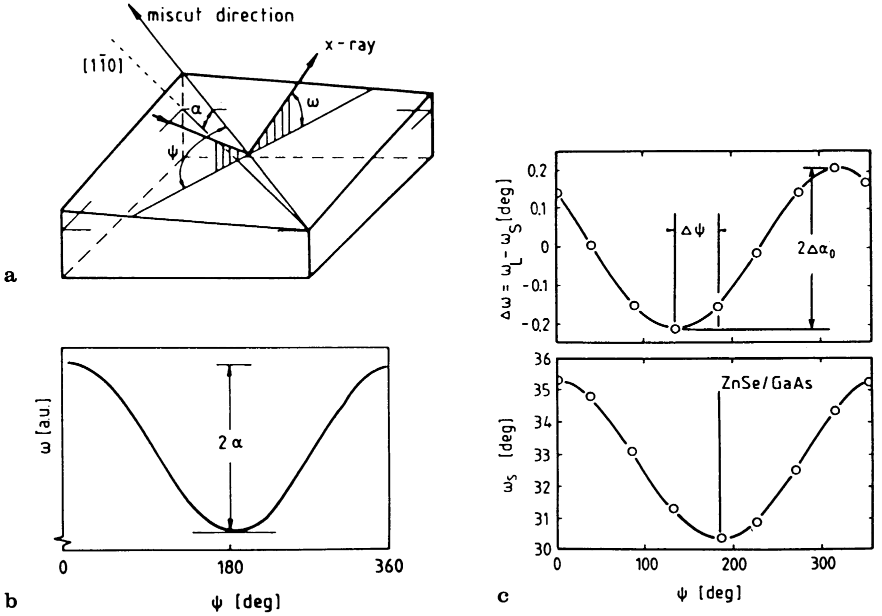

Fig. 6.31. Influence of tilted substrates on diffraction from epilayers. **a** Sketch of scattering geometry for (001) surface with [1$\bar{1}$0] miscut direction; miscut angle: α; ψ is the angle between the projection of incident X-Ray beam on the sample surface and the miscut direction; ω is the angle between X-Rays and sample surface for the Bragg condition, **b** plot of ω versus ψ exhibits periodic variation of ω with period of 360° and a modulation corresponding to 2α for $\psi = 180°$, **c** Relative tilt $\omega = \omega_L - \omega_S$ from epilayer and substrate versus ψ (upper part) and tilt of substrate versus ψ (lower part) exhibit a phase difference $\Delta\psi = 50°$ [6.122]

in reciprocal space is given. Interdiffusion of superlattices (SL's), tilt, terracing, and mosaic spread are discussed.

6.6.1 Superlattices

Artificially structured multilayers have become an important class of new materials which offer within certain limits unique electronic, optical, magnetic and mechanical properties. Along growth direction, usually two layers of different chemical composition are alternatively deposited. The one-dimensional periodicity with period D is the origin of a one-dimensional periodic potential, which is superimposed on the three-dimensional crystal potential, the period of which is determined by the lattice constants of the materials. For all properties listed above the structural perfection of a multilayer system is decisive. The X-Ray diffraction pattern of such a periodic structure consists of a series of satellite peaks accompanying the main zero-order diffraction peak along the direction of chemical modulation. The period D is given by:

$$D = \frac{(L_i - L_j)\lambda}{2(\sin(\theta_i) - \sin(\theta_j))} \tag{6.55}$$

where L_i, L_j are diffraction order indices, $\sin(\theta_i)$ and $\sin(\theta_j)$ the corresponding Bragg angles of the satellites L_i, L_j. (Note: The angular distance between adjacent satellites peaks L_i, L_j need not be equidistant, an effect which becomes important for short period superlattices). Besides the position of the main superlattice peak and of the satellites, their intensities and *FWHM*s are experimentally accessible. These data provide in principle information on thickness variations, composition and composition variations throughout the multilayer structure, interface roughness and grading, interdiffusion, and strains within the layers. We start with a perfect superlattice structure of a finite total thickness and abrupt interfaces. We consider a periodic sequence of layers of materials A and B with layer thicknesses d_A and d_B, the period $D = d_A + d_B$. The lattice parameters of the two materials along growth direction are a_A and a_B. The structure consists of N periods as shown in Fig. 6.32. A rectangular, i.e. abrupt profile of the layer sequences along growth direction is assumed. In order to illustrate the diffraction pattern in a simple way, we use the fact that the real space and the reciprocal space are related to each other via a Fourier transformation. For the intensities the kinematical approximation is used.

In a one-dimensional approximation the period D is represented by a function $f(z)$ which describes the periodic scattering centers by the atomic form factors (which are different in materials A and B). In kinematical approximation the scattering intensity is proportional to the $FF^*(k)$ where $F(k)$ is the Fourier transform of $f(z)$. $f(z)$ is described as a sum of two functions $f_A(z)$ and $f_B(z)$. In real space, these two functions are now presented as multiplications, convolutions and summations according to Fig. 6.32. The slit functions with slits z_1 and z_2 are multiplied with a Dirac comb (a_A, a_B) and are convoluted with δ-function Dirac combs of separation D. The contribution from the two components A and B are added and are finally multiplied with a rectangular function ($N \cdot D$).

The diffracted intensity is obtained by Fourier transformation of these functions and given by $[F_A(k) + F_B(k)]^2$, where F_A, F_B are the Fourier transforms of $f_A(z)$, $f_B(z)$. For sufficiently large difference between a_A and a_B a diffraction pattern results which is shown in Fig. 6.32.

The main SL maxima appear close to $2\pi/a_A$ and $2\pi/a_B$ accompanied by satellites, the width of which is given by $(4\pi/N \cdot D)$. The separation between two subsequent maxima is given by $2\pi/D$ and the width of the envelope function depends on $4\pi/d_A$ and $4\pi/d_B$; n_0 denotes the diffraction order [6.125]. The angular position of the zeroth order superlattice peak in such a strained-layer situation corresponds to a lattice constant determined

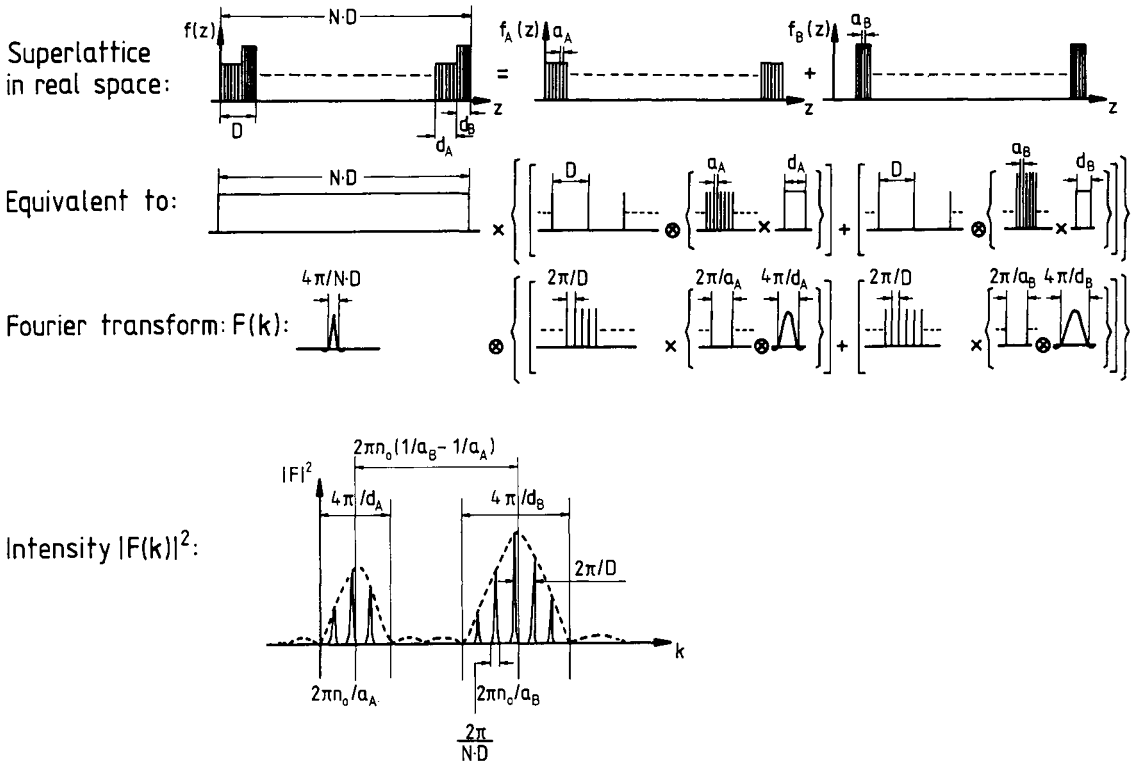

Fig. 6.32. Schematic description of the diffractionΩprofile of a superlattice in terms of a Fourier analysis: It is assumed that the SL is perfect and consisting of N periods of double layers with period D $(= d_A + \delta d_B)$ with lattice constants along z-direction a_A and a_B and two different scattering factors [6.125]

by $(d_1 a_A + d_2 a_B)/(d_1 + d_2)$ where d_1 and d_2 are the layer thicknesses of materials A and B in one period and a_A, a_B represent lattice constants in growth direction. Of course, the zero-order SL peak must not be the one with the highest intensity. For growth along [100] direction, and tetragonal distortion Nakashima [6.126] has derived a procedure for finding its position (see also [6.127]): For the (h00) oriented substrate the angular distance from a SLS peak to the substrate peak is plotted vs. h^2 for several reflections (hkl). Only the zero-order peak shows a straight line through the origin.

An experimental example for this situation is shown in Fig. 6.33. It shows a $\omega - 2\Theta$-scan of the (004) Bragg diffraction of a Si/SiGe superlattice grown on a SiGe buffer ($x = 0.25$) of 2000 Å thickness on top of a (001) oriented Si wafer. These data illustrate the structures which are expected in a strained layer superlattice. The lattice constant mismatch between Si and $Si_{0.5}Ge_{0.5}$ is about 2%. Since the Si content of the buffer is 25%, the Si layers of the SL and the SiGe layers are strained symmetrically: the Si layers are under biaxial tension and the SiGe layers under biaxial compression. Both the Si-layers of the superlattice and the SiGe layers give rise to their own sub-satellite structures. The indexing in this Figure should not be confused with that of the entire superlattice stack, i.e. the actual zero order peak in the sense of the above discussion appears at an angle of about 68.790°.

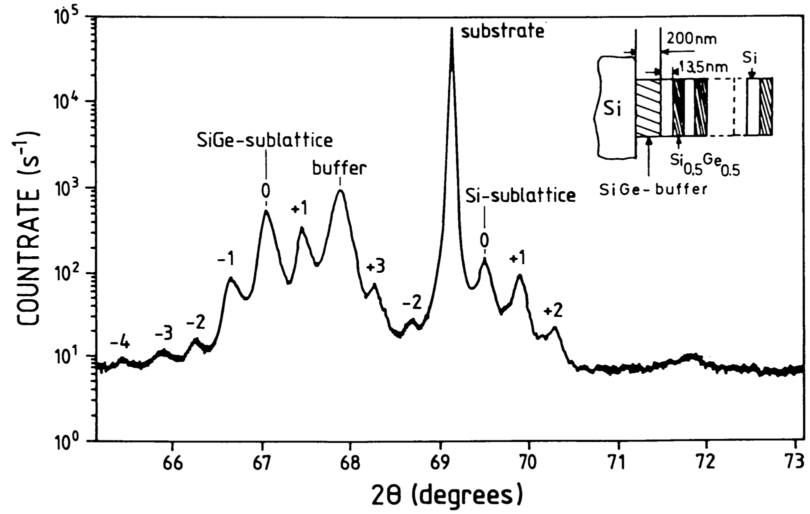

Fig. 6.33. Si/SiGe SL deposited on a SiGe buffer (D = 270 Å, d_A = 135 Å, d_B = 135 Å), 10 periods. Main peak corresponds to the Si substrate, the buffer peak is due to the SiGe alloy and 2 SL systems, one compressive (biaxially) strained SiGe sublattice and one tensile strained Si sublattice of the superlattice, taken in a $\omega - 2\Theta$ scan

This Si/SiGe superlattice is an example for a non-perfect strained-multilayer structure with quite a limited number of satellite peaks observable (see Sect. 6.6.4).

As shown in Sect. 6.5.1 also the rocking-curves of simple heterostructures exhibit fringes corresponding the layer thicknesses involved. Macrander et al. [6.167] applied Fourier transformation for extracting the thicknesses of a InP/InGaAsP/InP double heterostructure.

At this point we would like to emphasize the importance of the X-Ray optics used for the evaluation of full width of half maxima of diffracted X-Ray peaks, since such quantities are quite often used as a first indication of the structural quality of epitaxial layers and superlattices. In the following we compare two $\omega - 2\Theta$ scans of a PbTe/EuTe superlattice grown on BaF_2 substrate along the [111] direction, one recorded with DCD optics and the second one with Triple-Axis Diffractometry (TAD) optics. In both cases a Philips MRD materials research diffractometer employing $CuK_{\alpha 1}$ radiation with a four-crystal Bartels monochromator (set for the (220) Ge reflection mode) in the primary beam was used. For the DCD optics the detector had an opening angle acceptance of 2 degrees. For the TAD optics a channel-cut two-reflection Ge (220) analyser crystal was used in the secondary beam which results in a beam divergence of 12 arcsec and in a high resolution reciprocal space probe as compared to the extent of the RELP's of interest. In Fig. 6.34 the $\omega - 2\Theta$ diffraction curve of the symmetrical (222) Bragg reflection of the PbTe/EuTe SL using DCD optics is shown.

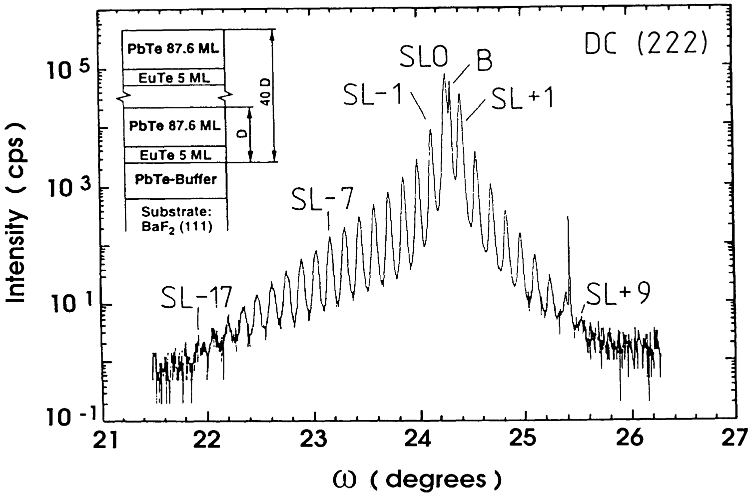

Fig. 6.34. Double-crystal rocking-curve ($\omega - 2\Theta$ scan) for the (222) Bragg reflection of a PbTe/EuTe SL (insert with the structural parameters). B denotes the PbTe buffer, SL-17 to SL+8 denote the superlattice satellite reflections [6.128]

The insert shows the nominal structural parameters of the sample. In the double-crystal rocking-curve besides the BaF_2 substrate and the PbTe buffer (B) peaks a large number of superlattice (SL) satellites (SL-17 to SL8) are clearly resolved and few more appear in the background noise. The *FWHM* of the main diffraction peaks are 26 arcsec for the substrate, 42 arcsec for the PbTe buffer, and 102 arcsec for the zero order superlattice peak. These *FWHM* values deduced from the DC rocking-curve are strongly influenced by the limited DCD resolution. In the following Fig. 6.35 the corresponding $\omega - 2\Theta$ triple axis diffractogram, i.e. using the analyser crystal is shown, which clearly demonstrates the much higher instrumental resolution in comparison to the DC rocking-curve.

However, because of the lower X-Ray intensity at the detector a smaller number of satellites can be observed. The *FWHM*s of the diffraction peaks correspond now much better to the real broadening along the $\omega - 2\Theta$ direction, i.e. the growth direction (i.e. 8 arcsec for the BaF_2 substrate, 17 arcsec for the PbTe buffer and 47 arcsec for the SL0 peak). In this Figure also a simulation of the (222) Bragg diffraction curve based on dynamical scattering theory is shown.

An example of a diffraction from a perfect GaAs/AlAs structure is shown in Fig. 6.36. It consists of 710 Å thick GaAs layers and 107 Å thick AlAs layers with 50 periods and shows the (002) diffraction.

The separation of satellite peaks corresponds to a period of 817 Å. One recognises that satellite extrema up to the order $i = \pm 32$ are observable. The envelope of the satellite intensities oscillates due to the final thickness

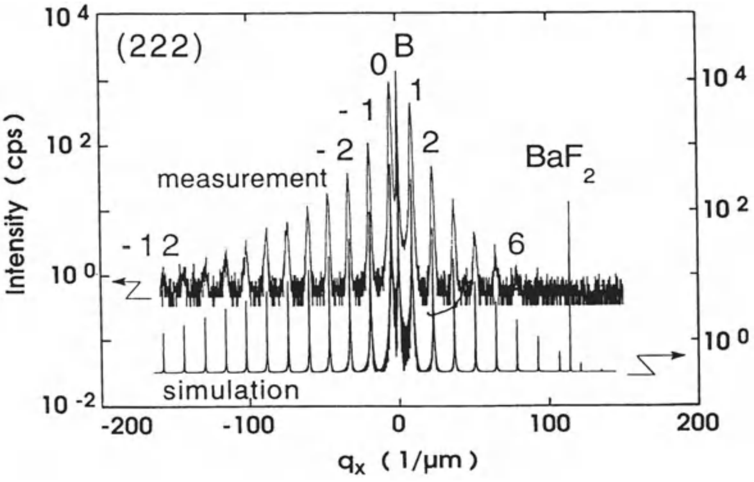

Fig. 6.35. (222) Bragg reflection triple axis rocking-curve ($\omega - 2\Theta$ scan) of the PbTe/EuTe SL shown in Fig. 6.34 with simulation based on dynamical scattering theory [6.128]

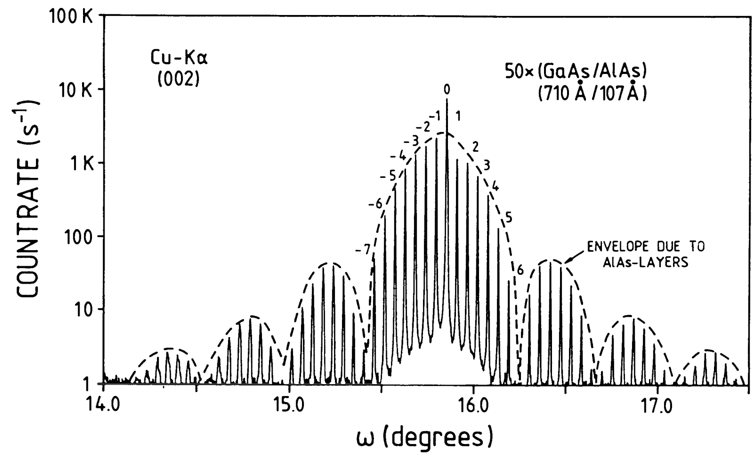

Fig. 6.36. High resolution X-Ray (002) diffraction of a GaAs/AlAs, ($d_A = 710$ Å, $d_B = 107$ Å) SL with 50 periods showing satellite peaks up to $i = 32$ in an $\omega - 2\theta$ scan. The modulation of the intensities due to an envelope function results from the 107 Å thick AlAs layers since their (002) structure factor is much stronger than that of the GaAs layers. The finite thickness fringes of the AlAs layers cause a spacing approximately eight times as large as that of the superlattice peaks [6.13]

fringes caused by the 107 Å thick AlAs layers which are observable strongly in the (002) Bragg peak since in this case the AlAs structure factor is much stronger than the corresponding GaAs one. The envelope of the superlattice peaks exhibits minima with a spacing approximately eight times as large as that of the satellite peaks.

In strained layer superlattices deposited on a substrate whose lattice constant deviates considerably from the mean SL constant, the intensity distribution turns out to be asymmetric with respect to the $i = 0$ SL peak. Interfacial strain as e.g. caused by introducing monolayers with appreciably different bond lengths than those found on the average in the SL, lead to quite substantial intensity enhancements of higher order satellite peaks as shown in the subsequent Figures.

The extremely high sensitivity of the envelope function to small fluctuations within the layer sequence of the interfaces has been exploited by Vandenberg et al. [6.129, 6.130] to study the presence of interfacial strain at heteroepitaxial interfaces.

At GaInAs/InP interfaces the strain already results from the different group V atoms at both sides of the interfaces without interdiffusion.

The net interfacial strains are caused by the different bond length in arsenic or phosphorous containing compounds. It turns out that X-Ray diffraction is particularly useful to investigate these interfacial strains as shown in Fig. 6.37 [6.131]. For a layer sequence InP/GaInAs/InP the interfaces can

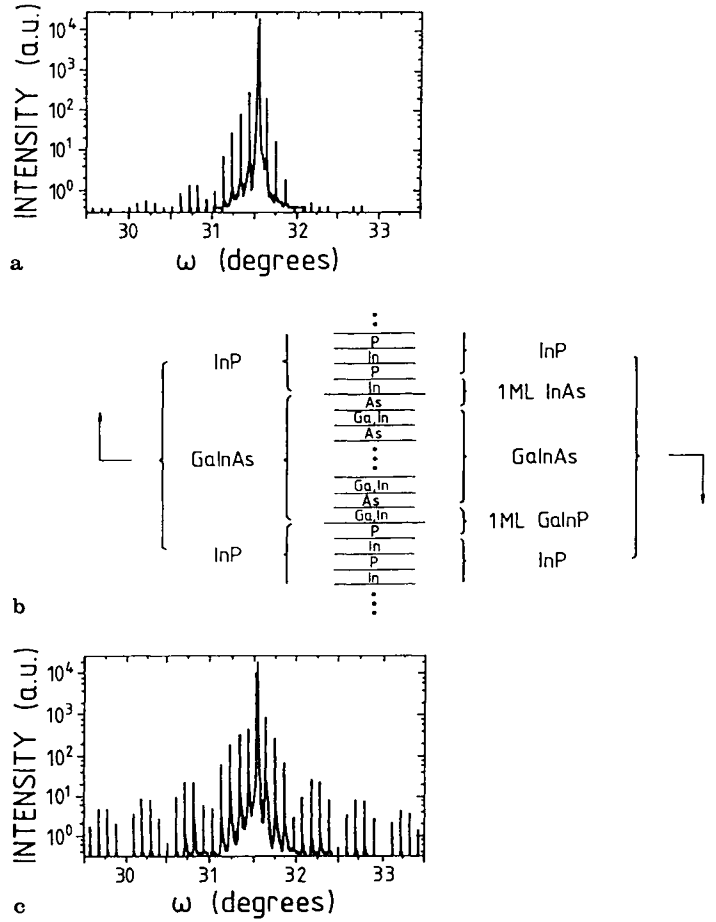

Fig. 6.37. Simulated diffraction patterns in the vicinity of the (004) reflection of a 20 period superlattice consisting of 10 nm thick $Ga_{0.46}In_{0.54}As$ and 40 nm thick InP layers on InP(001) substrate (**a**), same structure, but including additional InAs and GaInP monolayers (**c**) as indicated in (**b**) [6.131]

be defined either as indicated in the left hand part of the central panel of Fig. 6.37 or as shown in the right hand part where at the interfaces one monolayer of InAs or GaInP is introduced. In the simulated X-Ray diffractograms the two cases lead to completely different patterns. The monolayers of InAs and GaInP are strongly lattice mismatched to both InP and the lattice matched GaInAs. Consequently, a similar situation is encountered as already discussed by Tapfer et al. [6.93] (see Fig. 6.26) for Si/Ge/Si. InAs, having a larger lattice constant than InP is under biaxial compressive strain whereas the GaInP layer is under biaxial tensile strain. However, above the

GaInP layer, the subsequent GaInAs layers have the correct lattice constant in comparison to InP, but with slightly shifted atomic positions. Therefore the wave fields from the InP layers below and from the GaInAs layers above the GaInP monolayer are shifted in phase with respect to each other and a similar effect is encountered by the InAs monolayer. Figs. 6.37a,c show the dramatic consequences of the two monolayers on the X-Ray diffractogram.

Vandenberg et al. [6.130] were able to show that high resolution X-Ray diffraction is capable of quantitatively identifying these strains, based on a comparison of experimental data of a $D = 534\,\text{Å}$ SL with 10 doublelayers of InGaAs/InP (Fig. 6.38). Therefore the satellite reflection (up to $i = \pm 34$) are closely spaced. The envelope of the intensities critically depends on strains through the relative shift of atomic positions in the repeated unit cells. In a computer simulation of the diffracted intensities one takes the interfacial strains across the InGaAs/InP into account by incorporating a negative strain producing monolayer at the InP to InGaAs interface and a positively strained monolayer in the InGaAs to InP interface. The interface spacing on one side is 1.4261 Å and on the other side 1.5347 Å. The total number of layers is $N_{\text{InP}} = 310$ and $N_{\text{InGaAs}} = 54$, i.e. it is important that d_A is quite different from d_B in order to produce the envelope intensity variation and consequently different macroscopic net strains on both sides of the interfaces, ($\epsilon_{\perp}^{+} = +4.6\%$, $\epsilon_{\perp}^{-} = -4.6\%$).

The formation of interfacial InAs-, InAsP-, GaInP- or GaInAsP layers in nearly lattice matched InGaAs/InP structures is also very likely due to an exchange of group V elements during the gas switching procedure in Metal

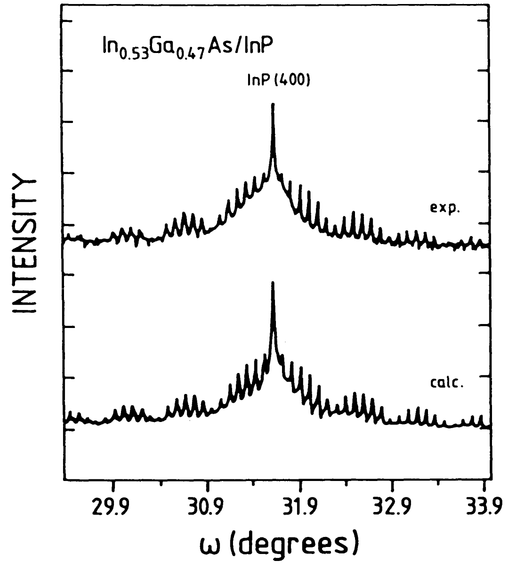

Fig. 6.38. Diffraction scan of a $In_{0.53}Ga_{0.47}As$/InP superlattice ($D = 534\,\text{Å}$, ten periods). In the best fit $N_{\text{InGaAs}} = 54$ monolayers are assumed with one strained monolayer at each interface. The simulation includes interfacial strain in the closely lattice matched $In_xGa_{1-x}As$/InP SL (ϵ^{+}, ϵ^{-}) and small linear decrease of the number of InP monolayers N_{InP} from 314 to 306 [6.130]

Organic Vapour Phase Epitaxy (MOVPE) or due thermal interdiffusion. X-Ray diffraction is a valuable tool in identifying interlayers in the sequence of the whole stack of layers. Figure 6.39 shows an X-Ray diffractogram of a multilayer structure designed for an optical switch application in the 1.55 μm range [6.132]. This structure consists of an InP substrate, an InP buffer layer (0.2 μm) and a multilayer structure with a period of 10 nm (InGaAs/InP) double layers, and of a second multilayer structure with a period of 105 nm (which involves the first one (InGaAs/InP) and an additional 55 nm InP layer). On top an InP cap layer is deposited. The experimentally observed diffraction pattern is quite intricate with apparently different periods on the low and

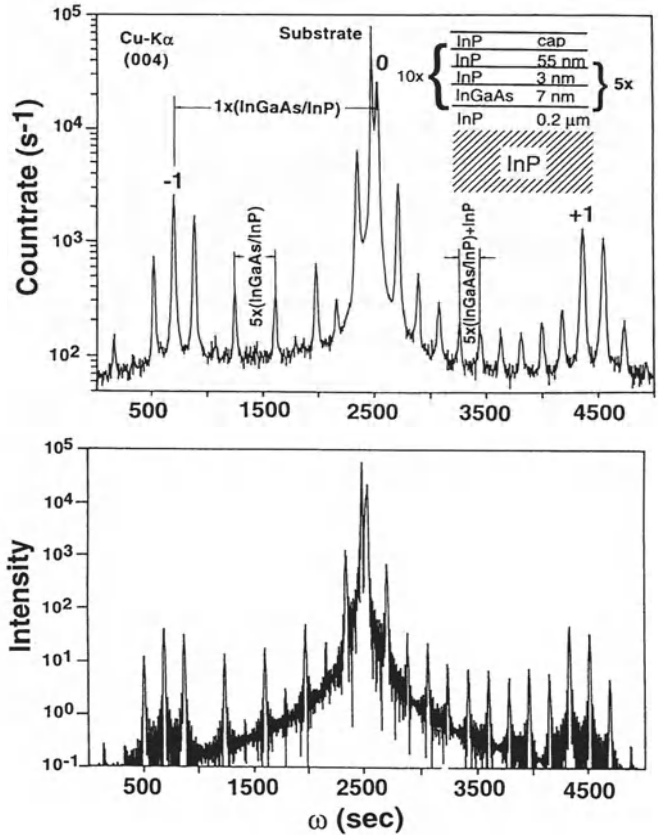

Fig. 6.39. Upper panel: experimental diffraction pattern of an InGaAs/InP MQW-layer structure with three different periods as shown in the insert. Lower panel: best fit to the experimental spectrum. The asymmetric diffraction pattern can only be simulated by introducing InAs or InAsP and InGaP or InGaAsP monolayers at the lower and upper interfaces, respectively [6.132]

high angle side of the substrate peak. The different periods in the structure are clearly observable:

The SL peaks $i = \pm 1$ represent the period of the 10 nm thick double layers. On the low angle side of the $i = 0$ SL peak, the total thickness of the InP/InGaAs SL ($d_{\mathrm{total}} = 50\,\mathrm{nm}$) causes intensity fringes to appear. Finally on the high angle side of the main peak the satellite peaks of the other SL appear with a period $D = (5 * 10 + 55)\,\mathrm{nm} = 105\,\mathrm{nm}$. This characteristic envelope function allows for an unambiguous determination of the interfacial strain distribution along the growth direction as shown by model calculations based on the dynamical theory. A calculated pattern is shown in the lower part of Fig. 6.39. The calculations clearly show that the experimental pattern can only be simulated when strain-creating interfacial layers are introduced, which is a well known phenomenon in this material system. Figure 6.40 shows

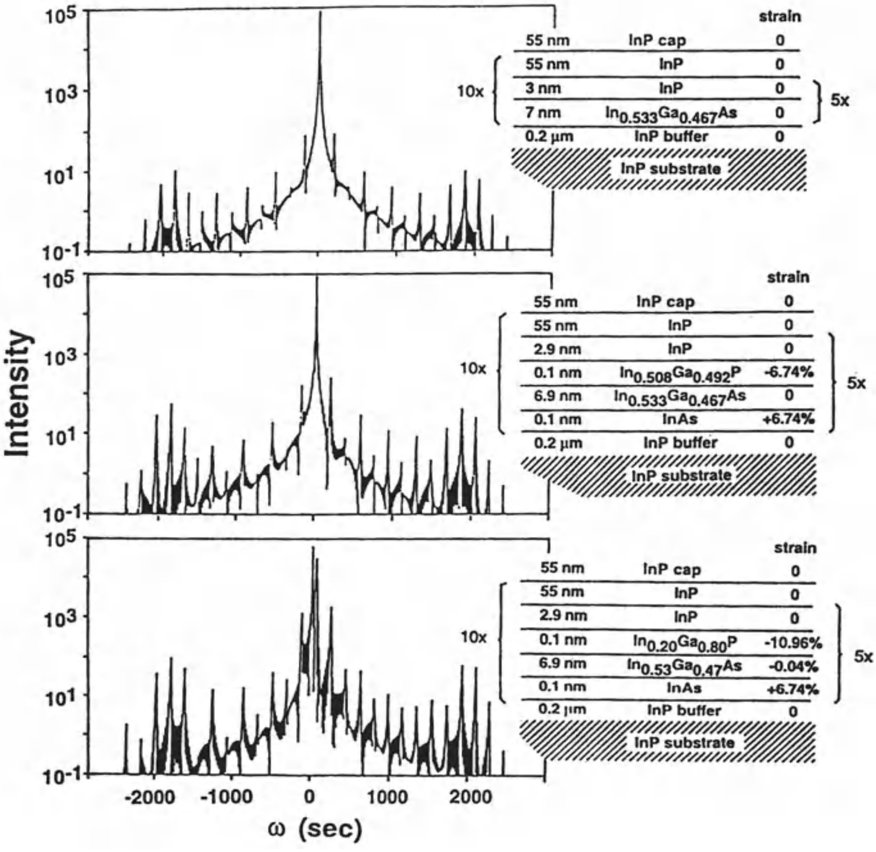

Fig. 6.40. Simulation procedure of Fig. 6.39: upper panel: without any strain; central part: including symmetric interfacial monolayers and lower panel: with asymmetric interfacial monolayers (see text) [6.132]

the different stages of the simulation. Firstly, the structure is simulated as designed, without any strain. The pattern is completely symmetric and the main satellite peaks being much too low in intensity (upper panel). The intensity of the satellite peaks can be increased symmetrically by introducing interfacial monolayers with height of same magnitude but opposite sign at both the InP-to-InGaAs and InGaAs-to-InP heterointerfaces (central panel). In the next step (lower panel) the envelope function is influenced by introducing interfacial monolayers of asymmetric strain. In order to get similarity with the experimental spectrum the nature of the interfacial strain must be compressive at the InP-to-InGaAs interfaces and tensile at the InP-to-InGaAs ones. This situation can be verified by introducing a material whose lattice constant is smaller than that of InP between InGaAs/InP and a material with a larger lattice constant between InP/InGaAs. A negatively mismatched GaInAsP or GaInP monolayer at GaInAs-to-InP and a positively mismatched InAs or InAsP monolayer at InP-to-InGaAs fulfill these requirements. In the latter case the best fit is obtained with the highest strain possible ($\epsilon_\perp^+ = +6.74\%$), i.e. with pure InAs monolayers. At the upper interface a higher strain value is needed for an optimal fit, i.e. $\epsilon_\perp^+ = -10\%$. Such high strain can be generated by lowering the In concentration. Thus from X-Ray analysis the interfacial strain distribution along growth direction was deduced. Interfacial layers are also needed in order to fit ellipsometric data on such samples [6.133]. Quite recently, similar measurements were performed on GaInP/GaAs superlattices on GaAs substrate using the (002) diffraction [6.134]. The example demonstrates how much information in particular also on subtle epitaxial growth processes can be extruded from HRXRD.

The numerical simulation of rocking-curves is becoming more and more important. Several companies (Philips, Bede, Siemens, etc) offer program packages. Herres et al. [6.135] have described a program `Simulat` which calculates strain parameters based on Segmüller-Murakami [6.99], Fewster's [6.87] version of the dynamical X-Ray diffraction theory for reflection and convolves the theoretical rocking-curves with the monochromator function for a comparison with the experimental data.

6.6.2 Ewald Sphere Construction of SL-Diffraction Diagrams

In a periodic multilayer structure all reciprocal lattice points (*hkl*) are accompanied by satellite points, along the direction which corresponds to the growth direction [6.60, 6.136, 6.137], i.e., strictly spoken, along the direction of chemical modulation.

The Ewald sphere construction for a symmetric Bragg reflection (002) of a superlattice is shown in Fig. 6.41. Along the direction of wavevector transfer, i.e. $\mathbf{G}_{hkl}$ the satellite peaks are present. These are broadened and elongated along the perpendicular direction (i.e. parallel to the surface plane) due to the presence of disorder, i.e. misfit dislocations. The broadening along the

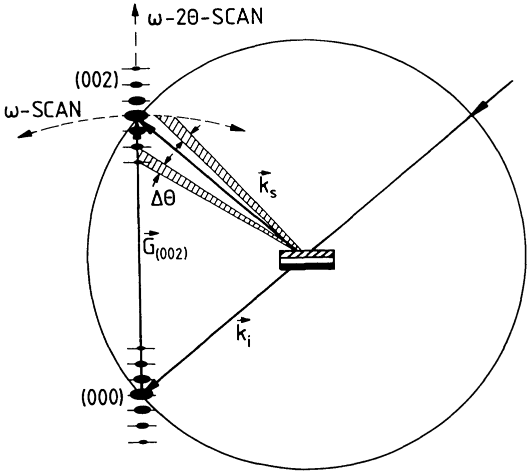

Fig. 6.41. Ewald sphere construction for (002) Bragg diffraction of a SL grown along [001] direction showing satellite reciprocal lattice points accompanying the main (*hkl*) sites. In an $\omega - 2\Theta$-scan the satellite structure is probed along the direction of **G** whereas in a typical rocking-curve an ω-scan (dashed curve) is performed with open slits in front of the detector corresponding to a certain angular spread around the scattered wavevector $\mathbf{k}_s$

growth direction results from the finite number of lattice planes contributing to the interference pattern. The extent of broadening and elongation can be measured by properly choosing both the scan mode and the Bragg diffraction angle. The procedure is outlined in the following Figures where diffracted intensities vs. angles 2θ or ω are plotted together with the corresponding Ewald sphere construction.

As an example a rather imperfect PbTe/PbSnTe superlattice with a period of 285 Å is chosen. Due to the BaF_2 substrate, which is lattice mismatched (about 4%) and in addition not of high crystalline perfection, the superlattice is distorted by misfit dislocations and mosaic structure which contribute to broadening of the reciprocal lattice points. Nevertheless in the symmetrical (222) $\omega - 2\Theta$ scan (Fig. 6.42) a satellite structure is clearly resolved, since for this scan mode the wavevector transfer is along the growth direction.

However, in an ω-scan of the same (222) Bragg reflection of the sample, the $i = \pm 2i$ satellites are barely visible and the $i = \pm 1$ ones are strongly broadened. The buffer peak and the $i = 0$ SL peak have merged together (Fig. 6.43).

In the reciprocal lattice, as shown in Figs. 6.42, 6.43 these facts can be explained with the help of the Ewald sphere considering the different scans in the $\omega - 2\Theta$ (Fig. 6.42) as well as in the ω mode (Fig. 6.43). Provided that the small angle grain boundaries are mainly oriented parallel to the growth

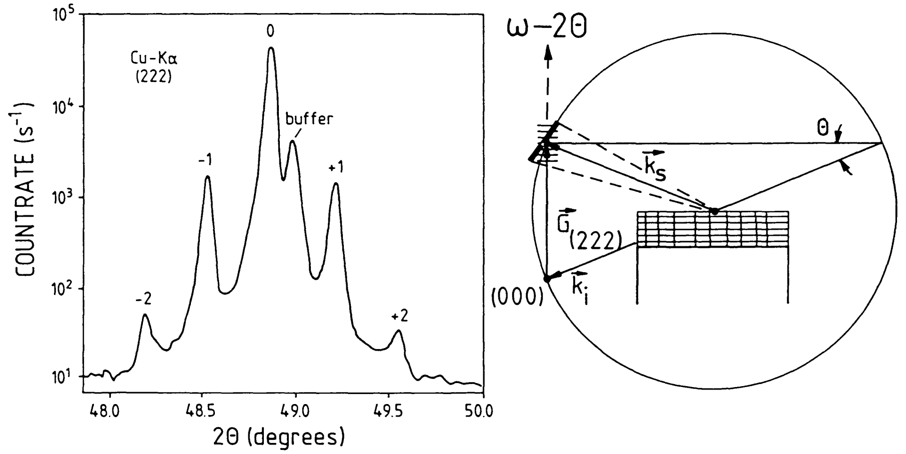

Fig. 6.42. An ω-scan of a PbTe /Pb$_{1-x}$Sn$_x$Te SL deposited on a Pb$_{1-x}$Sn$_x$Te buffer ($x = 0.18$, period $D = 285$ Å) of a (222) Bragg diffraction. The broadening of the reciprocal lattice points in direction perpendicular to the scan mode is due to misfit dislocations

direction the broadening of the SL satellites will not become effective in a scan mode along the **G**-direction for a symmetrical reflection (Fig. 6.42). However, for the ω-scan the SL is probed along the $\mathbf{k}_S$ direction as indicated in Fig. 6.43, upper panel, and several SL-points contribute to the registered Bragg diffraction. Choosing scattering geometry with $\mathbf{k}_S$ approximately parallel to the growth direction, i.e. for that case a (264) Bragg diffraction for which $2\Theta = 126.6°$ and $\omega = 40°$ ($2\Theta - \omega \cong 90°$) produces in the rocking-curve a well resolved satellite SL-structure in an ω-scan (Fig. 6.43, central panel). For that diffraction, the broadening of the reciprocal lattice points parallel to the superlattice planes does not contribute to the observed diffraction pattern. The peak broadening is also influenced by interdiffusion in addition to the effects mentioned earlier.

This information on the extent of the reciprocal lattices points in various directions in reciprocal space are confirmed by choosing a scattering geometry which probes the extension of the reciprocal lattice points along a proper direction which is perpendicular to the growth direction. This is the case for a (062) Bragg reflection with an ω angle of 92.3° and a 2θ of 97.5° ($2\theta - \omega \cong 0°$). In the ω-scan no satellite at all is visible and in the corresponding Ewald sphere plot, the contribution from all satellites are recorded simultaneously for all ω-positions (Fig. 6.43, lower panel). In all the diagrams illustrating the ω-scans in the reciprocal lattice, the finite dispersion, i.e. the angular range of scattered wavevectors $\mathbf{k}_s$ is indicated by dashed lines. This example illustrates the importance of the proper selection of diffraction conditions. The choice of the (264) and (062) Bragg peaks is optimal for the investigation of layers

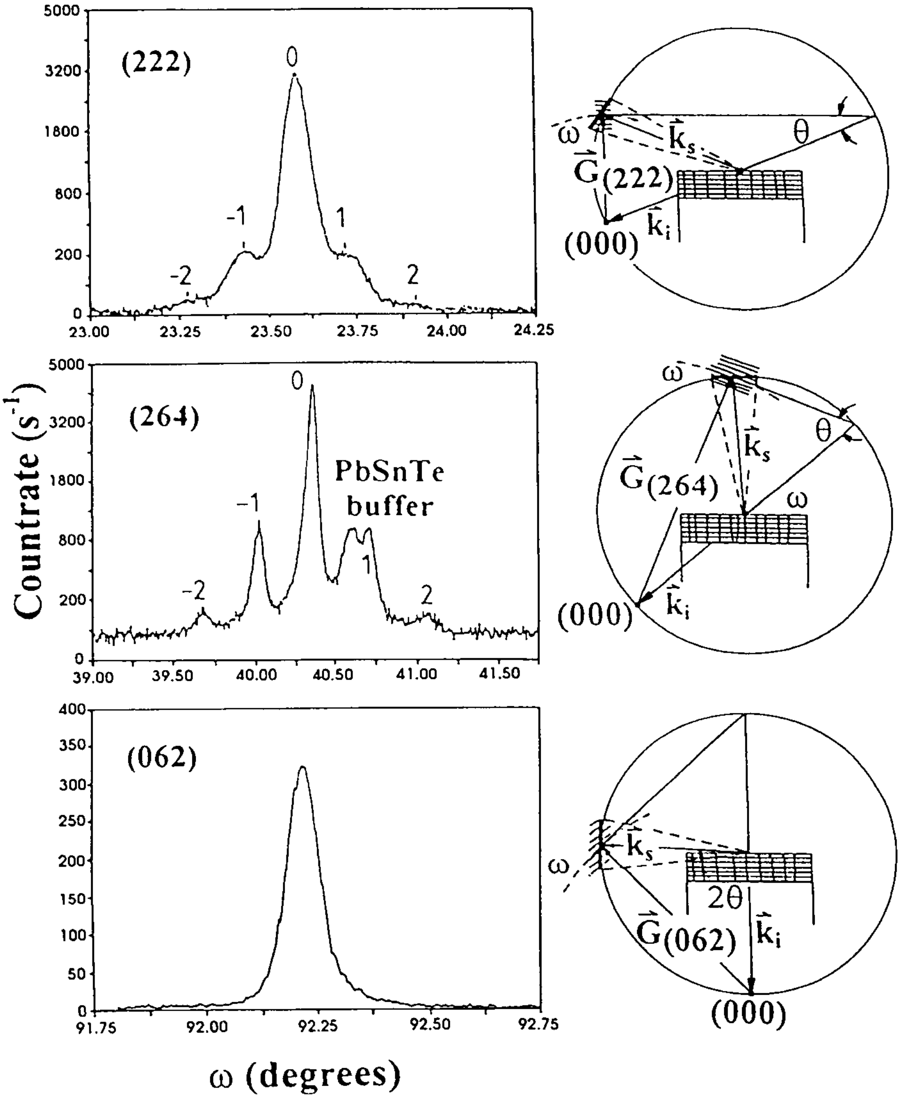

Fig. 6.43. As Fig. 6.42 but for ω-scans for (222), (264) and (062) diffractions. In the symmetric (222) case the satellites are barely resolved since the rocking-curve is taken with wide open slits in front of the detector during the scan. For the (264) diffraction the SL satellites are well resolved (see reciprocal lattice for explanation) whereas in the (062) geometry all satellites contribute at the same time to the reduced intensity for various ω angles

grown in the [111]-direction. In general, the resulting shape of the rocking-curve depends both on the amount of mosaicity and the (*hkl*) of the reciprocal space probe.

The broadening of the scattering intensity thus immediately yields information on the extent of the reciprocal lattice points parallel to the growth direction which is not influenced by the finite-layer thicknesses.

Therefore, by performing measurements with several Bragg diffractions one can uniquely get information on the orientation dependence of the broadening with respect to the growth direction. Such data are necessary for a determination of the real structure (mosaic structure due to small angle grain boundaries, misfit and threading dislocations) of epitaxial films.

6.6.3 Interpretation of the Fine Structure in X-Ray Diffraction Profiles of SL's

In highly perfect SL's, between the satellite peaks, additional extrema can be observed as shown in Fig. 6.44. A (004) Bragg diffraction of a Si/SiGe SL

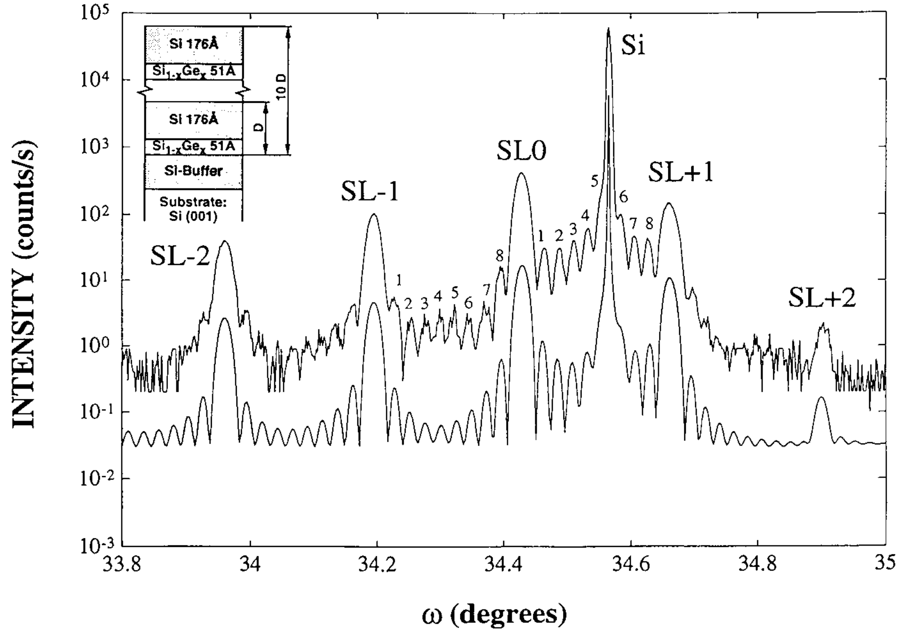

Fig. 6.44. HRXRD of Si/SiGe superlattice deposited on (001) oriented Si. SL period $D = 227$ Å with 10 double layers corresponding to a total thickness of 2270 Å. The number of secondary maxima in-between the main SL satellite peaks is $10 - 2 = 8$

on a Si buffer and thus highly strained with a total thickness of 2270 Å is shown. Expanding the ω-scale additional maxima appear between the main satellites. The SL period for the spacing for the $i = 1, 2, 3, \ldots$ SL satellites is found to be 227 Å, i.e. there are 10 double layers of SiGe. The evaluation of the distance between the fringes accompanying the SL satellites yields a total thickness of about 2270 Å. We would like to point out that between two subsequent satellites there are $N - 2$ side maxima $(10 - 2 = 8)$ which follows from classical diffraction physics for a diffraction grating consisting of N slits.

The intensity of the subsidiary maxima between the main satellite peaks turns out to be extremely sensitive to irregularities in the period. As Powell et al. [6.138] have shown for a Si/Ge SL, a small dispersion in the SL period in the order of 2% causes quite drastic changes in the pattern of the subsidiary maxima, whereas the width of the main satellites is still unaffected.

6.6.4 Imperfect MQW's and Superlattices

Real MQW and SL samples exhibit a number of imperfections which result from the growth procedure itself like interdiffusion, compositional and thickness fluctuations. In the following the consequences of these imperfections on the diffraction profiles are discussed.

6.6.4.1 Interdiffusion in MQW's and SL-Systems. From the intensity of the satellite peaks of X-Ray diffractograms already Fleming et al. [6.83, 6.139, 6.140] have determined the abruptness of the transition region between GaAs and AlAs layers in $(\mathrm{GaAs})_n(\mathrm{AlAs})_m$ superlattices. Later this technique has been applied by Arch et al. [6.141] for a study of interdiffusion in HgTe-CdTe superlattices and recently by Hogg et al. [6.142] for $\mathrm{Cd}_{1-x}\mathrm{Mn}_x\mathrm{Te}/\mathrm{CdTe}$ multilayers. If a rectangular modulation of the chemical composition across the interfaces is assumed without change of the SL-period D, the compositional modulation $c(z)$ is described by a Fourier series:

$$c(z) = c_0 \left[1 + \sum_m Q_m \cos\left(\frac{2\pi m z}{D}\right) \right] \tag{6.56}$$

Q_m is the amplitude of the m-th harmonic. For abrupt interfaces only the odd Fourier components are nonzero, whereas for an arbitrary profile all components have to be considered. During growth or during an annealing procedure the coefficients Q_m vary with time according to the diffusion equation:

$$Q_m(t) = Q_m(0) \exp\left[- \left(\frac{2\pi m z}{D}\right)^2 D(T)\, t \right] \tag{6.57}$$

Depending on growth direction and crystal structure, the influence of the concentration profile $c(z)$ on the X-Ray scattering amplitudes $S(k)$ has to be calculated. In a kinematical approximation then the intensities of the SL peaks are readily calculated and the relation between the intensity of the satellite peak number ±m and the Fourier coefficients Q_m is given by

$$\frac{I_{\pm m}}{I_0} = \frac{Q_m^2}{4} \left(\frac{2\pi \epsilon \rho_{\pm}}{m\frac{2\pi}{D}} \pm \eta \right)^2 \tag{6.58}$$

where

$$\rho\pm = la^* \pm \frac{m2\pi}{D} \qquad h = \frac{4\Delta f}{S(00l)}$$

(for growth along the [001] direction). $S(00l)$ is the average structure factor of the $A_{1-x}B_xC$ lattice; ϵ denotes the amplitude of the interplane spacing modulation. $\Delta f = f_A - f_B$ takes into account the modulation of the scattering due to the difference in chemical composition and a^* is an average lattice parameter in reciprocal space.

Thus the intensity of the SL peaks in an X-Ray diffractogram has two contributions:

a) one originating from the modulation of scattering amplitudes due to the differences in chemical composition

b) the second originating from the modulation of interplanar spacing (see also Fig. 6.32).

Using intensities on both sides of the central peak (which yields I_0 as intensity) both Q_m and ϵ can be determined. From the knowledge of the Q_m's the concentration profile is established.

Quite often, especially for large x in $AC/A_{1-x}B_xC$ superlattices, the interdiffusion process is *composition dependent* and the Fick's law according to

$$\frac{\partial c}{\partial t} = D\frac{\partial^2 c}{\partial z^2} + \frac{\partial D}{\partial c}\left(\frac{\partial c}{\partial z}\right)^2 \tag{6.59}$$

has to be used. For the consequences, especially in short period superlattices, we refer to Fleming et al. [6.83], and Mc Whan [6.139, 6.140].

Several authors have investigated the limits of the applicability of the procedure just outlined. Recently, Hogg et al. [6.142] have shown that for large differences in lattice constants of the constituent materials, i.e. large values of strain, the diffusion constant derived from the satellite intensities using the method of Fleming et al. [6.83] breaks down. As a breakdown criterion Hogg et al. [6.142] have suggested:

$$\frac{\lambda}{2\cos\theta}\left(\frac{1}{d_w} + \frac{1}{d_b}\right) \geq \frac{a_w^{\perp} - a_b^{\perp}}{a_b^{\perp}} \tan\theta \tag{6.60}$$

i.e. when the strain is sufficiently large to cause a splitting of the well (w) and barrier (b) diffraction patterns, e.g. like that shown in Fig. 6.33 or schematically in Fig. 6.32.

However, there is another effect which has to be considered especially in SL structures where the interdiffusion coefficient is quite large. The layers close to the substrate are for a longer period of time at growth temperature than those close to the final surface. Consequently, already during growth the layers close to the substrate experience more interdiffusion than those which are close to the growing surface.

Thus the diffusion equation has to be solved with a boundary condition at the surface where the diffusion current equals the flux of component B (in a AC/$A_{1-x}B_xC$ SL grown by MBE) for a sticking coefficient of one [6.143]. The diffusion equation

$$\frac{\delta c}{\delta t} = \frac{\delta}{\delta z}\left(D\frac{\delta c}{\delta t}\right) \tag{6.61}$$

is solved in discretised steps in $i\Delta z$ ($i = 1, 2, \dots, N$) equal to the plane distances (monolayer by monolayer) and in $j\Delta t$ ($j = 1, 2, \dots, N$)

$$\frac{c(1, j+1) - c(i, j)}{\Delta t} = D\frac{c(i+1, j) - 2c(i, j) + c(i-1, j)}{(\Delta z)^2} \tag{6.62}$$

In the simulation Δz corresponds to the lattice plane distances (here d_{111}, but identical considerations hold for d_{100}) growth direction, the temporal step Δt is related to the growth rate v by $\Delta t = d/(vn_{\mathrm{tot}})$, where $n_{\mathrm{tot}} = d/d_{111}$. With these expressions, the equation above can be rewritten

$$c(1, j+1) = c(i, j) + D\frac{d}{vd_{111}}(c(i+1, j) - 2c(i, j) + c(i-1, j)) \tag{6.63}$$

A unique solution is only possible for special boundary conditions.

For the two-dimensional growth process two spatial boundary conditions must be considered: At the buffer-to-substrate interface the diffusion current vanishes, whereas at the top layer the diffusion current equals the incoming flux I_{beam} from the source, if a sticking coefficient of 1 is assumed. Thus the boundary conditions are

$$\frac{\delta c}{\delta z} = 0(z = 0) \tag{6.64}$$

$$c(1, j) = c(2, j) \tag{6.65}$$

$$\frac{\delta c}{\delta z} = I_{\mathrm{beam}}(z = vt) \tag{6.66}$$

$$c(j, j) = I_{\mathrm{beam}}(j)\Delta t \tag{6.67}$$

The Eqs. (6.66, 6.67) reflect the moving boundary $i = j = 1, 2, \dots, N$ during the growth.

This procedure was used for the analysis of rocking-curves of PbTe/ PbMnTe superlattices [6.143]. The X-Ray diffraction data were compared with calculated ones, based on the Mn-profile which was obtained from the numerical solution of the diffusion equation. For large interdiffusion it is difficult to obtain from the damping of the satellite intensities alone reliable information on the diffusion constant and the method just described should be used. Furthermore one has to consider the influence of interface roughness on the satellite intensities as well.

An interesting example for nonlinear interdiffusion in HgCdTe/CdTe multilayers was performed by Kim et al. [6.144] who demonstrated the importance of relaxation of systems like SL's which are far from thermodynamic equilibrium.

In summary, interdiffusion does not affect the periodicity but decreases the contrast between the layers, and thus results in reduced satellite peak intensities particularly for the higher order satellites.

6.6.4.2 Imperfect Superlattices: Period, Thickness, Composition Fluctuations.

Fewster [6.145] has outlined a procedure for determining variations in period D, in interface roughness, and in interface grading from SL diffraction patterns.

Period variations are changes $\varDelta D$ of D, i.e. of the sum of barrier and well width with depth of the sample, but averaged laterally over a coherently diffracting volume. Interface roughness originates from both lateral changes of well and barrier widths as well as vertical variations of these quantities. This interface roughness can be either random or correlated both laterally and vertically as was discussed by Savage et al. [6.146], Phang et al. [6.147], Holý et al. [6.148]. The separation of correlated and uncorrelated interface roughness phenomena is possible by measuring both the Bragg diffracted intensities as well as the diffuse scattered ones.

In addition, in real semiconductor superlattices consisting of binary and ternary materials (e.g. $GaAs/Ga_{1-x}Al_xAs$) grading will occur which causes variations of the composition x across the interface, both vertically as well as laterally.

Since in uninterrupted MBE growth processes the growth front usually extends over about three monolayers in vertical direction, imperfect completion of layers during growth is a standard phenomenon.

Fewster has shown [6.149] that the higher order satellites broaden progressively if there are variations in the periods. For satellite peaks close to the central Bragg peak, $\cos\theta$ is nearly constant, D may be simplified to:

$$D = \frac{(L_i - L_j)\lambda}{\varDelta\theta \, 2\cos(\theta)} \qquad (6.68)$$

where $\varDelta\theta$ is the angular distance between two satellites L_i, L_j. From the differentiation of this equation follows the relation between the change in period $\varDelta D$ and the satellite broadening $\delta(\varDelta\theta)$ (difference in angle within one satellite):

$$\delta(\Delta D) = \frac{(L_i - L_j)\lambda}{2\cos(\theta)} \frac{1}{(\Delta\theta)^2} \delta(\Delta\theta) \tag{6.69}$$

If grading occurs at heterointerfaces, both the lattice parameters and the scattering factors change, which have to be included in model calculations. In Fig. 6.33 the substrate and the buffer layer have different chemical compositions and thus different lattice constants. The superlattice itself has a mean lattice constant, which depends on the lattice constants of the constituents A, B and their layer widths d_A, d_B. From the angular separation between the $i = 0$ superlattice peak, the average mismatch can be roughly calculated [6.137]:

$$\left(\frac{\Delta a}{a}\right)_{\perp} = \frac{-\Delta\theta(1-\nu)}{\cos^2\phi(\tan\theta_B + \tan\phi)(1+\nu)} \tag{6.70}$$

where ν is the Poisson ratio, and ϕ the angle between the diffracting lattice planes and the surface plane. For small total thicknesses of the SL ($< 0.5\,\mu$m) the average $i = 0$ SL peak is shifted to the substrate peak and only a dynamical simulation program yields proper results.

For the description of imperfect superlattices which exhibit composition gradients computer simulations are presented in the following. As an example the (004) diffractogram of an ideal 10 period $In_{0.511}Ga_{0.489}As$ /InP MQW structure is shown in Fig. 6.45a. Figure 6.45b shows the effect of a linear

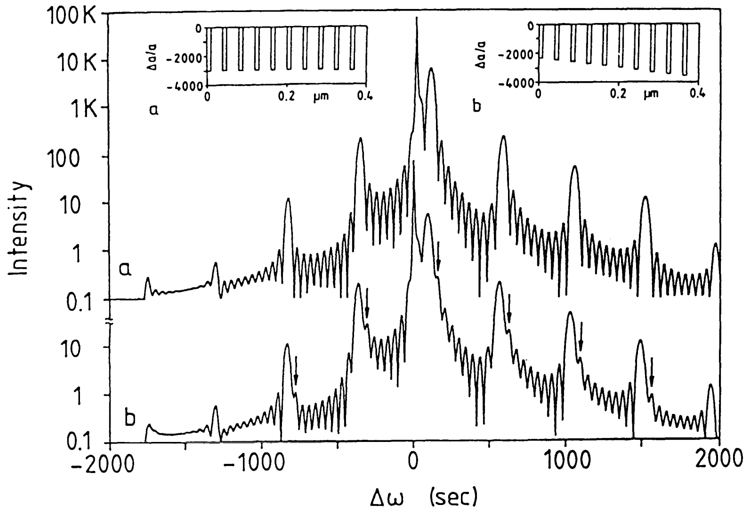

Fig. 6.45a. Calculated (004) Bragg diffractogram for a 10 period $In_{0.511}Ga_{0.489}As$/InP MQW structure on InP(001) with $d_1 = 10\,$nm and $d_2 = 30\,$nm, **b** Effect of a gradient in In concentration from 0.516 to 0.507 on the diffractogram. Arrows indicate the secondary maxima which would lead to broadening and/or splitting of the experimental diffractogram

gradient in the composition on the diffractogram. The In gradient from 0.516 to 0.507 causes only minute changes in the intensity of the main satellite peaks, whereas the envelope function of the secondary has changed which manifests itself as an enhancement of the $i = 1$ secondary maximum (see arrows). In a measurement such a gradient will appear as a splitting and/or broadening of the satellite peaks. For a statistical fluctuation of the In content within the limits $x = 0.516$ to 0.507, the resulting diffractogram is hardly distinguishable from that of the perfect one. Several authors have discussed and experimentally investigated such effects [6.150–6.155]. Also for the investigation of imperfect SL structures reciprocal space mapping offers some advantages. With DCD scans it is in general difficult to separate strain and composition gradients in SLS structures from each other. Using reciprocal space maps around symmetrical and asymmetrical Bragg reflections, such a distinction can be easily made both from the asymmetry of the iso-intensity contours and from the maximum intensity positions with respect to the substrate reciprocal lattice points.

6.6.5 Strained-Layer Superlattices: Tilt, Terracing and Mosaic Spread

In general the mean superlattice lattice constant is different from that of the substrate and also different from that of the intermediate buffer layer. In the reciprocal lattice each substrate point is accompanied by a buffer point and a set due to the strained-layer superlattice. The relative position of the points depends on the superlattice period D and the strains present parallel and perpendicular to growth direction.

Neumann et al. [6.121] have studied the effects of terracing in GaAs/GaAs$_{1-x}$Sb$_x$ SL's. In Fig. 6.46a, a schematic presentation of a terraced SL is given, where the angle α denotes the terrace angle, i.e. the angle between the direction of modulation and the normal of the constituent lattice planes. This means that the chemical modulation direction is not parallel to the lattice planes of the SL film. In addition, the SL can also be tilted with respect to the substrate as shown schematically in Fig. 6.46b. There it is assumed that the GaAsSb layers are strained to match the lattice constants of GaAs both along the terraces as well as at the interfacial steps (completely coherent interfaces).

In Fig. 6.46b, a second angle 2β is defined, where β represents the average tilt of the entire superlattice (epitaxial film) with respect to the substrate. The value of β can be estimated to be

$$\beta \approx \frac{\alpha(a_{x'} - a_0)}{a_0} \approx \alpha\left(1 + \frac{2C_{12}}{C_{11}}\right)\frac{\Delta a}{a_0} \tag{6.71}$$

where a_0 and $a_{x'}$ are the lattice parameters at the step and directly above the step in the previous layer, respectively. Δa is the difference in lattice

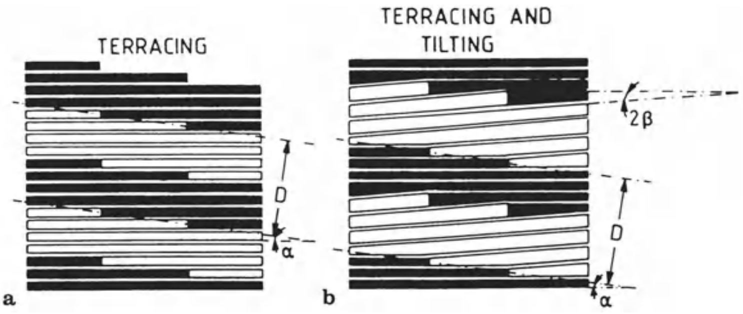

Fig. 6.46. Scheme of a terraced superlattice without (**a**) and with additional (**b**) tilting relative to the substrate [6.121]

constants between the ternary compound and the binary one. $a_{x'}$ is given by:

$$a_{x'} = a_x + \frac{2C_{12}(x)}{C_{11}(x)} \Delta a \tag{6.72}$$

Thereby the value of $a_{x'}$ was calculated by the Poisson expansion for a cubic cell compressed along two of the cube edges. With the assumption $C_{11} \approx 2C_{12}$ which is approximately valid for many zinc-blende semiconductors it follows for the tilt angle of a completely coherent system:

$$\beta \approx 2\alpha\epsilon \tag{6.73}$$

where $\epsilon = \Delta a / a_0$ is the misfit strain. This model describes the tilting mechanism in the regime of small strains i.e. without formation of misfit dislocations in the stack of the SL layer. Neumann et al. have found that for a GaAs substrate, miscut by 2°, and 25 periods of a $GaAs_{1-x}Sb_x$/GaAs SL with equal thickness and $D = 428$ Å the terracing angle α is 1.5° and the tilt angle β is 0.08°. These experiments were performed with a triple-axis spectrometer which is a convenient tool to separate the effects resulting from the terraced SL from the additional tilt.

Following a presentation given by Holý et al. [6.148,6.156,6.157] we summarise the effects of strains and terracing, and mosaic spread in a schematic presentation in Fig. 6.47 for a strained-layer SL grown along a [001]-direction. In Fig. 6.47 for clarity only the reciprocal lattice points (004), (224), and $(\overline{22}4)$ for the SL are presented. The azimuth is along a $[1\overline{1}0]$ direction.

The position of the strained layer SL peak labeled 0, i.e. the zeroth-order satellite peak depends on the mean strains parallel or perpendicular to the growth plane. The separation of the subsequent satellites numbered $(-i, -i+1, \ldots, -1, 0, +1, \ldots, i-1, i)$ is determined by $2\pi/D$, D being the superlattice period in the growth direction (in the case of Fig. 6.47 the [001]-direction). In a system without any tilt these satellites are arranged exactly in the [001]-direction, the picture for the asymmetric (224) and $(\overline{22}4)$ reflexes being completely symmetric with respect to the (004) reflexes. If terracing occurs, the superlattice peaks are rotated about the zeroth-order satellite by the terracing angle α and the zeroth-order satellite itself is rotated about (000) by the angle β as discussed above. We show schematically the effect of mosaicity, of the fluctuation of the SL period and of interface roughness as well as of random deformation on the shape of the reciprocal lattice points. The effect of mosaicity leads to a symmetrical smearing of the reciprocal lattice points according to Fig. 6.47 and causes an additional broadening due to the mosaic block shape function along the $\omega - 2\theta$ direction and the tilts between the mosaic blocks cause a broadening in ω-direction. The asymmetric RELP's are all elongated along the ω-circumference, the further away from (000) the larger the broadening. Interface roughness leaves the contours of constant intensity untilted. The SL0 peak is unaffected whereas with increasing satellite index the broadening perpendicular to the growth direction becomes larger.

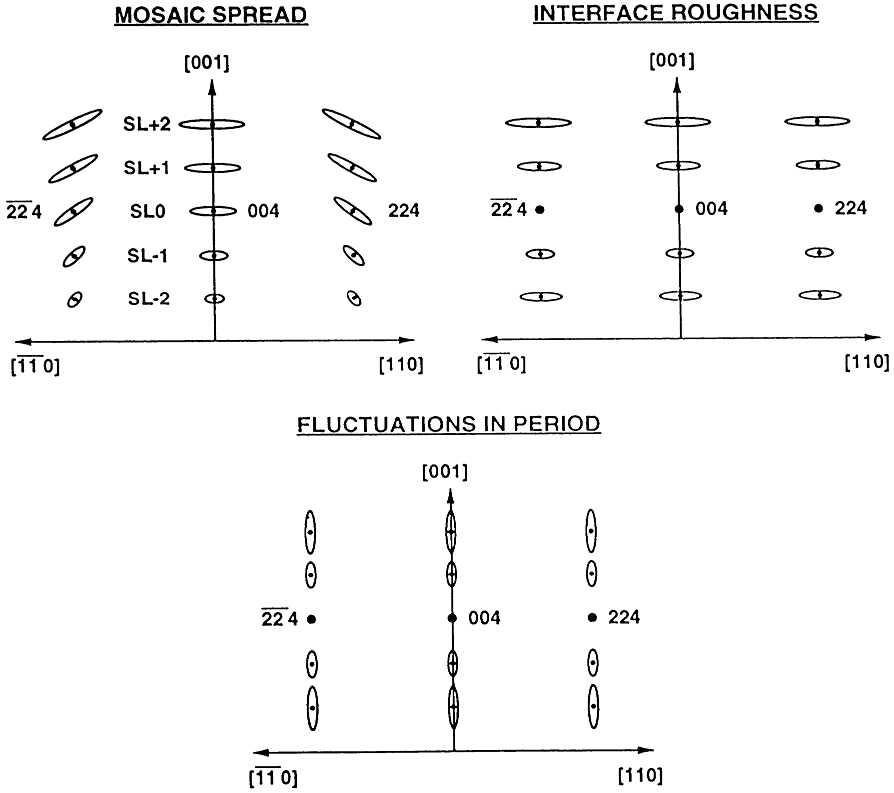

Fig. 6.47. Scheme of unstrained-layer SL of different orders on substrate without tilt in reciprocal space. Influence of mosaic spread, of interface roughness, and of fluctuations in period are shown schematically part) [6.148,6.156], see also Fig. 6.46

Fluctuations in the superlattice period manifest themselves in an elongation of the SL satellite peaks along growth direction, and again the SL0 satellite remains unaffected (Fig. 6.47).

6.7 Scans in the Reciprocal Lattice

So far only scans along one distinct direction in reciprocal space have been discussed. With the triple-axis spectrometers, nowadays available, maps of a reciprocal lattice spot are measured in order to determine independently Bragg plane tilts from asymmetry effects and substrate curvature induced broadening from film mosaicity (see Sect. 6.1.4).

This technique was applied to study intensity contour plots, along a (440) Bragg diffraction from a single QW InGaAs (160 Å) embedded in an InP barrier (500 Å cap layer, 2500 Å InP buffer deposited by MBE on InP:Fe substrate tilted 2° off) [6.42]. In Fig. 6.48 the intensity contours show $i = +4 \ldots -3$ satellites accompanying the strain-split InP peak in the center of the (440) diffraction. The crystal face is oriented in the [100] direction, the [010] direction lies within the surface plane. The intensity distribution (corresponding to 4 orders of magnitude) is recorded over a distance within the reciprocal lattice which corresponds to an ω-scan of 2.26°. Due to tilt of the growth plane by 2° off the [100] direction towards the [110] direction the line connecting the satellite intensity extrema is inclined by a small angle with respect to the vertical axis. For the intensity profile along the [100] and [110] direction it turns out that the position of higher order satellites yields quite precise information on lattice mismatch between the cap layer and the InGaAs quantum well, as well as on surface roughness and on interface roughness.

Another example of the efficient use of contour plots is shown in Fig. 6.49 which was obtained from a DCD together with a position-sensitive detector (PSD) system [6.12] for an $In_{0.2}Ga_{0.8}As$/GaAs strained-layer SL for the (224) reflection.

The intensity contour map yields much more information than the ω-scan which just resolves the substrate peak and the main SL peak but no satellites. The other projection in the $\Delta 2\theta$ axis which corresponds to an $\omega - 2\Theta$ scan reveals the satellite structure, but information of the tilt of the SL with respect to the substrate is lost.

A direct comparison of the information content of a rocking-curve of a ZnSe epitaxial layer on top of a GaAs substrate with a mapping of the reciprocal lattice is given in Fig. 6.50.

The main advantage of the triple-axis mode is the fact that the intensity contour plot gives much more information. The asymmetric broadening of the layer peaks is interpreted as being caused by mosaicity of the ZnSe layer in comparison to the much better perfection of the GaAs substrate. In the follow-

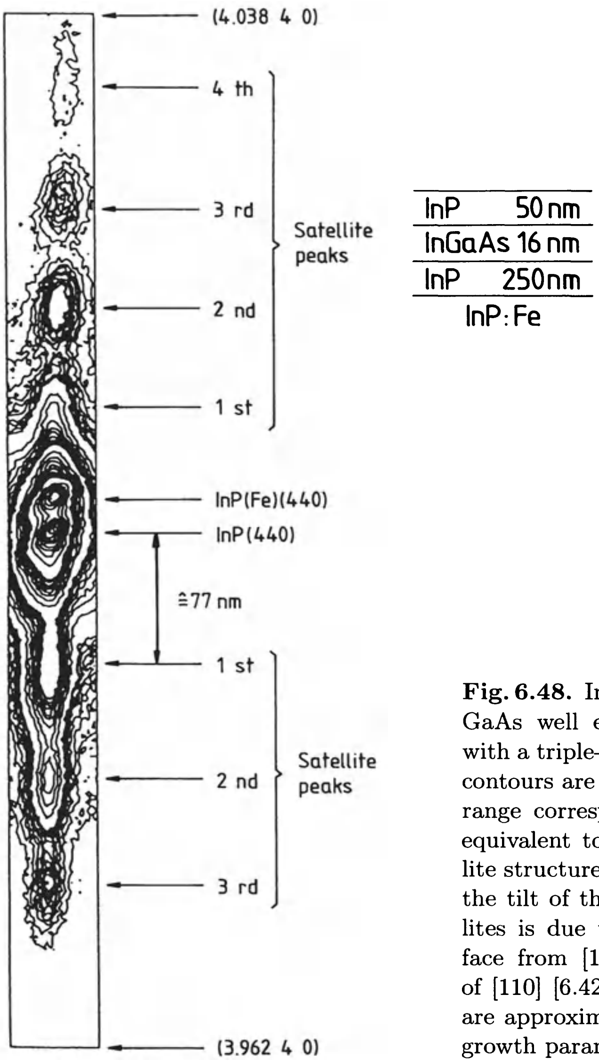

Fig. 6.48. Intensity contour plot of InGaAs well embedded in InP obtained with a triple-axis spectrometer. Intensity contours are shown over 4 decades. Scan range corresponds to ±0.07a^* which is equivalent to an ω-scan of 2.26°. Satellite structure is due to a period of 770 Å, the tilt of the line connecting the satellites is due to the offset of the crystal face from [110] by 2° in the direction of [110] [6.42]. Thicknesses in the insert are approximate values from the crystal growth parameters

ing Fig. 6.51a a direct comparison of a rocking-curve on a PbTe/EuTe SL and a reciprocal space mapping is presented. The SL consists of 40 double-layers of 93 ML of PbTe ($a_0 = 6.462$ Å) and 5 ML of EuTe ($a_0 = 6.598$ Å) which are deposited on a 4.1 μm PbTe buffer on a (111)-oriented BaF$_2$-substrate ($a_0 = 6.200$ Å). In the symmetric (222) Bragg reflection, superimposed on a broad background, $i = -18$ satellites are observed. The width of the SL maxima increases from 127" for $i = 0$ to 212" for $i = -15$.

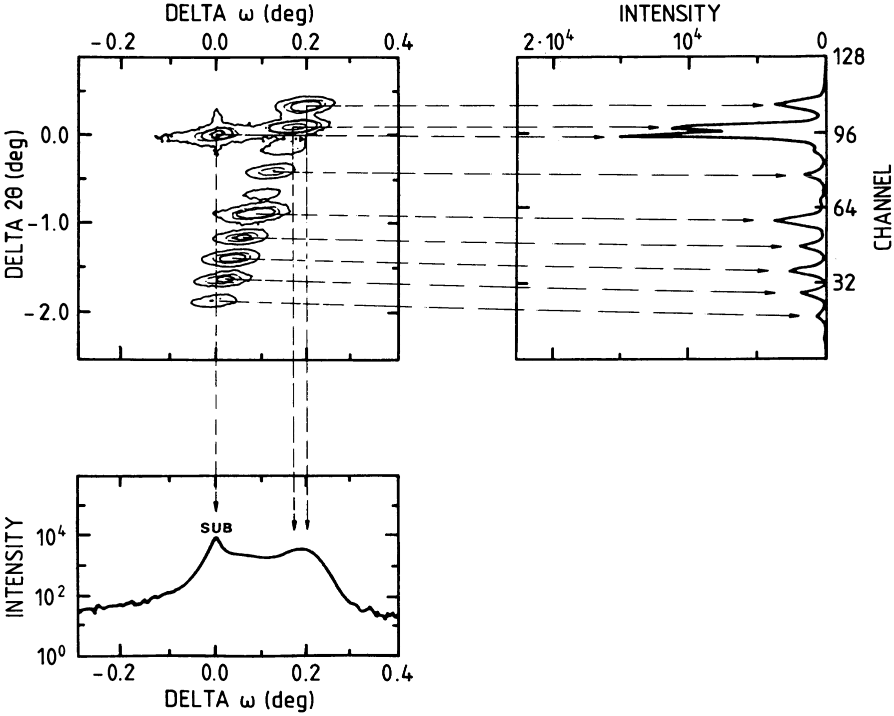

Fig. 6.49. Reciprocal space intensity contours of a GaAs/$In_{0.2}Ga_{0.8}As$ SL (d_1 = 12 nm, d_2 = 26 nm) deposited on an $In_{0.1}Ga_{0.9}As$ buffer (d = 200 nm) on GaAs ((224) reflection). Upper left corner: contours obtained with conventional DCD using a position sensitive detector; upper right: integrated intensity along 2θ and lower left: integrated intensity along ω with identification along lines with arrows [6.12]

According to Fewster [6.9, 6.10] the use of a triple-axis diffractometer, with an analyser which uses more than one reflection, offers the following advantages in the analysis of multilayer structures:

- Strain and strain gradients can be separated from structural imperfections such as tilts and mosaicity: in the reciprocal space maps the intensity distribution along the strain influences the $q_\perp$ -direction, i. e. the one along the ω-2Θ-scan.
- Mosaic spread or bending is observed along the $q_{\|}$- direction in the reciprocal space maps, i. e. along the ω- scan.

In superlattices, the half width of the zero order ($i = 0$) peak along the $q_{\|}$-direction yields the lateral correlation length ξ. Any additional broadening of the $i = \pm 1$ and higher satellite peaks along the $q_{\|}$-direction is associated

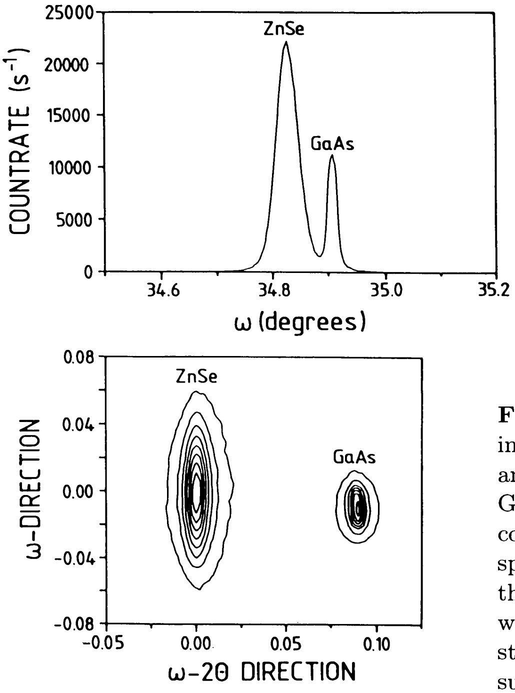

Fig. 6.50. Comparison of a rocking-curve of the (004) Bragg peak of an epitaxial ZnSe layer on top of a GaAs substrate with a iso-intensity contour plot obtained with the 4+1+2 spectrometer. From the $\omega - 2\Theta$ scan the lattice mismatch can be deduced, whereas during the ω-scan the broad structure of the ZnSe diffraction results from mosaicity [6.13]

with superlattice imperfections. Using the Scherrer equation

$$\xi = \frac{k\lambda}{2W\cos\theta} \tag{6.74}$$

where k is a constant (~ 1) which is characteristic for the shape, Θ the Bragg angle and W the width of the diffraction peak, the broader $i > 0$ SL peaks can be analysed to yield a correlation length ξ which characterises a length scale in the interfaces of the SL's. Such an analysis, performed by Fewster [6.9] on short period GaAs/AlAs (16.7 Å/16.7 Å) superlattices gave a correlation length ξ of the order of 400 to 800 Å, in good agreement with results of scanning tunneling microscopy. Hence, triple-crystal diffractometry is particularly useful for the investigation of imperfect superlattices and heterostructures. In strained-layer superlattices, beyond their critical thickness, partial strain relaxation occurs. Using reciprocal space mapping of asymmetric reflections, the complete strain status can be obtained: i.e. the strain components parallel and perpendicular to the surface, and therefore the lattice parameters. Furthermore, also information on the strain variation as a function of depth into the crystal is accessible. In addition, also information on mosaicity and tilting is obtained. Multicrystal-multireflection diffractometry can therefore determine residual strains and mosaic structure or bending in real heterostructure

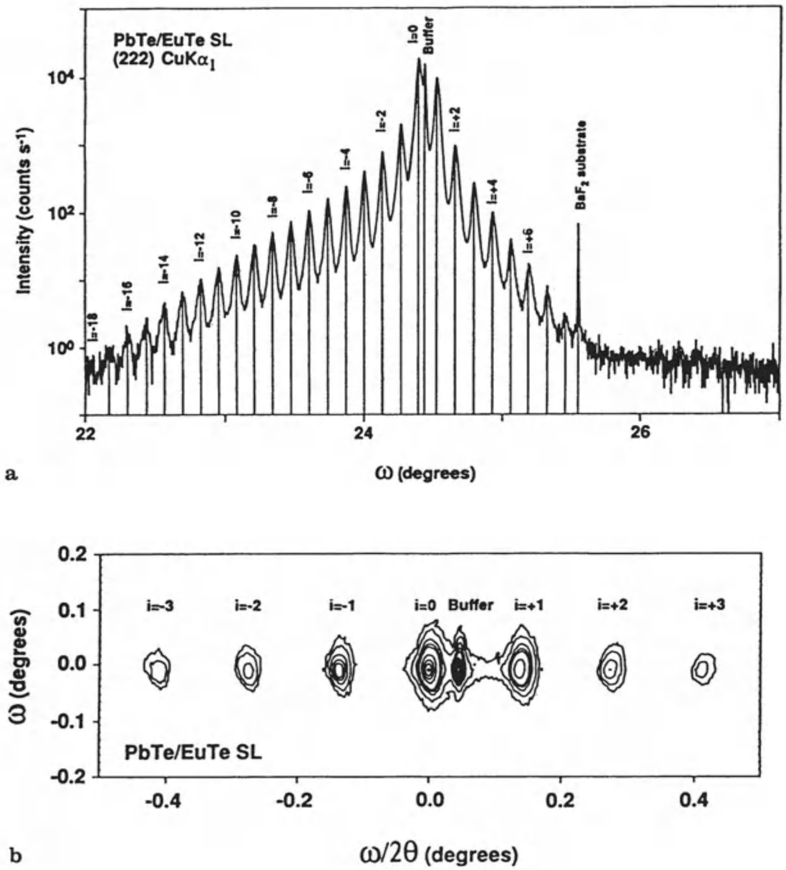

Fig. 6.51a. Rocking-curve of a PbTe/EuTe superlattice, one period consisting of 93 monolayers of PbTe and 5 monolayers of EuTe, 40 periods on a 4.1 μm thick PbTe buffer deposited on (111) BaF_2 substrate, **b** triple-axis reciprocal lattice scan intensity isocontour plot of the same structure showing broadening in the ω-direction which corresponds to the $q_{\|}$-direction. Intensities span the region from 5 to 5000 in 10 steps

systems. Such information is not accessible from conventional rocking-curves obtained with the DCD.

As an example we show in Fig. 6.51b the reciprocal map for a (222) diffraction of the same PbTe/EuTe SL structure which was shown in Fig. 6.51a. Along the ω-2Θ-direction ($q_{\perp}$-direction) the strain variations and thickness fluctuations of the SL along the growth direction can be derived. In the ω-direction ($q_{\|}$-direction) it is apparent that already the PbTe buffer layer peak exhibits some mosaic spread which increases considerably for the higher SL satellites. For the SL width along $q_{\|}$, we deduce an interface coherence length of about 700 Å. In order to extract the relevant information from the triple axis diffractograms it is necessary to calculate iso-intensity contour plots around reciprocal lattice points and to perform the necessary projections. For such imperfect structures the usual fitting procedure based on the Takagi-Taupin equations which label for dynamical scattering in nearly perfect layer structures is not adequate. Fewster [6.158] has recently attempted to formulate a dynamical diffraction theory for partially relaxed semiconductor layer structures which contain interfacial defects and has compared his calculation which experimental data on InGaAs/GaAs and on $Si/Si_{1-x}Ge_x$.

The combination of low temperature equipment and a triple-axis X-Ray spectrometer is particularly useful for the study of structural phase transitions. $Pb_{1-x}Ge_xTe$ exhibits a structural instability towards the formation of a rhombohedral phase at low temperatures from the high temperature rock-salt structure. Fig. 6.52 (top) shows the consequences of this phase transition for scattered X-Ray intensities in a reciprocal lattice scan. Below T_c, any of the equivalent ⟨111⟩-directions transforms into a rhombohedral *c*-axis. The occurrence of this splitting can be used as a manifestation for the phase transition. For a compound with a Ge content of 6% (film thickness: 2600 nm) a lattice temperature of 20 K is well below T_c. If a PbGeTe layer of the same Ge-content with a thickness of 500 Å is sandwiched between PbTe layers, the occurrence of the structural phase transition is inhibited, apparently by strains exerted on the PbGeTe film (Fig. 6.52 (bottom)). The films are deposited on (111) oriented BaF_2 substrates. The corresponding reciprocal lattice scan, showing iso-intensity contours around a PbGeTe reflection and around a PbTe reflection does not exhibit any evidence for a splitting of the PbGeTe peak even at $T = 20$ K [6.159]. For the Bragg diffractions, a pseudo-orthorhombic notation is used with the cubic [111] orientation parallel to the [001] orthorhombic direction and the orthorhombic [100] and [010] axes parallel to the [211] and [011] axes, respectively.

Another example for a reciprocal space map on a 2 μm AlInAs layer on an InP substrate is shown in Fig. 6.53 for a (004) reflection as obtained with the HRMCMRD (see Fig. 6.9) [6.58, 6.9, 6.10]. The diffraction space probe has a width of 10 arcsec and is presented by the parallelogram A'–B'. The parallel lines A–B denote the finite width of the Ewald sphere due to the wavelength spread leaving the monochromator. Without analyser crystals the detector acceptance angle is several degrees and corresponds to a sector which is longer than A–B. Measurements taken without an analyser (DCS, Bartels-type) and with the 3-diffraction analyser are compared in the right part of Fig. 6.53. From the DCS results using a wide open detector the intensities of layer and substrate are nearly identical. An $\omega - 2\Theta$ scan parallel C–D, however, reveals quite different intensities: smaller and broader for the layer and a larger peak intensity for the substrate.

From a series of scans parallel to the line C–D the diffraction map can be obtained and a detailed analysis of the two-dimensional intensity distribution

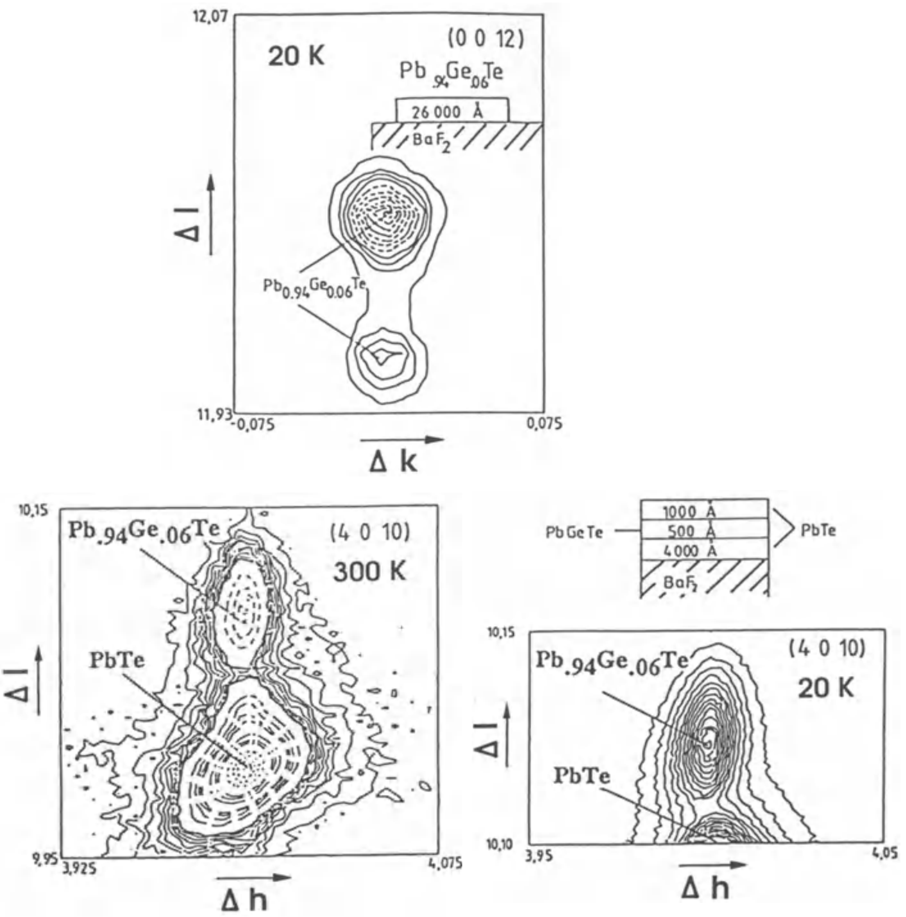

Fig. 6.52. Isocontour plots of PbGeTe layers deposited on a BaF_2 substrate with and without PbTe buffer and cap layers. top: at $T = 20\,K$, below the cubic - rhombohedral phase transitions, splitting of (0012) peak occurs (rhombohedral notation). bottom: with PbTe layers the phase transition is inhibited, probably due to mismatch strains [6.159]

yields information on strain, sample curvature, and eventually on mosaic structure. The excellent signal to noise ratio makes this technique most useful for the study of thin epitaxial layers and superlattices. Diffraction space maps in the vicinity of an asymmetric reflection of a superlattice can be used to determine partial relaxation in strained layer SL's, the strain variation as a function of the z-coordinate (growth direction) as well as any tilting. In combination with topography, where the film is placed behind the analyser crystal, a correlation of diffraction space mapping and topographs which ex-

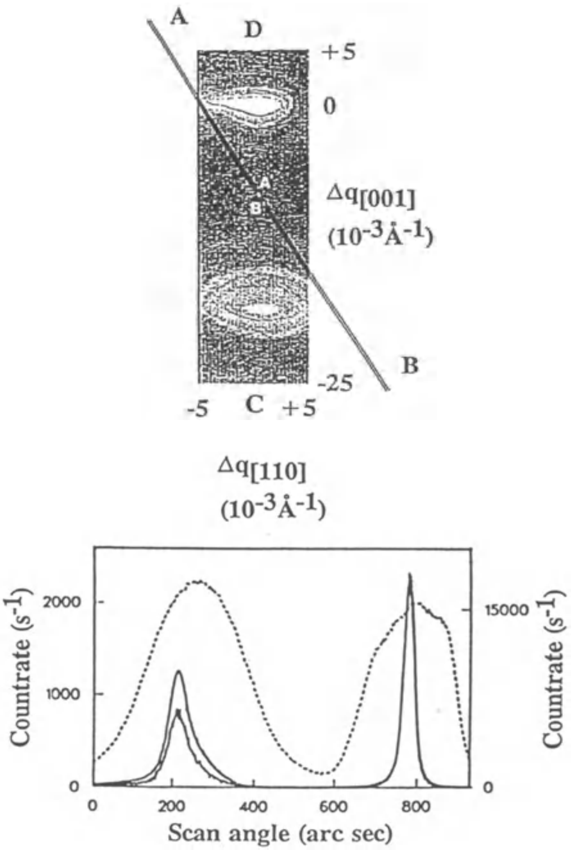

Fig. 6.53. Left panel: reciprocal space map of a (004) reflection from an AlInAs layer (2 μm) deposited on an InP substrate. The parallel lines A, B represent the finite width of Ewald sphere due to finite wavelength spread leaving the monochromator crystals. Direction C–D corresponds to a radial direction from (000) along d^*, accessible with an $\omega - 2\omega'$ scan. The 4 + 1 crystal monochromator with open detector accepts all intensities between lines A–B. In the HRMCMRD the probe which is swept is indicated by the small parallelogram A–B. Right panel: for the case shown above, different diffraction profiles: dashed lines correspond to ω-scan with 4 + 1 crystal monochromator the solid line is obtained with the HRMCMRD ($\omega - 2\Theta$ scan)(lhs intensity scale); dotted line: sum of the HRMCMRD scans parallel to C–D [6.9]

hibit intensity modulation due to strain fields of dislocations is possible (see Fig. 6.9). This combination technique has been applied by Keir et al. [6.160] for a study of the structural properties of $Hg_{1-x}Cd_xTe$/CdTe on GaAs.

In the following we demonstrate the usefulness of reciprocal space mapping for the assessment of the structural properties of two short period

$Si_{0.6}Ge_{0.4}$ structures grown on either single step or step-graded SiGe buffers. Reciprocal space mapping of both symmetric (004) and asymmetric (224) Bragg diffraction peaks is used to establish the status of strain relaxation. The structural characteristics of substrate, buffer, and superlattice influence the positions of the reciprocal lattice points (RELP) and the shape of iso-intensity contours around them. We show that these two- dimensional reciprocal lattice maps yield a wealth of structural information, usually much more than the conventional rocking-curves [6.161]. Both SL samples were grown by molecular beam epitaxy on (001) oriented non-miscut Si substrates. For sample A, a 20 nm thick Si layer was deposited at $T = 550\,°\mathrm{C}$, followed by the 20 nm thick single step $Si_{0.60}Ge_{0.4}$ buffer deposited at 450 °C. The short period SL $Si_{0.60}Ge_{0.4}$ was grown at 350 °C (145 periods). For sample B, a 100 nm thick Si layer was grown on top of the substrate followed by the step-graded buffer (B1), in which the Ge content was increased stepwise by 3% per 50 nm up to a total thickness of 700 nm., i.e. to a nominal Ge content of 40%. During the buffer growth, the temperature was decreased continuously from 600 °C to 520 °C. Subsequently, a 550 nm thick $Si_{0.60}Ge_{0.4}$ alloy buffer layer (B2) was grown at 500 °C. Prior to the growth of the SL a monolayer of antimony was deposited as a surfactant. For the thick step-graded buffer, the relaxation mechanism causes a complete relaxation of the individual slices, of which the buffer is composed, and thus the corresponding RELP's finally lie along the [224] direction which connects (000) with the (224) substrate RELP. In such a case the superlattice with the proper mean composition (with respect to the top buffer layer) can grow virtually unaffected by the substrate. The in-plane lattice constants of the SL and the top buffer layer coincide and within the SL layers the values of biaxial compression and dilation are unaffected by the substrate.

In Fig. 6.54 contours of constant scattered intensity around the (004) and (224) RELP's of sample A are shown, which were derived from a series of $\omega - 2\Theta$ scans with ω-offsets using the proper transformation from angular space into reciprocal space [6.161]. The asymmetry around the substrate (004) RELP is an artifact (analyser streak caused by the finite size of the reciprocal space probe, which is defined by the X-Ray optics used). Qualitatively, the strain situation is determined by a partially relaxed buffer layer, on which pseudomorphic growth of the superlattice with respect to the single step buffer occurs as indicated by the position of the zero order superlattice peak. For sample B, the reciprocal space maps are shown in Fig. 6.55. From both RELP's around (004) and (224) it follows that all portions of the step-graded buffer (B1) are fully relaxed, because the intensity contours are symmetric around the $\mathbf{q}_{||}[224]$ direction, which is not entirely the case for the zero order intensity contours. The maximum intensity lies along the $[11\bar{1}]$ direction away from the $\mathbf{q}_{||}[224]$ direction. The region of the SiGe alloy with constant Ge content (B2) yields intensity contours which overlap in their positions with the zero order contours of the superlattice. Because of its low intensity, the

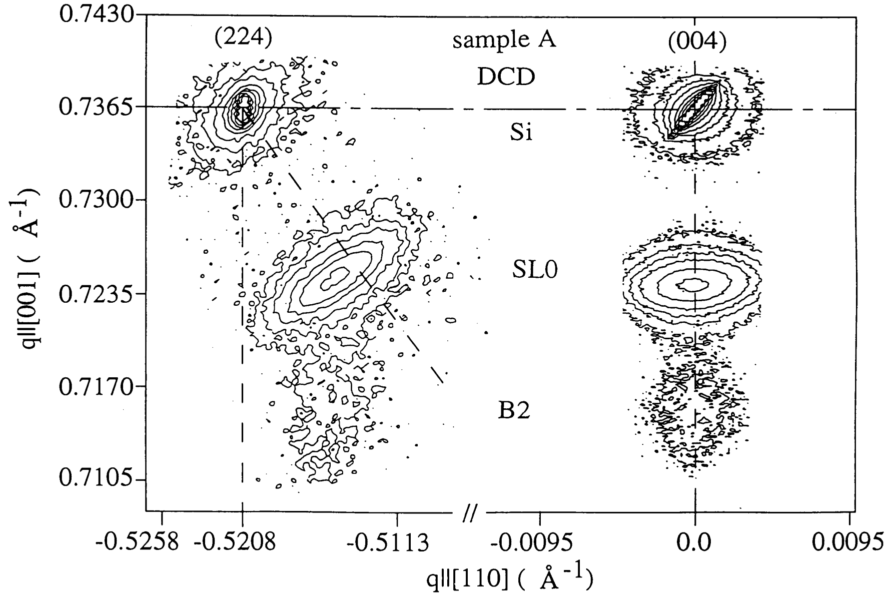

Fig. 6.54. Measured (224) and (004) reciprocal space maps of sample A. The iso-intensity contours correspond to 0.5, 1, 2, 10, 20, 2000 cps in the (224) map and to 1, 2, 10, 20, 100, 2000 cps in the (004) map. The (224) buffer RELP lies below the center of the SL0 RELP along the [001] growth direction [6.161]

zero order peak was not detected in the (224) map. From the (004) reciprocal space map it follows that the tilt between superlattice, buffer and substrate is negligible.

From the reciprocal space maps, *FWHM*'s of the intensity distribution parallel [001] and perpendicular [110] to the growth direction are deduced and for sample A values of 400 and 1150 arcsec are found, respectively, for the zero order peak of the superlattice. For sample B, the corresponding values are 350 and 1070 arcsec, respectively, which do not change for first order (SL-1) intensity contour within the experimental accuracy of ±15 arcsec.

From Figs. 6.54 and 6.55 it is obvious what potential is offered for immediate identification of the strain status of short-period superlattices by reciprocal space maps. The symmetry of the intensity contours around the zero order peaks indicates the absence of large scale strain gradients along the growth direction, and a rather statistical distribution of the mosaic blocks and a constant strain status within the superlattice stack.

If partial relaxation occurs on SLS grown on alloy buffers, the evaluation of the strain status is complicated when a deviation from Vegard's law is present, which is the case e.g. for SiGe alloys. This deviation has to be

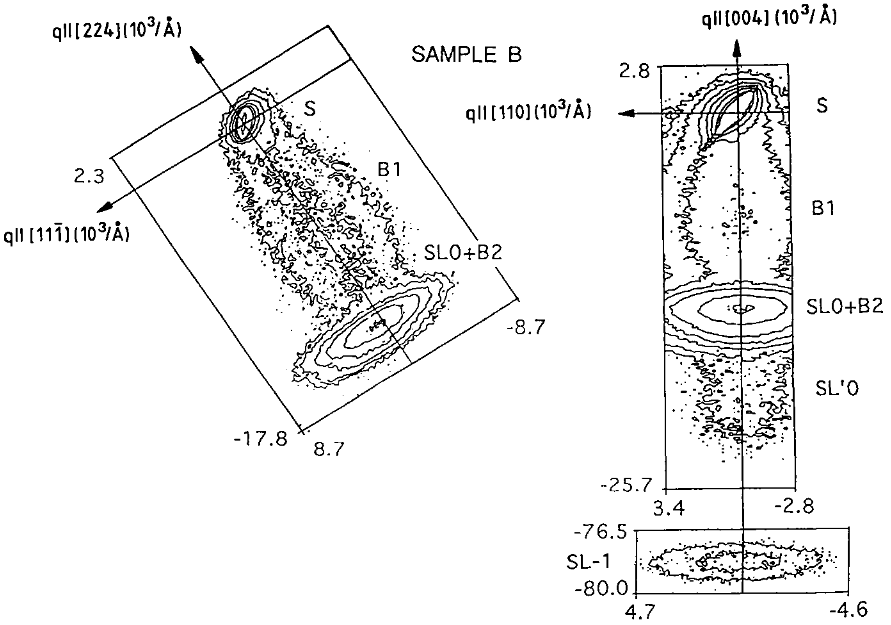

Fig. 6.55. Measured reciprocal space maps of sample *B*. The iso-intensity contours correspond to 1, 2, 5, 10, 20, 50, 1000 cps in the (224) map, to 1, 2 cps in the (004) map of the SL-1 and to 1, 2, 5, 10, 20, 50, 100 cps in the other (004) map, respectively. In the (224) map, the B1 buffer layers RELP's are symmetric around the [224] direction indicating full relaxation; the shift of the maximum intensity of the SL0 peak away from the $q \parallel [224]$ direction indicates residual in-plane strain SL of −0.33% [6.161]

considered for the evaluation of strain status deduced from the shift of the reciprocal lattice points during the relaxation process.

The distribution of the diffusely scattered intensity around reciprocal lattice points results from structural imperfections like microscopic and macroscopic strain gradients, and statistically distributed lattice plane tilts, usually referred to as mosaicity.

Recently, the correlation function of the random deformation field due to these structural defects was calculated for short period Si_9Ge_6 superlattices. The Fourier transformation of the two-dimensional reciprocal space distribution of the scattered intensity equals the correlation function multiplied by the reflectivity of the perfect structure, i.e. it is obtained from the reciprocal space maps without any assumption on the defect structure in the sample. From the correlation function one obtains directly the region which scatters X-rays coherently, i.e. along growth direction as well as laterally [6.163]. Reciprocal space mapping has been also used quite extensively to study partially relaxed layers of ZnSe grown by MBE on (001) oriented GaAs substrates [6.164]. From measurements of reciprocal space maps around different asymmetric and symmetric RELP's a depth gradient not only in strain but also in mosaicity was derived by the authors.

In the following we show data on pseudomorphic Si/SiGe MQW structures which exhibit considerably smaller *FWHM*'s both along and perpendicular to growth direction. The p-type modulation doped Si/$Si_{1-x}Ge_x$ MQW structures were grown by MBE on (001) oriented Si substrates [6.165]. The MQW sample, on which X-Ray data are shown in Fig. 6.56, consisted of 10 repeats of 52 Å thick $Si_{0.77}Ge_{0.23}$ wells and 175 Å thick Si barriers. A Si cap layer of 440 Å was deposited on top.

In Fig. 6.56 in the insert a DCD rocking-curve of the (004) Bragg reflection is shown. Apart from the substrate peak several superlattice peaks are identified. However this sample shows subsidiary intensity maxima between the main SL maxima. Since the number of periods is $N = 10$, the number of

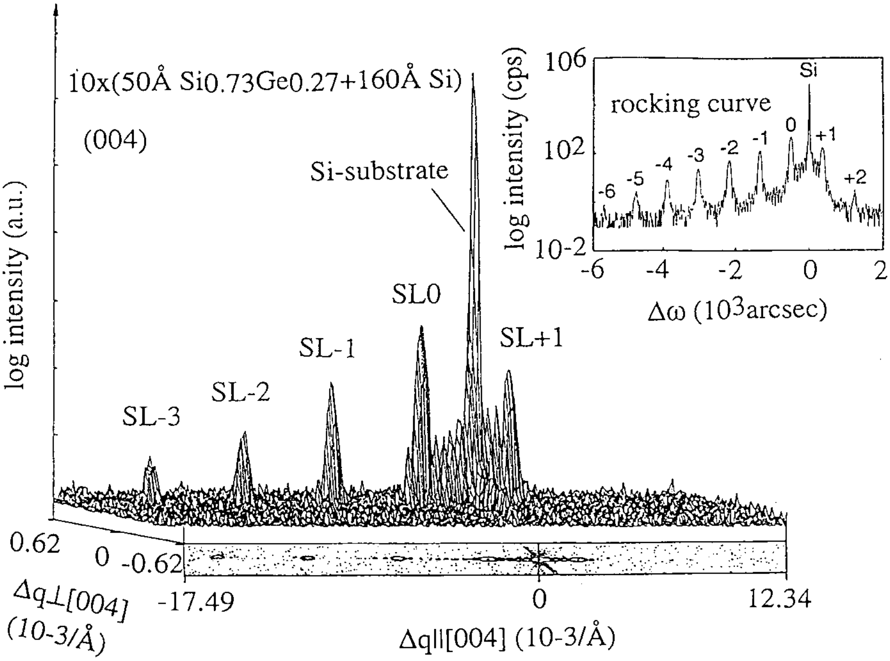

Fig. 6.56. Triple-axis reciprocal space map of a pseudomorphic Si/SiGe MQW structure on Si(001) in the vicinity of (004) substrate reflection along the directions q||[004] and perpendicular to it. Three- and two-dimensional contour plots of constant scattered intensity (in a logarithmic scale) are shown, transformed to reciprocal space coordinates Δq relative to the substrate. The insert exhibits a DCD rocking-curve measured over the same region in reciprocal space with the Si substrate peak and several orders of superlattice peaks $(-6 \ldots 2)$ [6.165]

subsidiary maxima has to be $N - 2$, which is in this case $10 - 2 = 8$. The subsidiary maxima can be identified not only between SL0 and SL+1, but also between the SL0 and SL-1, SL-1 and SL-2 and even in between SL-2 and SL-3. In Fig. 6.56 also a reciprocal space map around the (004) Bragg reflection for the substrate and the SL+1, SL0, SL-1,-2,-3 peaks is shown, which demonstrates the different *FWHM*'s of the contours of equal intensity along the [004]-direction and perpendicular to it (i.e., the [010]-direction). The intensity in the reciprocal space map is also shown in a three-dimensional representation. In Fig. 6.57 the central part of 6.56 is enlarged for clarity for the demonstration of the subsidiary intensity maxima in between the SL0 and SL+1 superlattice (004) reflections for the same sample. The *FWHM* of the SL extrema along growth direction is 78 arcsec, which is due to the finite thickness of the entire MWQ stack. However, perpendicular to growth direction the *FWHM* is only 13 arcsec for the zero order peak, which indicates the extremely high crystalline perfection and the absence of any appreciable mosaicity. This fact is not astonishing since the analysis of the (004) and the (224) reciprocal space maps yield that the mean in-plane lattice constant

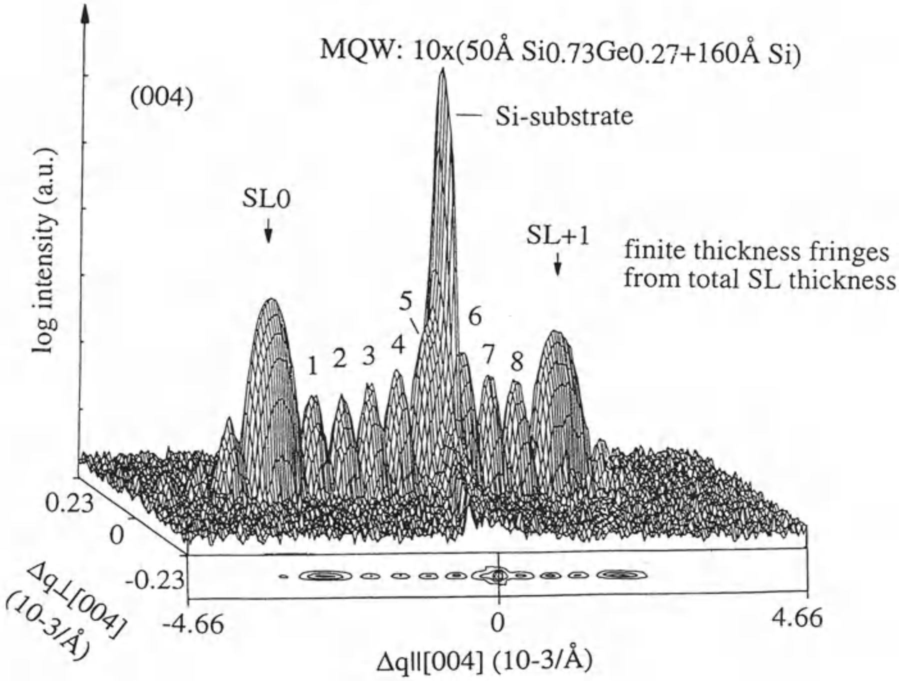

Fig. 6.57. Detail of Fig. 6.56 showing 8 clearly resolved finite thickness fringes inbetween the SL peaks SL0 and SL+1, indicating high structural perfection. The *FWHM* of the SL reciprocal lattice points in the $\mathbf{q}_\perp$ direction are remarkably small [6.165]

of the MQW constituent layers is exactly equal to the unstrained Si lattice constant.

For superlattices grown along a [111]-direction like e.g. the one shown in Fig. 6.58 usually reciprocal space maps are recorded around a symmetric (222) and an asymmetric (264) reflection. The data stem from a PbTe (87.6 monolayers)/EuTe (5 monolayer) superlattice grown on a PbTe buffer, deposited on a (111) BaF_2 substrate. The iso-intensity contours in the vicinity of the buffer (B) and the superlattice peaks (SL0, SL ± 1, SL ± 2, SL ± 3) are shown. For these two (111) and (264) reflections the superlattice peaks lie all along the [111]-direction normal to the sample surface and both measurements were performed in the same $[1\bar{1}0]$ azimuth orientation of the sample.

A theoretical analysis based on the kinematical diffraction theory of diffuse X-Ray scattering from multilayers exhibiting interface roughness as well as mosaic structure was given by Holý [6.168]. With this method iso-intensitiy

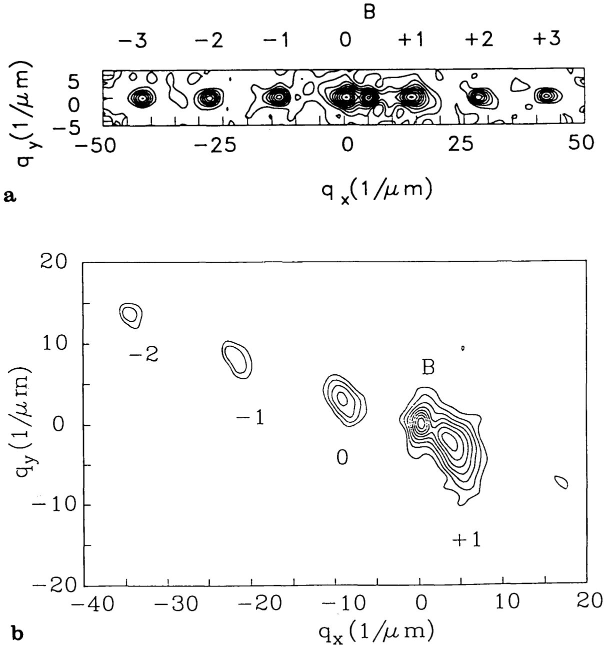

Fig. 6.58. Reciprocal space maps around symmetric (111) (**a**) and asymmetric (264) (**b**) reciprocal lattice points of a PbTe (87.6 monolayers)/ EuTe (5 monolayers) superlattice grown on a PbTe buffer deposited on (111) BaF_2 substrate. The ω and $\omega - 2\theta$ scan directions are transformed to the reciprocal space axes q_x (parallel to $q_{[222]}$) and q_y (perpendicular to $q_{[222]}$) for (**a**), and parallel to $q_{[264]}$ and perpendicular to $q_{[264]}$ for (**b**) [6.128]

contours and various satellite reflections in reciprocal space maps as well as DCD rocking-curves are simulated. The analysis yields interface roughness, the correlation of interface roughness from different interfaces, and independently the mosaic spread.

6.8 New Developments

6.8.1 Analysis of Quantum Wire Structures Using HRXRD

Laterally structured semiconductors (quantum wires and quantum dots) are in the focus of current interest. Since these are periodic structures with large coherence length and typical dimensions of the order of 1000 Å, X-Ray diffraction can be used to get information on their structural quality.

Recently Tapfer et al. [6.169, 6.170] have studied deep mesa etched AlGaAs/GaAs quantum wire structures and obtained both the quantum-wire period as well as the quantum wire width. In the angular range close to a Bragg diffraction peak interference of X-Ray waves scattered by the quantum-wires occurs. For the analysis a combination of X-Ray diffraction- and a multiple-slit Fraunhofer model has been employed. The normalised reflectivity as a function of the deviation $\varDelta\theta$ from the Bragg angle is given by

$$R(\varDelta\theta) = (|Y_h|DI)^2 \tag{6.75}$$

where Y_h is the Fourier coefficient of the polarisability for the h-th Bragg reflection and

$$D = \frac{\sin\beta}{\beta} \tag{6.76}$$

the diffraction term with

$$\beta = \frac{\pi d_w \sin(2\theta_B)\varDelta\theta}{\lambda\cos\theta_e} \tag{6.77}$$

where d_w is the quantum-wire width, θ_e is the angle between reflected X-Ray beam and the crystal surface. I is the interference term

$$I = \frac{\sin(N\alpha)}{N\sin\alpha} \tag{6.78}$$

with

$$\alpha = \frac{\pi L_p \sin(2\theta_B)\varDelta\theta}{\lambda\cos\theta_e} \tag{6.79}$$

where N is the total number of irradiated quantum wires and L_p the QW period. From these equations the QW width d_w and period L_p are given by

$$d_w = \frac{\pm m\lambda\cos\theta_e}{\Delta\theta_{\min}\sin(2\theta_B)} \tag{6.80}$$

$$L_p = \frac{\pm n\lambda\cos\theta_e}{\Delta\theta_{\max}\sin(2\theta_B)}. \tag{6.81}$$

There is the possibility that the maxima of I coincide with the minima of D. When $L_p = (n/m)d_w$ the n-th order QW peaks are suppressed. This allows determination of not only the QW period but also the QW width d_w. An example of such a measurement is given in Fig. 6.59 with inserts explaining the scattering geometry. In reciprocal space the rods have dimensions Å^{-1}, the inverse height of the mesa-etched structures and they are a distance $1/L_p$

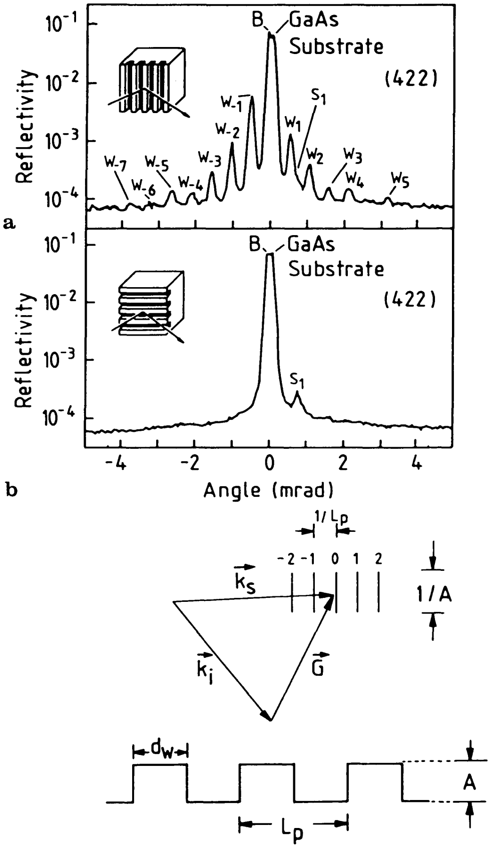

Fig. 6.59. Diffraction pattern of a GaAs/Al$_{0.36}$Ga$_{0.64}$AS multi quantum well wire structure (**a**) perpendicular and (**b**) parallel to the scattering plane as indicated by the inserts [6.171]. The satellite peaks W_i are due to the periodic array of the quantum wires. Lower part shows the corresponding scattering scheme in reciprocal space [6.166]

apart. The accuracy of the determination of the quantum wire period L_p is about 30 Å.

Figure 6.59 shows experimental X-Ray diffraction pattern of a MQW $Al_{0.36}Ga_{0.64}As/GaAs$ deposited on a $Al_{0.36}Ga_{0.64}As$ buffer layer on top of a GaAs substrate for an asymmetric (422) reflection. The satellites designed W_i (with i up to ±6) are due to the lateral periodicity caused by the quantum wires and their separation yields a period of 282 nm and a quantum wire width of 60 nm. B denotes the diffraction peak of the buffer and S_1 the first order SL peak from the chemical modulation along the growth direction. In addition, Tapfer et al. deduced from the comparison of the SL peak positions in the two scattering geometries an in-plane lattice strain normal to the quantum wires.

Macrander and Slusky [6.166] have investigated InP substrates with a sawtooth corrugation and overgrown epilayers of InGaAsP on these substrates. They found satellite structures, if the corrugations were oriented perpendicular to the diffraction plane. For the corrugation orientation parallel to the diffraction plane no evidence for satellite peaks was found.

Recently, a diffraction model based on a semi-dynamical diffraction theory for the calculation of diffraction pattern of corrugated surfaces was presented [6.172]. This model is useful for the determination of the shape (rectangular, trapezoid, ...) i.e. of the geometrical parameters of the surface corrugation from the observed diffractograms. The analysis of symmetric and asymmetric diffractograms is necessary for this purpose, the latter should be recorded in glancing exit reflection geometry, since this is the most sensitive one to surface corrugation. Apparently, two-dimensional reciprocal space maps offer similar advantages for the analysis of periodic corrugated surfaces as well as for periodic semiconductor wires or dots fabricated by deep mesa etching, as they do for the analysis of epilayers and heterostructures. Gailhanou et al. [6.173], van der Sluis et al. [6.174] and Holý et al. [6.175] have recently used this technique for the study of corrugated GaAs, InP, Si substrates as well as InAs/GaAs quantum wires. Gailhanou has pointed out that surface gratings act simultaneously as reflection and transmission gratings.

Fukui and Saito [6.176] have in principle made similar observations on fractional-layer superlattices $(AlAs)_{0.5}/(GaAs)_{0.5}$ grown on vicinal (001) surfaces which exhibited satellite peaks in X-Ray diffraction due to the lateral compositional modulation (AlAs rods–GaAs rods). Structural studies on InAs microclusters (quantum dots) were also performed by Brandt et al. [6.177]. The InAs microclusters were prepared by deposition of fractional monolayers of InAs on terraced (001) GaAs surfaces and subsequent overgrowth of InAs. An asymmetry of the angular position of the satellite peaks (±1) was observed when the sample was rotated around the surface normal.

In the following reciprocal space maps of the diffraction pattern of reactive ion etched 150 nm and 175 nm wide GaAs/AlAs periodic quantum wires and quantum dots, fabricated by electron beam lithography and $SiCl_4/O_2$

reactive ion etching, are presented [6.178]. The GaAs/AlAs wires and dots were realized by nanostructuring a 30 period AlAs-GaAs multiquantum well grown on a 15 nm thick GaAs buffer. The nominally 8 nm thick GaAs wells are separated by nominally 12 nm AlAs barriers resulting in a total thickness of 600 nm. The MQW was capped by a 20 nm GaAs layer. Beneath the GaAs buffer 25 periods of a 5 ML/5 ML short period AlAs-GaAs SL with a total thickness of approximately 75 nm was grown on the GaAs substrate with a 80 nm buffer. The lateral macroperiodicity of the wire and dot arrays gives rise to additional intensity maxima in the diffraction pattern along q_x-direction perpendicular to the growth direction. In Fig. 6.60a reciprocal space maps around the (004) reciprocal lattice point (RELP) of an unstructured (as-grown) GaAs/AlAs-reference sample are shown. "S" denotes the GaAs-substrate peak, SL_0 and SL_1 the zero and first-order MQW peak, respectively. "A" is a symbol for an artifact, the analyser streak. Both the substrate and SL_0 peak are elongated along the Ewald sphere intersecting the growth direction with the Bragg angle Θ_B. Thickness fringes inbetween the MQW peaks SL_0 and SL_1 indicate the good crystalline quality of the system. Their spacing corresponds to the total thickness of the superlattice of approximately 640 nm. In Fig. 6.60b the diffraction pattern of the periodic wire array is shown. Wire satellites accompanying the SL_0 peak and the first-order MQW peak SL_1 are observed. The wire period determined from the spacing of the satellites along the q_x direction is 303 nm. The inset in Fig. 6.60b defines the diffraction geometry, the arrow is the normal to the diffraction plane, which is defined by the incident and diffracted (004) X-Ray

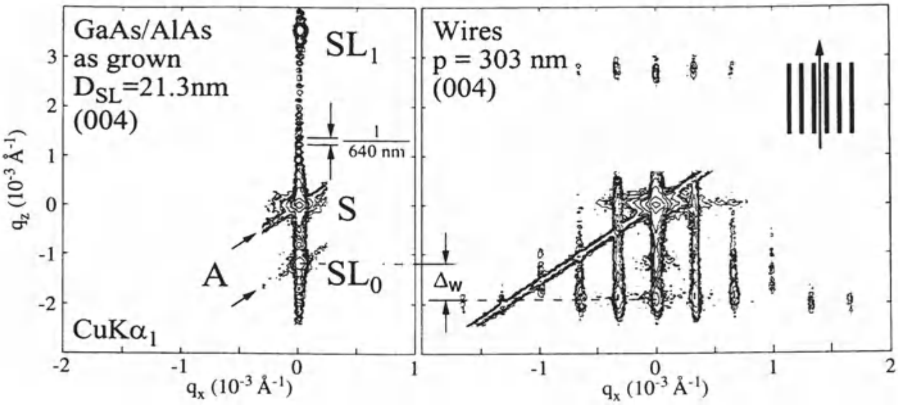

Fig. 6.60. Reciprocal space maps of a MQW GaAs/AlAs reference sample (**a**) and a MQW GaAs/AlAs wire array (**b**) on GaAs(001) around the GaAs (004) reflection. The levels of the isointensity contours are varying between 1.2 to 18000 counts/s in (**a**) and between 1.5 and 15000 counts/s in (**b**)

wavevectors. The half width of the satellite peaks beside the GaAs substrate and buffer peak is much larger than that of the actual GaAs/AlAs dot fringes indicating a corrugation of the GaAs buffer.

In Fig. 6.61 maps for the periodic dot array are shown. The sample was oriented with the [110]-direction perpendicular to the diffraction plane (q_x-direction coincides with [1$\bar{1}$0], (a) and with [100] perpendicular to the diffraction plane (q_x-direction coincides with [010], (b). Clearly dot satellites are observable around the SL_0 satellite RELP. The satellite spacing decreases by a factor of $1/\sqrt{2}$ when the diffraction plane is rotated by 45° out of the principal direction of the dot array Fig. 6.61b. After a further rotation of 45° the original spacing is observed again. From the position of the MQW wire satellites in Fig. 6.60b it is concluded that the mean lattice constant along growth direction is larger than in the unpatterned reference sample Fig. 6.60a, probably due to oxidizing of the AlAs layers upon etching.

Schuller et al. [6.179] investigated GaAs/AlAs short period superlattices which were grown with individual layer thicknesses which were different from integral numbers of atomic planes. This can be viewed as the introduction of controlled interfacial roughness modulation, which caused additional satellite structure. The non-integral but periodic modulation of the AlAs/GaAs SL structure can be interpreted as causing a splitting of the satellites. Schuller et al. interpreted this finding as evidence that controlled interface roughness induces changes in peak positions and not merely changes in peak intensities

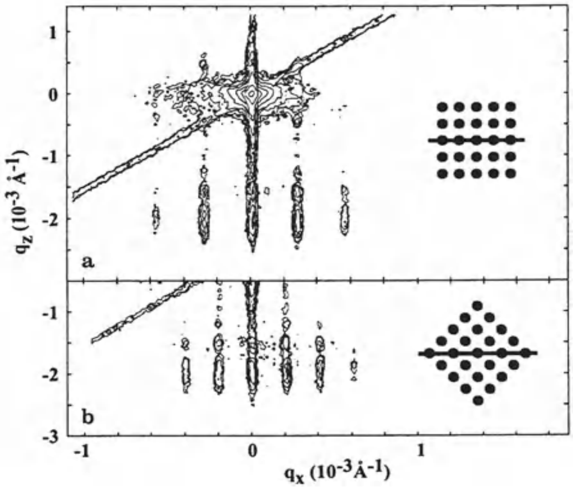

Fig. 6.61. Reciprocal space maps of a periodic MQW GaAs/AlAs dot array for $\phi = 0°$ (**a**) and $\phi = 45°$ (**b**) on GaAs(001). Due to the larger dot period in the incidence plane of the X-Rays in geometry B the satellite spacing in the reciprocal plane is reduced by a factor of $1/\sqrt{2}$

and linewidth, which is the case for random interface roughness. Fullerton et al. [6.154] derived an expression based on kinematical diffraction theory that includes random, continuous, and discrete fluctuations from the average superlattice structure.

Miceli et al. [6.180] measured and modeled both the low angle reflectivity as well as the Bragg scattering for (001) ErAs/GaAs (Fig. 6.62). X-Ray scattering was performed using Mo-K_{α_1} radiation from an 18 kW rotating anode generator and a triple-axis spectrometer with Ge(111) monochromator and analyser crystals. They analysed their data in the kinematical approximation including discrete interface fluctuations and the influence of diffuse scattering. They were able to fit both the data for the specular reflectivity and in the region of the (002) Bragg reflection peak with one single set of data. From their data, the authors concluded that the ErAs films grow with pinholes for 1 or 2 atomic layers of coverage and evolve into continuous films by 5 atomic layers coverage. It is claimed that the extended range reflectivity method gives structural details at the sub-monolayer scale and that the growth morphology of epitaxial layers can consequently be followed throughout the entire growth. Similar experiments were performed by Baribeau [6.181] on nonideal Si/SiGe superlattices. From the comparison of the conventional large angle high resolution X-Ray diffraction patterns on the same sample with the X-Ray reflectivities the interface roughness parameters, thickness fluctuations, and partial strain relaxation could be determined unambiguously.

In particular the X-Ray spectra of thin pseudomorphic epilayers exhibit binomial fluctuations for small numbers of atomic layers. This is characteristic for layer by layer growth. If the number of atomic layers increases Gaussian

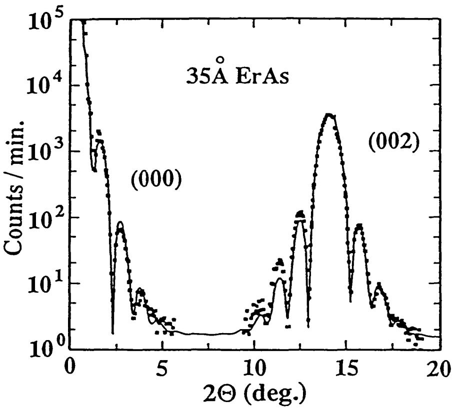

Fig. 6.62. Extended range specular reflectivity for 200 Å a-Si/35 Å ErAs/GaAs(001). The whole spectrum is fitted by one single set of parameters (solid line) both for the specular reflection (000) as well as for the (002) Bragg reflection [6.180].

interface fluctuations occur. For sufficiently thick layers, when lattice relaxation occurs, the intensity distribution indicates exponential fluctuations. The line shape of the intensity distribution along the $q_{\|}$-direction (in the intensity contour plots: ω-direction) yields information on the lateral disorder correlations. As already shown by Sinha et al. [6.182] the intensity distribution along $q_{\|}$ contains two components. The first one is delta-like and the second one is a broad background from diffuse scattering which can even exhibit side peaks. The diffuse scattering originates from lateral fluctuations, usually mosaic-like, at least for the thicker films. The delta-peak stems from flatness over a correlation range of several μm. The intensity of the delta-peak decreases with increasing film thickness, whereas the diffuse scattering intensity increases, especially with the occurrence of misfit dislocations. Miceli has shown, that the lineshapes in $q_{\|}$ geometry change considerably as $q_{\perp}$ is varied from a grazing angle condition to Bragg angle geometry.

Recently, Yasuami et al. [6.183] investigated by diffuse X-Ray scattering the sublattice ordering among group III atoms in $In_{0.5}Ga_{0.5}P$ and in $In_{0.5}Al_{0.5}P$. They determined the Warren-Cowley [6.184] short-range parameters and found excellent agreement with structure models from high resolution transmission electron microscopy.

6.8.2 Real Time X-Ray Diffraction

In-situ HRXRD has been recently applied by Tsuchiya et al. [6.185] for growth monitoring of InGaAs on InP using X-Ray diffraction data as an input for a feedback for the control of the metal organic sources. For that purpose the MOVPE reactor was equipped with Be-windows for the incident radiation, which passed through a Bartels monochromator and for the scattered radiation. A precise control of the lattice mismatch of the growing InGaAs layer was achieved.

Fast structural X-Ray diffraction methods have become possible through the use of synchrotron sources, angular dispersive methods and position-sensitive detectors. Using these advanced methods, problems like the strain relaxation dynamics in epitaxial layers can be addressed as shown by Lowe et al. [6.186]. In a recent study on SiGe films grown on Si substrates in a metastable region close to the critical thickness for misfit dislocation production, evidence was found for the coexistence of different strain states. During rapid thermal treatment the change of the strain status can be followed with a temporal resolution of about 1 s. The results indicate that the interface relaxation process is not dominated by the kinetics of single misfit dislocations but is rather a cooperative phenomenon.

6.9 Grazing-Incidence X-Ray Techniques

So far, the application of different X-Ray diffraction techniques for the characterisation of advanced epitaxial layers has been described. Measurements of the lattice mismatch and — in the case of alloy compounds — composition of epitaxial semiconductor structures are nowadays well established. In recent years ultrathin and thin layers, meaning a few tens to a few hundred Å, as well as multilayer structures are of increasing importance in science and technology. Although high resolution X-Ray techniques are now available, measurements on such structures are complicated because the relatively large penetration depth of X-Rays (typically some μm) leads to a poor surface layer to substrate scattering ratio. Nevertheless, for the past 10 years surface X-ray diffraction has become an important tool to solve various problems in surface and interface science. This development is strongly connected with the rapidly increasing number of high intensity synchrotron X-Ray sources because the diffracted waves are usually of very low intensity. Different techniques like crystal truncation rod analysis, two-dimensional crystallography, three-dimensional structure analysis and the evanescent wave method have been successfully applied. Previous reviews to this field of scattering techniques in surface science were made by Feidenhans'l [6.187], Fuoss and Brennan [6.188] and Robinson and Tweet [6.189]. The surface sensitivity of all widely used X-Ray techniques (diffraction, fluorescence analysis, X-Ray absorption, topography, ...) can be considerably enhanced when the X-Ray beam meets the surface at a glancing angle (a few milliradians) below the critical angle for which total external reflection occurs and an evanescent wave propagating parallel to the surface is created. In the last few years there has been a remarkable increase of the number of experimental and theoretical reports concerning grazing-incidence techniques for probing surfaces, surface layers and internal interfaces (see e.g. [6.190, 6.191]).

In the next subsections a discussion of the applications and capabilities of these techniques is presented. First we shall briefly review the basic concepts of the propagation of X-Ray radiation crossing interfaces. In particular, we shall consider refraction and total reflection of an incident wave at glancing angle. Next the methods of Grazing-Incidence Diffraction (GID) will be discussed.

Figure 6.63 illustrates a typical glancing-angle geometry. Let us consider a plane wave

$$\mathbf{E} = \mathbf{E_0} \exp[\mathrm{i}\,(\mathbf{k} \cdot \mathbf{r} - \omega t)] \tag{6.82}$$

with wavevector $\mathbf{k}_i$ impinging on a sharp interface which separates two different media (e.g. a single-crystal surface in vacuum). The angle of incidence ϑ_i is measured from the plane of the surface. Under suitable conditions, which will be explained below, the incoming wave splits into a reflected (wavevector $\mathbf{k}_r$) and a refracted one (not shown) and also a diffracted wave (wavevector $\mathbf{k}_s$)

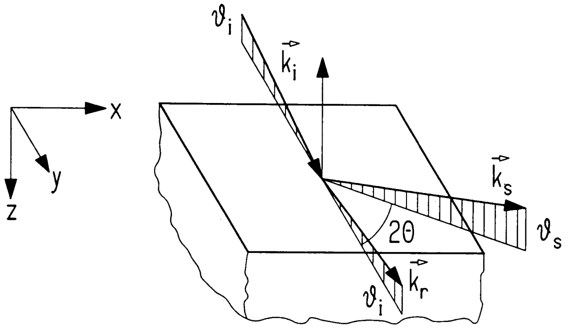

Fig. 6.63. Grazing-incidence geometry. The X-Rays meet the surface at an angle ϑ_i; the beam is diffracted through an angle 2θ and leaves the surface at an angle ϑ_s. 2θ is the angle between the projection of the specularly reflected X-Ray on the surface and the projection of the diffracted one

in the case of obeying the Bragg condition for a lattice plane nearly perpendicular to the surface. The situation for the reflected and refracted wave $\mathbf{k}_t$ is shown separately in Fig. 6.64. For simplicity all angles are assumed to be small (usually $\vartheta < 1°$) so that the small-angle approximation $[\sin(\vartheta) \approx \vartheta]$ can be used.

6.10 Reflection of X-Rays at Grazing Incidence

Refraction and reflection are well-known optical phenomena and are described by Snell's law and the Fresnel equations (see also Chapter 5 on FIR spectroscopy in this textbook) [6.193]. The index of refraction is the fundamental quantity for the description of wave propagation in any media. In the X-Ray range it can be written as [6.194,6.77]:

$$n = 1 - \delta - \mathrm{i}\beta \tag{6.83}$$

with the dispersive term

$$\delta = \frac{N_a r_e \lambda^2}{2\pi} \rho \frac{Z + f'}{A} \tag{6.84}$$

and the absorptive term

$$\beta = \frac{N_a r_e \lambda^2}{2\pi} \frac{\rho f''}{A} = \frac{\mu\lambda}{4\pi} \tag{6.85}$$

[N_a : Avogadro's number, r_e : classical electron radius, λ : wavelength of X-Rays, ρ : mass density, Z : atomic number, f', f'' : real (dispersion) and imaginary (absorption) part of the dispersion corrections [6.195], respectively, A : mass number, μ : linear absorption coefficient [6.196]]

For a multielement specimen in (6.84) and (6.85) the sum is to be taken over the weighted fractions of each element within the compound, respectively. The real part of n, $1 - \delta$, is connected to the phase-lag of the propagating wave, the imaginary part, β, corresponds to the decrease of the wave amplitude. δ and β are small positive quantities of order 10^{-5} to 10^{-7} for X-Ray wavelengths at about 1.5 Å (Tab. 6.2). Consequently, the refractive index is slightly less than 1 and the transmitted wave will be refracted from the normal (Fig. 6.64) according to Snell's law :

$$n_1 \cos \vartheta_i = n_2 \cos \vartheta_t \tag{6.86}$$

It is widely known that the effect of refraction must to be taken into account for precise lattice constant determination from measured Bragg angles [6.34]. On the other hand the deviation from Bragg's law has been used to determine the refractive index of crystals for X-Rays [6.77]. It was Compton [6.197] who first pointed out as early as 1923 that since the refractive index of matter is less than unity for X-Rays it ought to be possible to obtain external total reflection from a smooth surface. He verified his prediction experimentally determining the critical angle ϑ_c for the tungsten L line ($\lambda = 1.28\,\text{Å}$) being totally reflected from a glass surface. Neglecting absorption ($\beta = 0$), the X-Ray critical angle ϑ_c is given by

$$\cos \vartheta_c = n_2 \tag{6.87}$$

which leads, on expansion of the cosine for small angles, to

$$\vartheta_c \approx \sqrt{2\delta_2} \sim \sqrt{\rho(Z + f')\lambda} \tag{6.88}$$

Values of δ, β and ϑ_c (calculated for CuK$_\alpha$ radiation ($\lambda = 1.54\,\text{Å}$)) for three different materials are listed in Table 6.2. External total reflection typically takes place for glancing angles below 0.7° for X-Ray wavelengths at about 1.5 Å (CuK$_\alpha$ radiation).

It is well known from optical theory [6.193] that if the second medium is absorbing, Snell's law (6.86) is only true in a generalised form with a complex

Table 6.2. Comparison of the calculated dispersive term δ, the absorptive term β and the critical angle ϑ_c ($\lambda = 1.54\,\text{Å}$)

	δ	β	ϑ_c
Si	$7.47 \cdot 10^{-6}$	$0.18 \cdot 10^{-6}$	0.22°
GaAs	$14.79 \cdot 10^{-6}$	$0.46 \cdot 10^{-6}$	0.31°
Au	$49.78 \cdot 10^{-6}$	$4.59 \cdot 10^{-6}$	0.57°

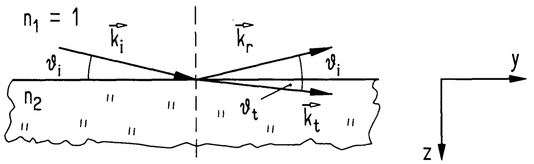

Fig. 6.64. Reflection and refraction of X-Rays incident upon a plane boundary between vacuum ($n_1 = 1$) and a medium whose refractive index n_2 is for X-Rays always less then 1

angle of refraction. This means that the planes of constant amplitude in the medium differ from the planes of constant phase. The refracted wave is conveniently called an inhomogeneous "plane" wave. From (6.86), reformulated in terms of ϑ_c such that

$$\vartheta_t^2 = \vartheta_i^2 - \vartheta_c^2, \tag{6.89}$$

we note that the internal angle ϑ_t is obviously always imaginary for $\vartheta_i < \vartheta_c$. This means that the amplitude of the transmitted wave field drops off exponentially

$$E_t(\mathbf{r}') \propto \exp[\mathrm{i} \cdot \mathrm{Re}(\mathbf{k}_\mathrm{t}) \cdot \mathbf{r}'] \exp[-z/z_0] \tag{6.90}$$

with a damping constant z_0 [6.198]

$$z_0 = \frac{\sqrt{2}}{k}\left[\sqrt{(\vartheta_i^2 - 2\delta_2)^2 + 4\beta_2^2} - (\vartheta_i^2 - 2\delta_2)\right]^{-\frac{1}{2}} \tag{6.91}$$

as the wave penetrates the less dense medium propagating parallel to the surface (y-direction in Fig. 6.64). Figure 6.65 shows the damping constant z_0 as a function of glancing angle ϑ_i. Note that for angles below ϑ_c the amplitude of the so-called evanescent wave decays at a short distance into the solid

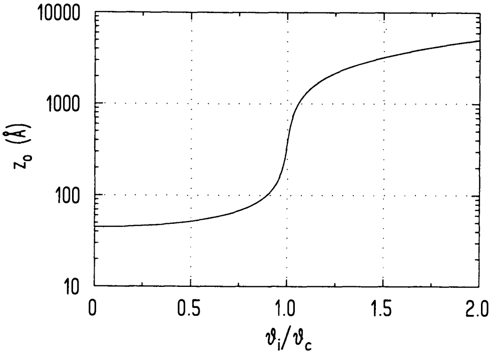

Fig. 6.65. Damping constant z_0 (1/e depth of the transmitted wave amplitude) for CuK$_\alpha$ radiation in GaAs as a function of glancing angles ϑ_i. The critical angle is $\vartheta_c = 0.31°$

(typically 50 Å). This fact makes grazing-incidence X-Ray techniques surface sensitive since the signal originates from a short depth below the surface. On the other hand the penetration of the wave into the bulk can be controlled by increasing the angle of incidence providing precise information on the electron density depth profile.

In order to derive expressions for the reflected and transmitted wave fields one has to apply the boundary conditions found from Maxwell's equations like in optical theory [6.193]. This leads to the Fresnel equations (see also Chapter on FIR spectroscopy) defining the amplitude reflection and transmission coefficients r and t, which are given by

$$r = \frac{\vartheta_i - \vartheta_t}{\vartheta_i + \vartheta_t} \tag{6.92}$$

$$t = \frac{2\vartheta_i}{\vartheta_i + \vartheta_t} \tag{6.93}$$

In the small angle limit considered here, the reflectance $R = r \cdot r^*$ and the transmittance $T = t \cdot t^*$ are independent of polarisation of the incident wave. A detailed discussion of R and T for X-Ray wavelengths is given by Parrat [6.199] and by Vineyard [6.200]. A theoretical reflection curve for GaAs is shown in Fig. 6.66. For angles well below ϑ_c, R becomes nearly unity. When ϑ_i exceeds the critical angle ϑ_c, R drops off rapidly as ϑ^{-4}. But there is obviously no sharp limit of total reflection. The reflectivity is significantly reduced in a range close to ϑ_c. This is due to photoelectric absorption of GaAs which was included in the calculation. It has first been verified by Prins [6.201] and Kiessig [6.202] in a series of experiments, that when X-Ray wavelengths approach the absorption edge of an element, then the sharpness of the limit of total reflection is much affected by the absorption. Their results gave for the first time definite evidence of the existence of anomalous dispersion of X-Rays. Measurements of reflectivity, carried out with synchrotron radiation, have recently been used for the determination of the energy dependence of the

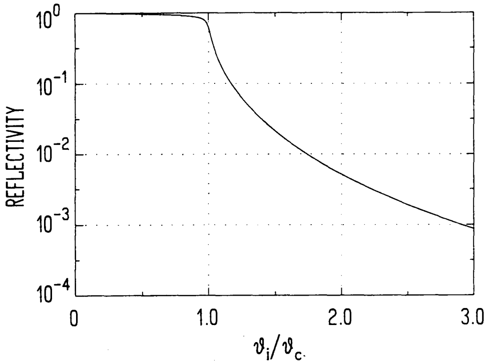

Fig. 6.66. Calculated reflectivity of GaAs (CuK$_\alpha$ radiation) as a function of glancing angles ϑ_i where the surface is perfectly smooth. ϑ_c is 0.31°

anomalous scattering factor f' (6.84) [6.203]. The knowledge of this quantity is quite important for the interpretation of many X-Ray experiments. We have to keep in mind that the critical angle as well as the shape of the Fresnel reflectivity curve (Fig. 6.66) depends on some characteristic material properties only, such as electron density, atomic form factor and absorption coefficient. They are independent of the crystalline structure or the orientation of crystallites on (or in) the surface. However, the measured reflectivity from a real surface departs from the predicted Fresnel reflectivity because in reality a surface is never ideally flat [6.199]. This problem will be discussed in the next Section.

6.11 Specular Reflection and Non-Specular Scattering of X-Rays from Layered Structures

Let us now consider a thin film on a substrate (Fig. 6.67). When the incident angle ϑ_i of the incoming X-Ray wave exceeds ϑ_c for the layer, the reflectivity will show oscillations as a function of ϑ_i due to interferences of waves reflected from the top surface and waves reflected from the interface (Fig. 6.68).

These phase-sensitive structures are geometric resonances known in optics as Fabry-Perot interferences. The angular spacing of the intensity maxima of specularly reflected X-Rays was first measured by Kiessig [6.204] from which he determined the thickness of thin films. For the situation depicted in Figs. 6.67, 6.68, respectively, $n_2 < n_3$, the thickness d is related to the maxima positions ϑ_m by

$$\frac{1}{2}(2m+1)\lambda = 2d \cdot \sqrt{\vartheta_m^2 - \vartheta_c^2} \tag{6.94}$$

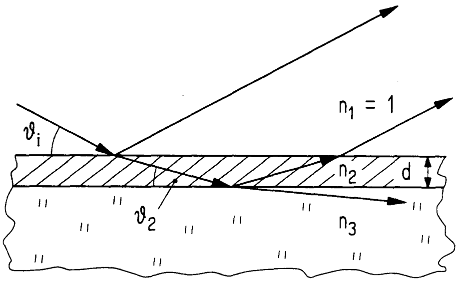

Fig. 6.67. X-Ray reflection at grazing incidence from a layer of thickness d on a substrate ($n_2 < n_3$). The incident beam is partially transmitted. This beam is reflected then back from the layer/substrate interface. The resulting path-length difference determines the interference pattern of the two beams

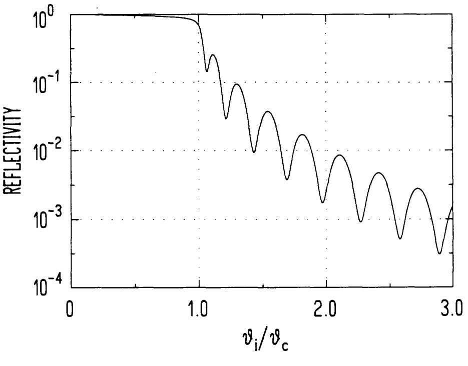

Fig. 6.68. Calculated reflectivity for a 42 nm thick GaAs layer on silicon (CuK$_\alpha$ radiation) assuming ideally abrupt interface and a flat substrate

where m is an integer, λ is the wavelength of the incident radiation. This leads to a linear relationship if the square of the angular position of the maxima, ϑ_m^2, is plotted versus $(m + 1/2)^2$. The slope gives the layer thickness d and intercepts the critical angle for the layer. While the oscillations in the reflectivity profile result from the thickness of the specimen, the amplitude of the oscillations depends upon the contrast at both interfaces, that is the difference of the dispersive term δ (6.84) at the film-to-substrate interface. Consequently, the greater the refractive index difference at the two interfaces, the more pronounced will be the oscillations. For layered structures the analysis of the reflected intensity requires a calculation of the fringe pattern based for example on the recursion formulae given by Parrat [6.199] following from the Fresnel formalism of optical reflection and refraction in a multilayer with smooth interfaces. But in reality, the surface and the interfaces are not atomically sharp, therefore the calculated reflectivity on the basis of the simple model of ideal layers is often in substantial disagreement with the measured data. The interfacial roughness and its correlation from interface to interface in multilayer thin films devices influences also their novel optical, electrical, magnetic, mechanical and superconducting properties. Therefore the knowledge and control of the quality of the interfaces is of both practical and fundamental interest. In several theoretical approaches concerning the X-Ray scattering from non-ideal interfaces (e.g. [6.182, 6.205, 6.206, 6.207]) the rough surface is characterized by the root mean square (rms) roughness σ, the height-height correlation length ξ and an exponent h $(0 < h < 1)$ which determines the texture of the roughness. The scattering from such rough surfaces is split into specular reflection and diffuse scattering terms which can be calculated on the basis of the distorted-wave Born approximation. In many cases a Debye-Waller type roughness factor is successfully incorporated in the Fresnel reflectivity model calculations in order to deduce the rms roughness σ. In the method applied by Vidal and Vincent [6.208] the Fresnel amplitude coefficients r_{Fj} at each interface j is corrected by

$$r_j = r_{Fj} \cdot \exp\left(-2k_j^2\, \vartheta_{ji}\vartheta_{(j+1)i}\, \sigma_j^2\right) \tag{6.95}$$

where σ_j is the rms value of roughness for layer j. The surface roughness determines the decay near ϑ_c while interfacial roughness leads, for layered structures, to progressive damping of the oscillations with increasing angle ϑ_i. But from reflectivity experiments no information on the in-plane correlation length ξ can be obtained. This incoherent contribution affects the scattering of X-Rays into non-specular directions which are observed in a wide angular range around the speculary reflected beam. A typical feature of the diffusely scattered intensity is a maximum if either the angle of incidence or the detection angle equals the critical angle of total reflection. Yoneda [6.209] was the first who observed this anomalous surface reflection for glancing angles. Warren and Clark [6.210] and Guentert [6.211] interpreted the effect in terms of small-angle scattering of surface or interface irregularities. The diffuse scattering technique has proved to be a useful tool for the determination of surface quality and surface contaminants on the atomic scale. In combination with measurements of the reflectivity it is possible to separate the roughness of external and internal interfaces and its correlation in multilayer films as well as to investigate the fractal dimension of the interface [6.206, 6.212, 6.175, 6.213, 6.214].

Furthermore it has been demonstrated that the nonspecular scattering is affected in particular by the vertical roughness correlation [6.215]. These theoretical results have been used for the analysis of specular and nonspecular X-Ray reflectivity experiments on a 20 period MBE-grown AlAs/GaAs SL performed whith a synchrotron source using various scans and reciprocal space mapping around (000).

Some of the principles of specular reflection given in the previous sections will now be illustrated. The characterisation of thin films by means of X-Ray reflectivity measurements under grazing incidence conditions is not restricted to single-crystal samples like in the case of diffraction techniques. One can obtain information on electron density and thickness of single-crystal, polycrystal as well as amorphous films. But also surface and interface roughness on an atomic scale can be analysed. While the reflectivity profile of a single-layer sample often exhibits simple oscillations which can easily be evaluated, in case of multilayer structures the interpretation is not that straightforward. Because of recent improvements of deposition techniques multilayer structures of stratified and periodic media have been produced, which found a wide interest in basic research as well as in applications to the design of electronic and optoelectronic devices, soft X-Ray mirror structures, etc.. X-Ray scattering at small angle has proved to be useful for their characterisation [6.216, 6.217]. A typical situation of a semiconductor superlattice with large period thickness is shown in Fig. 6.69. The sample was nominally 10 * (60 nm GaAs, 20 nm AlAs) grown by MBE on a GaAs substrate. Beyond the critical angle at 0.31°,

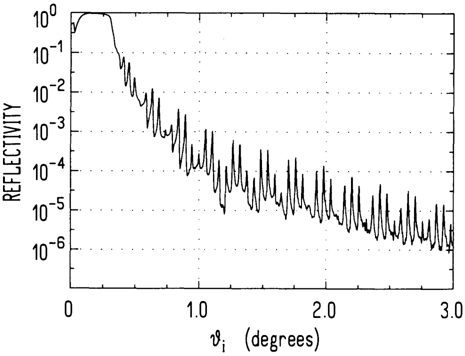

Fig. 6.69. Grazing incidence X-ray reflectivity of a 10 period GaAs/AlAs (d_A = 60 nm, d_B = 200 nm) superlattice grown on (100) GaAs (The sample was grown by A. Förster, ISI, KFA Jülich, the reflectivity measurement was carried out by U. Klemradt, IFF, KFA Jülich)

which corresponds to the value for GaAs, the reflectivity curve exhibits a series of peaks in reflection. A full analysis of the data requires a calculation of the reflected intensity and adjustment of the parameters until a good fit is obtained. For this purpose least-squares curve fitting procedures [6.218] and Fourier analysis [6.219] have been employed.

An good example for the interface characterisation by means of X-Ray total reflection was given by Krol et al. [6.220]. For thin epitaxial $\mathrm{In}_x\mathrm{Ga}_{1-x}\mathrm{As}$ layers ($x = 0.53$ and 0.60) on InP and GaAs substrates they determined the roughness of the interfaces, and epilayer thickness by fitting the soft X-Ray reflectivities (used X-Ray energies 550... 700 eV), assuming a model with uncorrelated interfacial roughness. The surface roughness parameters of all investigated samples were always smaller than interfacial roughness and did not depend on the type of the substrate or presence of stress in the epilayer. They concluded that the surface quality of the substrate and the MBE growth conditions influence more strongly the morphologic structure than strain or lattice mismatch. Slijkerman et al. [6.221] demonstrated that grazing-incidence X-Ray reflection technique is sensitive enough to detect even a delta-doping profile at a depth of a few nanometers below the surface. They characterised samples with a very narrow distribution of Sb dopant atoms capped, after deposition on a Si (001) crystal, with an ultrathin (a few nm) Si overlayer by analysing the reflectivity profiles. A schematic representation of the sample geometry is shown in Fig. 6.70. In the right-hand part, the depth profile of the electron density used in their model calculations is illustrated. The parameters they used to adjust their data (Fig. 6.71) indicate that the Sb doping profile drops off abruptly towards the substrate and more smoothly towards the surface with a 1/e decay length of 1.01 ± 0.37 nm.

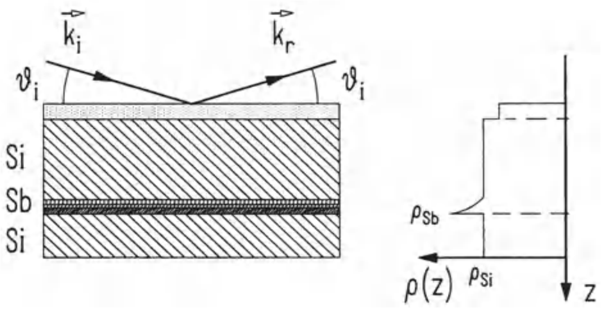

Fig. 6.70. Schematic illustration of a reflectance experiment from a buried delta-doping layer of Sb on Si. The corresponding density depth profile is given in the right-hand part [6.221]

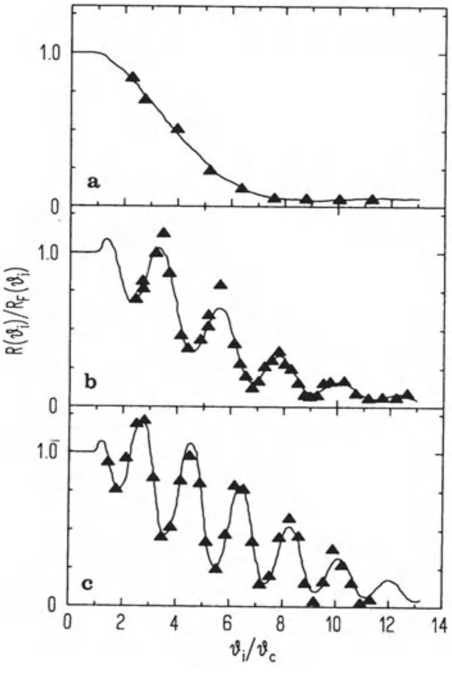

Fig. 6.71. Measured normalised reflectivities $R(\vartheta_i)/R_F(\vartheta_i)$ as a function glancing angle ϑ_i/ϑ_c. **a** Reflectivity data for a sample without Sb. The solid line was simulated for a model with only oxide on top of the sample surface, **b** the reflectivity curve for a Sb delta-doping layer on Si with c-Si cap. The calculated profile (solid line) to the measured data is given by the density profile with exponential Sb decay towards the surface in Fig. 6.70, **c** reflectivity data and fit obtained from a Sb doping profile with an a-Si overlayer [6.221]

Grazing X-Ray reflection was also applied by Baribeau [6.222] to study monolayer-thick buried Ge layers on Si. He measured and analysed strong oscillations, arising from the reflected X-Rays at the Ge/Si interface and the surface of the Si capping layer, for Ge film thicknesses down to one monolayer. The X-Ray data which are in agreement with additional transmission electron microscope studies of the samples, suggest a transition from a two-dimensional to three-dimensional growth mode at Ge coverage of about 6 monolayers. Similar results were obtained from the analysis of X-Ray reflectivity curves from various short-period $(\mathrm{Si}_m\mathrm{Ge}_n)_p$ superlattices [6.223]. Sharp interfaces (half a monolayer wide) were found only for samples grown on Si with $n < 4$. Structures with larger n had rough interfaces owing to three-dimensional growth phenomena. The great sensitivity of X-Ray reflectometry to thickness variations and interfacial roughness makes this technique a powerful tool also for the characterisation of non-ideal multilayer structures. Recently it was demonstrated [6.181], how X-Ray reflectometry can complement double-crystal diffractometry analysis of non-ideal $\mathrm{Si/Si}_{1-x}$ superlattices that contain thickness fluctuations or in which partial strain relaxation is present.

These examples clearly demonstrate the capacity of this X-Ray technique for nondestructive charaterisation of thin films and interfaces. In addition it has been successfully applied to study a wide variety of interesting problems in surface and interface physics and chemistry and also in epitaxial growth. Examples include: average composition determination in multilayer structures [6.224], oxidation of metal and semiconductor surfaces [6.42], structure of Langmuir-Blodgett films [6.225], capillary waves on the surface of liquids [6.226], liquid organic monolayers on water and spreading of polymer micro-droplets on solid surfaces [6.227]. Combined X-Ray fluorescence and reflectivity measurements turned out to be very promising for depth profile element analysis of surface and layer structures [6.228, 6.229, 6.217].

6.12 Grazing-Incidence X-Ray Diffraction

Marra et al. [6.230] demonstrated for the first time that X-Rays striking a sample at a glancing angle can be Bragg scattered from lattice planes normal to the surface of ordered-layered structures. Studying the interface structure of epitaxial Al films on a GaAs single crystal, they achieved an considerably enhanced surface sensitivity under external total reflection conditions. Because of the improved signal-to-noise ratio they were able to measure the lattice spacing parallel to the interface in the Al layer as a function of layer thickness from 1000 down to 35 atomic layers (202 nm to 7.5 nm). Since this first experimental report grazing-incidence X-Ray scattering techniques with simultaneous total external reflection have been rapidly developed and successfully applied to study different aspects of surface and interfaces structures. A general survey of the current state of art is given by the recent conference proceedings [6.190, 6.191]. But the first theoretical concept dealing with this subject has already been treated in the early paper by Farwig and Schürmann [6.231]. Meanwhile the grazing-incidence X-Ray scattering theory has been studied in detail by Vineyard [6.200], Dietrich and Wagner [6.232, 6.233], Afanas'ev and Melkonyan [6.234] and Cowan [6.235]. These approaches range from semikinematic to dynamic scattering theory. The experimental progress in this new and promising research area are stimulated by advanced surface- and thin-film-preparation techniques in combination with the availability of X-Ray facilities like high intensity synchrotron sources. But also laboratory high-resolution X-Ray diffractometers have proved to be useful. The ideas of glancing angles reflectivity and surface diffraction have also been extended to other forms of radiation, particularly thermal neutrons [6.236, 6.237].

A typical scattering geometry is sketched in Fig. 6.72. The X-Ray beam strikes the sample surface at an angle ϑ_i ($< \vartheta_c$) and is specular reflected as described in the previous sections. Bragg diffraction occurs from planes perpendicular to the surface. The scattered X-rays leave the surface at an angle 2θ about the surface normal at a takeoff angle ϑ_s (typically equal to ϑ_i). Conventional Bragg diffraction monitors the structural properties perpendicular to the interface or close to it, in Grazing-Incidence Diffraction (GID) the diffraction vector $\mathbf{k}_{\|}$ is parallel or nearly parallel to the surface. The small perpendicular momentum transfer $\mathbf{k}_z$ (6.98) depending on ϑ_i and ϑ_s has to be carefully considered [6.238, 6.237], too. In many cases the samples of interest exhibit a certain mosaic structure; therefore a semikinematic approach is adequate for the description of the scattering phenomena. The concept is known as "Distorted Wave Born Approximation" (DWBA). The

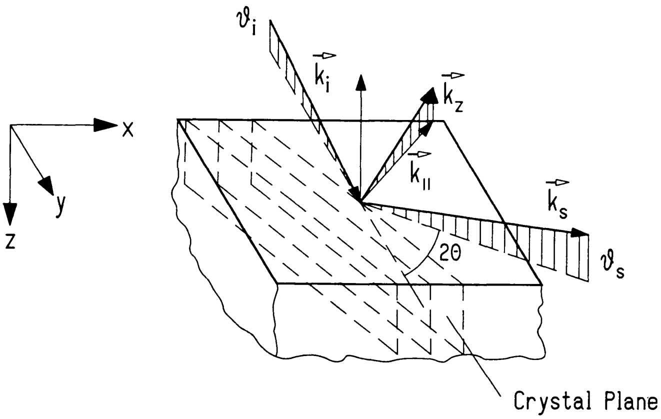

Fig. 6.72. Diffraction geometry under grazing incidence conditions showing incident ($\mathbf{k}_i$), scattered ($\mathbf{k}_s$) wavevectors as well as the components of the scattering vector. The speculary reflected beam is not shown

DWBA was first conceived by Vineyard [6.200] who treated only one grazing angle. Later this approach was extended to an arbitrary scattering geometry by Dietrich and Wagner [6.232, 6.233] and put into practice by Dosch et al. [6.238]. Within the framework of DWBA, the evanescent wave field inside the medium ("distorted wave") instead of the wave field in vacuum is considered to illuminate the crystal. The scattering intensity near the conditions of total external reflection is then given by [6.239]

$$I(k_{\|}, k_z) \sim |t_i|^2 \cdot S(k_{\|}, k_z) \cdot |t_s|^2 \tag{6.96}$$

with the structure factor $S(k_{\|}, k_z)$ for the momentum transfer components $k_{\|}$ parallel and k_z perpendicular to the surface. Furthermore, the Fresnel transmission coefficients $t_{i,s}$ are associated with the angles $\vartheta_{i,s}$

$$t_{i,s} = \frac{2\vartheta_{i,s}}{\vartheta_{i,s} + (\vartheta_{i,s}^2 - \vartheta_c^2)^{\frac{1}{2}}} \tag{6.97}$$

which are related to the amplitude of transmitted wave of the incident and diffracted beams. The ϑ-dependence of $t_{i,s}$ features an interesting phenomenon for $\vartheta_i = \vartheta_c$ (Fig. 6.73).

Here, the amplitude inside the medium is twice that of the incident wave (neglecting absorption) because of the phase matching of the two external waves that form a standing wave in front of the surface. It should be noted that grazing incidence (ϑ_i) and grazing exit (ϑ_s) are equivalent in case of

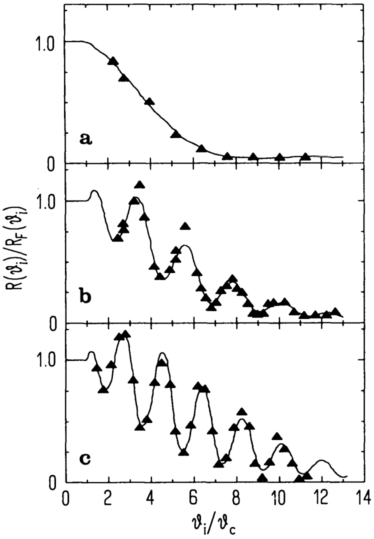

Fig. 6.73. Magnitude of the Fresnel transmission coefficient as a function of ϑ_i/ϑ_c

evanescent X-Ray waves. This interesting property has been experimentally verified by Becker et al. [6.240] detecting absorption (external incidence) and emission (internal excitation in the vicinity of a surface) of X-Ray waves in the total reflection region. Taking into account the refraction correction, k_z is given inside the solid by [6.233]:

$$k_z = k_{iz} - k_{sz} = \frac{2\pi}{\lambda}\left[(\sin^2\vartheta_i - 2\delta - i2\beta)^{\frac{1}{2}} + (\sin^2\vartheta_s - 2\delta - i2\beta)^{\frac{1}{2}}\right] \quad (6.98)$$

Whenever both angles ϑ_i and ϑ_s are less than ϑ_c ($\sin^2\vartheta_c = 2\delta$), $\mathrm{Re}(k_z)$ vanishes in the case of no absorption, although the vacuum value may be unequal zero. The consequences for Bragg scattering are that $\vartheta_{i,s}$ can be controlled independently within the total reflection regime without affecting the Bragg condition which has to be fulfilled inside the crystal. The associated scattering depth Λ for which the scattered intensity is reduced by 1/e is defined as [6.238]:

$$\Lambda \equiv |\,\mathrm{Im}(k_z)|^{-1} \quad (6.99)$$

This length has to be distinguished from the penetration depth z_0 (6.91) of the evanescent wave which depends only on the the incidence angle α_i. Because of (6.98) Λ is symmetrically dependent on ϑ_i and ϑ_s. Fixing one of the angles, ϑ_i or ϑ_s, at a value below ϑ_c the other one can be chosen freely, providing a variation of Λ between a minimum value of typically 20…50 Å and a maximum which is independent on the scanning angle (Fig. 6.74). The situation is qualitatively different when the fixed angle ϑ_i in Fig. 6.74,

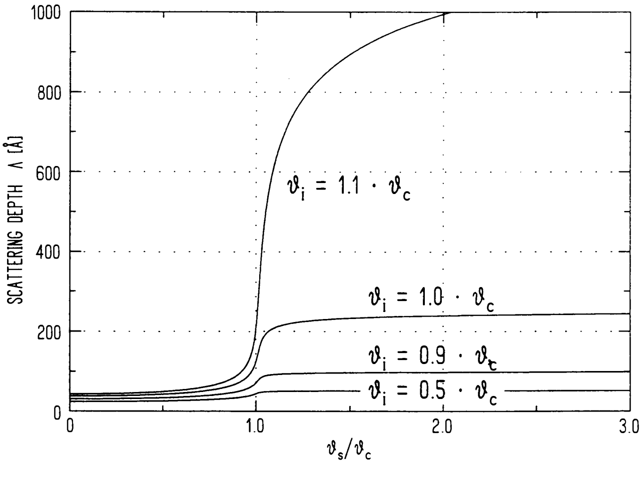

Fig. 6.74. Calculated scattering depth Λ for GaAs as a function of ϑ_s/ϑ_c for different incident angles ϑ_i/ϑ_c

exceeds ϑ_c. Although for $\vartheta_s/\vartheta_c \leq 1$ there still exists an evanescent wave ("grazing exit diffraction") in this case the upper limit of Λ is determined by photoabsorption and increases continuously with ϑ_s.

The behavior of Λ in the vicinity of total reflection has to be carefully considered when discussing surface Bragg scattering [6.238]. Figure 6.75 shows the results for the measured intensity distributions of the (222) reflection from a Fe_3Al $(\bar{1}10)$ surface for different incident and exit angles [6.238]. The Bragg maximum is displaced from its bulk position ($\vartheta_{i,s} = 0$) by an amount comparable to ϑ_c. These results can be qualitatively understood as follows. At small angles Λ is also small and so is the effective number of layers participating in the diffraction, thereby reducing the scattered intensity. The maximum in the diffracted intensity appears near $\vartheta_{i,s} \approx \vartheta_c$ because at larger angles $\mathrm{Re}(k_z)$ becomes finite and the Bragg condition is no longer obeyed. This effect overcompensates the increase of the scattering depth Λ. Similar scattering studies were carried out at highly perfect single crystals in order to get data for a detailed comparison with dynamical scattering theory (see e.g. [6.241,6.242]). Because of the properties of X-Ray waves outside and inside a perfect crystal, the calculated profiles of the specular reflected and diffracted beam show interesting features which are not described by the kinematical approximation [6.234,6.235].

High angular resolution measurements were achieved with synchrotron radiation revealing some of these features. Although effects of natural oxide layers [6.243] and of a tilt angle between the scattering lattice planes and surface normal has been carefully considered in the interpretation of the experimental data systematic deviations are still observed [6.241]. Recently

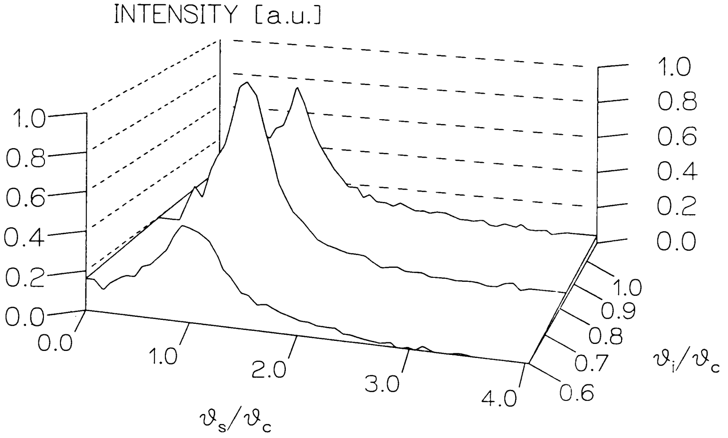

Fig. 6.75. Intensity profiles of an in-plane Bragg reflection from Fe_3Al (100) as a function of the take off angle ϑ_s/ϑ_c at three different glancing angles ϑ_i/ϑ_c [6.238]

Stepanov [6.244] proposed an explanation of the disagreements giving corrections for the angular dependence of the parameter α which describes the deviation from the Bragg condition. He also outlined ideas for further experimental tests which should to be taken on very clean crystal surfaces utilizing back diffraction conditions ($\Theta_B \approx 90°$).

The high angular resolution which is required in probing near surface profiles leads to very low intensity of the diffracted waves, so this kind of measurements are commonly performed with synchrotron radiation. A different diffraction scheme, for which a conventional X-Ray source is sufficient, has been proposed by Golovin and Imamov [6.245]. Instead of measuring the angular dependence of the intensity of the diffracted beam the whole diffracted cone is recorded with an open detector for varied angle of incidence of a well collimated X-Ray beam. Rahn and Pietsch [6.246, 6.247] demonstrated the application of the so-called "integral mode" for the characterisation of nanometer heterostructure layers. In their experimental setup they measured both the GID and the grazing-incidence reflectivity simultaneously. From the analysis of the profiles it was possible to separate the contributions of crystalline and amorphous part of the layer to the signals.

In order to determine both crystallite size and strains parallel to the interface also "$\Theta - 2\Theta$" scans are performed as in conventional diffraction. The direction of the scattering vector $\mathbf{k}_{\|}$ remains fixed, but the magnitude changes.

The interpretation of the data is straightforward and the structural properties are obtained from the formalism described in the previous passages of this Chapter. Segmüller et al. [6.3] applied this GID technique to characterise very different kinds of epitaxial films with thicknesses down to a few atomic layers. Although with their scattering arrangement depth profiling cannot be done, nor are the intensity calculation feasible, the measurements performed with a laboratory rotating anode X-Ray generator demonstrate the great application potential of GID in laboratory environment for thin film characterisation. Complementary results are obtained by symmetric Bragg diffraction along the direction parallel to the surface normal. In thin epitaxial InAs layers on GaAs (001) substrates Munekata et al. [6.248] detected for example by GID two domains with different strain distribution (Fig. 6.76). Conventional Bragg scattering only gives the domain with the relatively low strain.

Taking advantage of synchrotron sources, which provide high intensity in combination with small beam divergence, complex dynamic surface processes of scientific and technological importance can be characterised by high resolution surface scattering. The first *in-situ* grazing-incidence X-Ray scattering studies of a chemical vapor deposition process were presented by Fuoss et al. [6.249]. The authors directly observed the Organometallic Vapour-Phase Epitaxial (OMVPE) growth of ZnSe on GaAs(001). While the characteristic p(2 × 4) reconstruction was monitored from a clean GaAs surface, after an

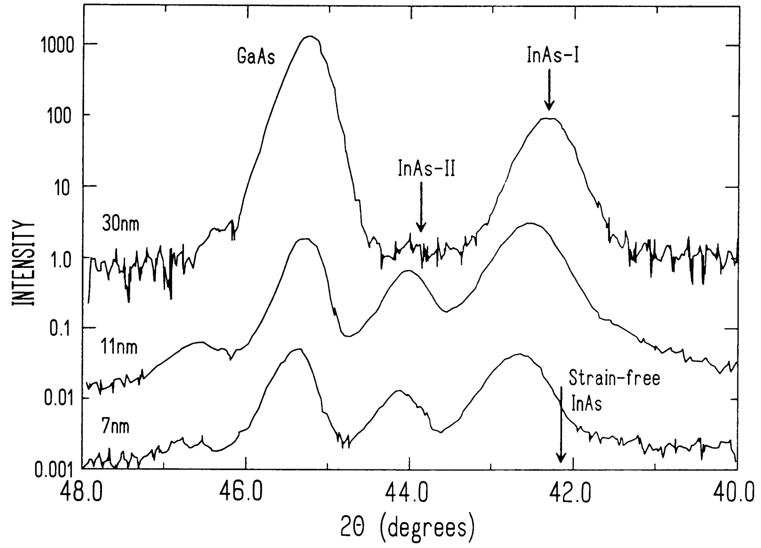

Fig. 6.76. (220) reflections of thin epitaxial InAs layers on GaAs (001) of different thicknesses obtained by X-Ray grazing-incidence diffraction. Two InAs domains with different strains are evident: a weekly strained InAs-I and a strongly strained InAs-II [6.248]

initial transient, a very well defined (2 × 1) ZnSe reconstruction was found independent of growth conditions. In a further experiment, they observed cyclic changes in X-Ray reflectivity of growing ZnSe films during alternating source epitaxy (Fig. 6.77). These oscillations are believed to characterise the kinetics of the decomposition of the selenium source compound [6.250]. Further interesting applications of grazing-incidence scattering for the atomic scale characterisation of OMVPE growth have recently been reported by Kisker et al. [6.251] and Lamelas et al. [6.252]. Several surface reconstructions were unambiguously determined for the growth of GaAs under OMVPE conditions. The nucleation of islands, their growth and finally, coalescence was observed by monitoring the surface sensitive crystal truncation rods. In addition, the average island spacing, its temperature dependence, and the anisotropy of the islands shape has been estimated from the diffuse scattering near the truncation rods. These are a particularly interesting example of the capacity of X-Ray techniques for surface studies so far thought to be the domain of electron diffraction techniques (e.g. RHEED, LEED).

In this short review only the basic aspects of X-Ray surface scattering techniques could be summarised. Its importance for nondestructive surface sensitive characterisation of epitaxial thin films has been demonstrated at several examples. Since X-Ray reflection does not depend on strain distribution

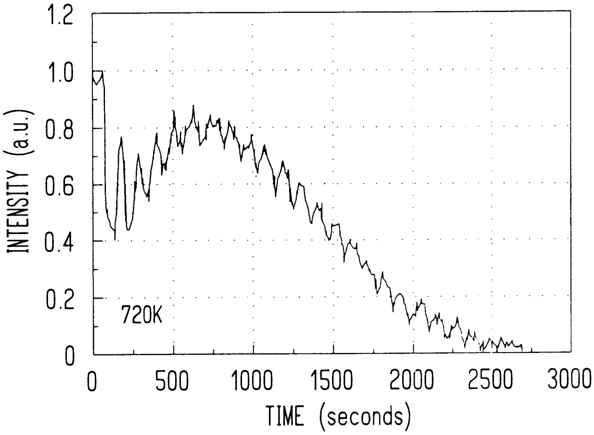

Fig. 6.77. Intensity oscillations from the specularly reflected X-Ray beam during alternating source epitaxial growth of ZnSe at 450 °C. For this study the film grew while the gas flow of the Se and Zn source was abruptly switched on and off [6.250]

or defects within a microstructure it allows the study also of heavily-defected structures or even amorphous materials. The reflectivity data can be used to determine the thickness of layers, the depth profiles of the electron density as well as interface and surface roughness. Simultaneous measurements of the X-Ray fluorescence which is excited by the standing wave formed at total reflection give information on the compositional properties of thin films and surfaces. This combination appears to be a promising new technique for non-destructive near-surface analysis. In case of crystalline samples Bragg diffraction under total external reflection conditions can be studied. Taking advantage of the reduced penetration depth crystallite size, strain, lateral lattice mismatch as well as mosaic spread in very thin epitaxial layers are determined. Although the available high intense synchrotron sources offer the suitable experimental conditions to perform all kind of grazing incidence measurements with variable X-Ray energies, conventional X-Ray sources have also proved to be applicable. For a more extensive treatment to this subject, we refer to the numerous original papers and recent reviews.

6.13 Summary

High-resolution X-Ray diffraction has become a standard tool in many laboratories where emphasis is on the growth of epitaxial layers and layer systems. Double-crystal diffractometry has been recently in widespread use and the introduction of commercially available instrumentation, especially the four-crystal monochromator has opened a wide field of applications. Through its non-destructive nature it is ideal for the determination of composition of heteroepitaxial layers, of their thicknesses, of strains and of interdiffusion at heterointerfaces. Through careful analysis strain relaxation in layers with thicknesses beyond the critical thickness for misfit dislocation can also be obtained. Lattice mismatch can be measured with an accuracy of $1.4 \cdot 10^{-5}$ (!). The tilt of epilayers with respect to their substrates can be determined as well.

The instrumentation has been further developed and nowadays triple-axis spectrometers or double-crystal diffractometers equipped with position-sensitive detectors allow one to perform a mapping of the reciprocal space. These maps are particulary advantageous for the analysis of not so perfect heterosystems or superlattices or of epilayers which show even some mosaicity. Further recent developments are the combination of high resolution X-Ray diffraction with X-Ray topography which is useful for producing maps of lattice strains with lateral resolutions down to 1 micrometer. Standard semiconductor wafers (thicknesses of 0.5 mm) can be used for this technique in transmission.

Structuring heteroepitaxial layers laterally has become quite important in order to realise 1-dimensional or 0-dimensional electronic systems. X-Ray diffraction techniques can be succesfully employed in order to determine the lateral periodicity of quantum wires or dots.

The use of synchrotron sources has permitted a real-time analysis of strain relaxation in heteroepitaxial layers and *in-situ* analysis during growth.

Grazing incidence diffraction has become a versatile technique for the characterisation of epitaxial layers during the past ten years. Since in this technique the diffraction vector is parallel to the surface, this method is quite sensitive to all properties which have to be probed in regions close to the surface or interface. In particular strains, crystallographic orientation and crystallite size, or domains within very thin epitaxial films can be determined by this technique. With rotating anodes or synchrotron radiation sources even monolayers are accessible.

6.14 Concluding Remarks

Due to the vast interest in epitaxial thin films (not necessarily semiconducting layers) there has been a rapid development in several X-Ray diffraction methods. Since the films are usually deposited on rather thick substrates with conventional laboratory instrumentation only the Bragg case reflection is accessible. Double crystal diffraction has become a general tool, usual in conjunction with several epitaxial techniques for immediate feedback of structural qualities of heterostructures, multilayers and superlattices for the crystal grower.

The use of an analyser crystal between the sample and the detector has become popular. Reciprocal space maps provide much more information than

rocking-curve modelling alone. Whereas for the latter extensive software is generally available for the former such kind of analysis programs are right now under development. Since the reciprocal space maps provide information on the films both in the direction of the surface normal as well as parallel to it, it is forseeable that triple-crystal techniques will become as important as double-crystal techniques are nowadays. Together with further developments in grazing incidence techniques which yield some new complementary information, X-Ray techniques provide a wealth of structural information on heteroepitaxial systems which range from crystallography, also for layers covered by others, as well as surface and interface morphology.
New directions are:

- *in-situ* growth control using Bragg diffraction of growing films, for a feedback to influence the growth process directly. This technique has so far been realised for MOVPE using DCD (with a Bartels type of monochromator [6.185]).
- Observation of *in-situ* growth with grazing incidence techniques relying on high intensity X-Ray sources such as a synchrotron [6.250].
- Observation of *in-situ* strain relaxation in Si/Ge growth, again using synchrotron radiation [6.186].
- extended range specular reflectivity [6.180] which starts at grazing angle incidence and extends to Bragg scattering at higher angles in a single experiment (using a rotating anode generator as a source). This technique seems to provide unique information on specular and diffuse scattering which combined in the analysis yields information on atomically discrete interface fluctuations.

In our opinion it is just a matter of time until also *in-situ* X-Ray diffraction will be used in conjunction with molecular beam growth technology. *In-situ* X-Ray scattering provides important additional information which is not easily or not at all obtainable with *in-situ* reflection high energy electron diffraction which is so far used as a standard probe in MBE growth:

- *in-situ* control of layer uniformity, chemical composition, and thickness.
- *in-situ* control of interdiffusion,
- *in-situ* control of structural, chemical, and morphological changes of buried layers due to subsequent growth process of further layers.

Whereas the use of synchrotron radiation tremendeously increases the sensitivity of X-Ray scattering due to monolayers and surfaces, standard laboratory instrumentation provides a wealth of the type of information outlined above. Due to its non-destructive nature the role of X-Ray diffraction will likely even increase as an invaluable method for probing the structural properties of heterostructures in near future.

References

1.1 B. A. Joyce: Rep. Prog. Physics **48**, 1637 (1985)

1.2 D. L. Partin: in *Semiconductors and Semimetals*, ed. T.P. Pearsall (Academic Press N.Y.) **33**, 331 (1991)

1.3 R. L. Gunshor, L. A. Kolodziejski, A. V. Nurmikko, N. Otsuka: in *Semiconductors and Semimetals*, ed. T. P. Pearsall, (Academic Press N.Y.) **33**, 337 (1991)

1.4 A. Y. Cho: J. Crystal Growth **111**, 1 (1991)

1.5 M. Razeghi: *The MOCVD Challenge*, (Adam Hilger, Bristol 1989)

1.6 E. Kasper, J. C. Bean: *Silicon Molecular Beam Epitaxy*, (CRC Press Florida 1988)

1.7 E. Kasper, F. Schäffler: in *Semiconductors and Semimetals*, ed. T. P. Pearsall (Academic Press N.Y.) **33**, 223 (1991)

1.8 M. A. Herman, H. Sitter: *Molecular Beam Epitaxy*, (Springer Berlin, Göttingen, Heidelberg 1989)

1.9 M. Illegems: in *Technology and Physics of Molecular Beam Epitaxy*, ed. E. M. C. Parker (Plenum Press N.Y.), p. 83 (1985)

1.10 P. K. Larsen and P. J. Dobson: in *Reflection High Energy Electron Diffraction and Reflection Electron Imaging of Surfaces* (NATO ARW, Plenum Press, N.Y. 1988)

1.11 D. E. Aspnes: in *Handbook on Semiconductors*, Vol.2, Ed. M. Balkanski (North-Holland Publishing Company 1980), p. 109

1.12 D. E. Aspnes: Proc. SPIE Aachen 1991, **1361**, p. 551

1.13 W. Richter: Phil. Trans. R. Soc. Lond. **A344**, 453 (1993)

1.14 S. M. Koch, O. Acher, F. Omnes, M. Defour, B. Drevillon, M. Razeghi: J. Appl. Phys. **69**, 3 (1991)

1.15 P. F. Fewster: Applied Surface Science **50**, 9 (1991)

1.16 A. Segmüller, I. C. Noyen, V. S. Speriosa: Progress in Crystal Growth and Characterization **18**, 21 (1989)

1.17 B. K. Tanner: in *Analysis of Microelectronic Materials and Devices*, eds. M. Grasserbauer and H. W. Werner (J. Wiley and Sons, Chichester and New York 1991), p. 609

1.18 A. Segmüller: J. Vac. Sci. Technology **A9**, 2447 (1991)

1.19 E. Betzig and J. Trautman: Science **257**, 189 (1992)

1.20 E. L. Buckland, P. J. Moyer and M. A. Paesler: J. Appl. Phys. **73**, 1018 (1993)

1.21 M. Henzler: Surface Science **152/153**, 963 (1985)

1.22 M. P. Seah: Vaccum **34**, 453 (1984)

1.23 M. Grasserbauer and H. W. Werner (eds.): *Analysis of Microelectronic Materials and Devices*, (J. Wiley, Chichester and New York 1991)

1.24 A. Benninghoven, F. G. Lüdemann, H. Werner: *Secondary Ion Mass Spectroscopy*, (J. Wiley, New York 1987)

1.25 S. T. Picraux, B. L. Doyle, J. Y. Tsao: in *Semiconductors and Semimetals*, ed. T. P. Pearsall (Academic Press N.Y.) **33**, 139 (1991)

1.26 W. F. van der Weg and F. H. P. M. Habraken: in *Analysis of Microelectronic Materials and Devices*, eds. M. Grasserbauer and H. W. Werner (J. Wiley and Sons, Chichester and New York), p. 563 (1991)

1.27 H. Cerva and H. Oppholzer: Prog. Crystal Growth and Characterisation **20**, 189 (1990)

1.28 H. Cerva: Appl. Surface Science **50**, 19 (1991)

1.29 F. A. Ponce, G. B. Anderson, J. M. Ballignall: Surface Science **168**, 564 (1986)

1.30 L. Reimer: *Transmission Electron Microscopy*, (Springer Series in Optical Science **36**, 1989)

1.31 D. E. Newbury, D. C. Joy, P. Ecklin, C. E. Fiori, J. I. Goldstein: *Advanced Scanning Electron Microscopy and X-Ray Analysis* (Plenum Press, N.Y. 1986)

1.32 *Scanning Tunneling Microscopy*, I, II, and III
H.-J. Güntherodt, R. Wiesendanger (eds.) (Springer Series in Surface Science, 1992)

1.33 R. C. Newman: in *Growth and Characterisation of Semiconductors*, R. A. Stradling and P. C. Klipstein (eds.) (Adam Hilger, Bristol), p. 119 (1990)

1.34 R. A. Stradling and P. C. Klipstein: *Growth and Characterization of Semiconductors* (Adam Hilger, Bristol 1990)

1.35 T. Dumelow, T. J. Parker, S. R. P. Smith, D. R. Tiley: Surf. Sci. Rep. **17**, 151 (1993)

1.36 M. Cardona and L. Ley: in *Photoemission in Solids* I and II, Topics in Applied Physics **26** and **27** (1978)

1.37 G. V. Marr: *Handbook on Synchrotron Radiation* (North Holland, Amsterdam) **2** (1987)

1.38 *Principles, Applications, Techniques of EXAFS, SEXAFS and XANES*, C. C. Koningsberger and R. Prius (eds.) (Wiley, New York 1988)

1.39 E. C. Lightowlers: in *Growth and Characterisation of Semiconductors*, R. A. Stradling and P. C. Klipstein (eds.) (Adam Hilger, Bristol), p. 135 (1990)

1.40 M. A. Herman, J. Christen, D. Bimberg: J. Appl. Phys. **70**, R1 (1991)

1.41 F. H. Pollak: in *Proceedings of the Society of Photo-Optical Instrumentation Engineers, San Jose*, D. E. Aspnes, S. So, R. F. Potter (eds.), SPIE, Bellingham (1981)

1.42 M. Cardona and G. Güntherodt: *Light Scattering in Solids* II to V, Topics in Applied Physics, **50** (1982), **51** (1982), **54** (1984), **66** (1989), (Springer, Berlin, Heidelberg, New York)

1.43 J. B. Theeten: Surface Science **96**, 275 (1980)

1.44 HRXRD Conf. Proc., J. Phys. D **26**, 4A (1993)

1.45 Z. J. Radzimski, B. I. Jiang, G. A. Rozgonyi, T. P. Humphreys, N. Hamaguchi, S. M. Bedair: J. Appl. Phys. **64**, 2328 (1988)

1.46 R. Köhler, Proc. HRXRD Workshop, Aigen 1992, Appl. Phys. **A58**, 149 (1994)

2.1 M. A. Herman, H. Sitter: *Molecular Beam Epitaxy* (Springer Berlin, Göttingen, Heidelberg 1989)

2.2 K. Ploog: *Angewandte Chemie* **100**, 611 (1988)

2.3 B. A. Joyce: Rep. Prog. Physics **48**, 1637 (1985)

2.4 A. Y. Cho: J. Crystal Growth **111**, 1 (1991)

2.5 A. Lopez-Otero: Thin Solid Films **49**, 1 (1978)

2.6 G. H. Olsen, T. J. Zamerowski: Prog. Cryst. Growth Characterisation **2**, 309 (1979)

2.7 G. B. Stringfellow: *Metalorganic Vapour Phase Epitaxy* (North Holland, Amsterdam 1986)

2.8 M. Razeghi: *The MOCVD Challenge*, Vol. 1, (Adam Hilger, Bristol 1989)

2.9 E. Kuphal, D. Fritzsche: J. Electr. Mat. **12**, 743 (1983)

2.10 M. G. Astles: *Liquid Phase Epitaxial Growth of III-V Compound Semiconductor Materials and Their Device Applications*, (Hilger, Bristol 1990)

2.11 D. Fotiadis, M. Boekholt, K. F. Jensen, W. Richter: J. Crystal Growth **100**, 577 (1990)

2.12 F. Durst, A. Melling, J. H. Whitelaw: *Principle and Practice of Laser Doppler Anemometry* (Academic Press, London, UK 1976)

2.13 R. J. Schodl: Fluid Eng. **102**, 412 (1980)

2.14 L. Stock, W. Richter: J. Crystal Growth **77**, 144 (1986)

2.15 W. Richter: Festkörperprobleme XXVI, Advances in Solid State Physics **26**, 335 (1986)

2.16 K. F. Jensen: J. Cryst. Growth **98**, 148 (1989)

2.17 K. C. Chiu, F. Rosenberger: Int. J. Heat and Mass Transfer **30**, 1645 (1987)

2.18 A. Compaan, H. J. Trodahl: Phys. Rev. **29**, 793 (1984)

2.19 A. Weber: *Raman Spectroscopy of Gases and Liquids* (Springer Berlin, 1979), p. 123

2.20 T. O. Sedgwick, J. E. Smith, R. Ghez, M. E. Cowher: J. Crystal Growth **31**, 264 (1975)

2.21 T. O. Sedgwick, J. E. Smith: J. Electrochem. Soc. **123**, 254 (1976)

2.22 J. E. Smith, T. O. Sedgwick: Thin Solid Films **40**, 1 (1977)

2.23 G. A Hebner, K. P. Killeen, R. M. Bielfeld: J. Crystal Growth **98**, 293 (1989)

2.24 V. M. Donnelly, R. F. Karlicek: J. Appl. Phys. **53**, 6399 (1982)

2.25 M. L. Fischer, R. Lückerath, P. Balk, W. Richter: Chemtronics **3**, 156 (1988)

2.26 K. P. Killeen: Appl. Phys. Lett. **61**, 1864 (1992)

2.27 J. E. Butler, N. Bottka, R. S. Sillmon, D. K. Gaskill: J. Crystal Growth **77**, 163 (1986)

2.28 P. Ho, W. G. Breiland: J. Appl. Phys. **63**, 5184 (1988)

2.29 W. G. Breiland, P. Ho, M. E. Coltrin: J. Appl. Phys. **60**, 1505 (1986)

2.30 W. G. Breiland, M. E. Coltrin, P. Ho: J. Appl. Phys. **59**, 3267 (1986)

2.31 P. Ho, W. G. Breiland: Appl. Phys. Lett. **44**, 51 (1984)

2.32 P. Ho, W. G. Breiland: Appl. Phys. Lett. **43**, 125 (1983)

2.33 S. Ishizaka, J. Simpson, J. O. Williams: Chemtronics **1**, 175 (1986)

2.34 K. J. Mackey, D. C. Rodway, P. C. Smith, A. W. Vere: Chemtronics **5**, 85 (1991)

2.35 W. G. Breiland, M. J. Kushner: Appl. Phys. Lett. **42**, 395 (1983)

2.36 M. Koppitz, W. Richter, R. Bahnen, M. Heyen: in Springer Series in Chemical Physics **39**, Laser Processing and Diagnostics, ed. by D. Bäuerle, Springer Verlag, Berlin, p. 530 (1984)

2.37 Y. Monteil, R. Favre, P. Raffin, J. Bouix, M. Vaille, P. Gibart: J. Crystal Growth **93**, 159 (1988)

2.38 S. A. J. Druet, J. P. E. Taran: Prog. Quant. Electr. **7**, 1 (1981)

2.39 R. Brakel, F. W. Schneider: in *Advances in Spectroscopy* Vol. 15, eds. R. J. H. Clark, R. E. Hester, Wiley, Chichester 1988

2.40 W. Richter, P. Kurpas, R. Lückerath, M. Motzkus: J. Crystal Growth **107**, 13 (1991)

2.41 M. Alden, A. L. Schawlow, S. Svanberg, W. Wendt, P. L. Zhang: Optics Letters **9**, 211 (1984)

2.42 International Colloquium on Optogalvanic Spectroscopy and its Application, J. de Physique Colloque **C7**, 44 (1983)

2.43 G. Leyendecker, J. Doppelbauer, D. Bäuerle, P. Geittner, H. Lydtin: Appl. Phys. **A30**, 237 (1983)

2.44 W. Richter, P. Kurpas, R. Lückerath, M. Motzkus: J. Crystal Growth **107**, 13 (1991)

2.45 M. E Coltrin, R. J. Kee, J. A. Miller: J. Electrochem. Soc. **131**, 425 (1984)

2.46 R. Lückerath, P. Tommack, A. Hertling, H. J. Koss, P. Balk, K. F. Jensen, W. Richter: J. Crystal Growth **93**, 151 (1988)

2.47 T. J. Mountziaris, K. F. Jensen: J. Electrochem. Soc. **138**, 2426 (1991)

2.48 M. P. Seak, W. A. Dench: Surf. Interf. Anal. **1**, 2 (1979)

2.49 D. E. Aspnes, A. A. Studna: Phys. Rev. **B27**, 985 (1983)

2.50 M. Cardona, F. H. Pollak, K. L. Shaklee: J. Phys. Soc. Jap. **21**, 89 (1966)

2.51 R. M. A. Azzam: Optics Communications **19**, 122 (1976)

2.52 H. Wormeester, D. J. Wentink, P. L. deBoeij, C. M. J. Wijers, A. van Silfhout: Phys. Rev. B **47**, 12663 (1993)

2.53 D. E. Aspnes, J. P. Harbison, A. A. Studna, L. T. Folrez: J. Vac. Sci. Technol. **A6**, 1327 (1988)

2.54 D. E. Aspnes: J. Vac. Sci. Technol. **B3**, 1498 (1985)

2.55 P. Chiaradia, G. Chiarotti, F. Ciccacci, R. Memeo, S. Nannarone, P. Sassaroli, S. Selci: Surf. Sci. **99**, 70 (1980)

2.56 P. Chirardia, A. Skrebtii, C. P. Goletti, Wang-Jian, R. del Sole: Surface Science **85**, 497 (1993)

2.57 C. P. Goletti, P. Chirardia, Wang-Jian, G. Chiarotti: Solid State Commun. **84**, 421 (1992)

2.58 D. K. Biegelsen, R. D. Bringans, J. E. Northrup, A. Schwartz: Phys. Rev. **B 41**, 5701 (1990)

2.59 S. N. Jasperson, S. E. Schnatterly: Rev. Sci. Instr. **40**, 761 (1969)

2.60 A. A. Studna, D. E. Aspnes, L. T. Florez, J. P. Harbison and R. Ryan: J. Vac. Sci. Technol. **A7**, 3291 (1989)

2.61 D. E. Aspnes, Y. C. Chang, A. A. Studna, L. T. Florez, H. H. Farrell, J. P. Harbison: Phys. Rev. Lett. **64**, 192 (1990)

2.62 L. Däweritz, R. Hey: Surf. Sci. **236**, 15 (1990)

2.63 S. M. Koch, O. Acher, F. Omnes, M. Defour, B. Drevillon, M. Razeghi: J. Appl. Phys. **69**, 1389 (1991)

2.64 T. Yasuda, D. E. Aspnes, D. R. Lee, C. H. Bjorkman and G. Lucovsky: J. Vac. Sci. Technol. **A12**, 1152 (1994)

2.65 D. E. Aspnes, J. P. Harbison, A. A. Studna, L. T. Florez: Phys. Rev. **B59**, 1687 (1987)

2.66 J. J. Harbison, D. E. Aspnes, A. A. Studna, L. T. Florez and M. K. Kelly: Appl. Phys. Lett. **52**, 2046 (1988)

2.67 F. Briones, D. Golmayo, L. Gonzalez, J. L. de Miguel: J. Appl. Phys. Japan **24**, L478 (1985)

2.68 J. E. Epler, T. A. Jung, H. P. Schweizer, Appl. Phys. Lett. **62**, 143 (1993)

2.69 B. Y. Maa, P. D. Dapkus, P. Chen, A. Madhukar: Appl. Phys. Lett. **62**, 2551 (1993)

2.70 E. Colas, D. E. Aspnes, R. Bhat, A. A. Studna, J. P. Harbison, L. T. Florez, M. A. Koza, V. G. Keramidas: J. Cryst. Growth **107**, 47 (1991)

2.71 I. Kamiya, H. Tanaka, D. E. Aspnes, L. T. Florez, E. Colas, J. P. Harbison, R. Bhat: Appl. Phys. Lett **60**, 1238 (1992)

2.72 I. Kamiya, D. E. Aspnes, H. Tanaka, L. T. Florez, E. Colas, J. P. Harbison, R. Bhat: Applied Surface Science **60/61**, 534 (1992)

2.73 I. Kamiya, D. E. Aspnes, H. Tanaka, L. T. Florez, J. P. Harbison, R. Bhat: Phys. Rev. Lett. **68**, 627 (1992)

2.74 Y.-Ch. Chang, D. E. Aspnes: J. Vac. Sc. Technol. **8**, 896 (1990)

2.75 D. W. Kisker, G. B. Stephenson, P. H. Fuoss, F. J. Lamelas, S. Brennan, P. Imperatori: J. Crystal Growth **124**, 1 (1992)

2.76 K. Ploska, W. Richter, F. Reinhardt, J. Jönson, J. Rumberg, M. Zorn, MRS Proceedings **334**, 155 (1993)

2.77 M. Wassermeier, I. Kamiya, D. E. Aspnes, L. T. Florez, J. P. Harbison, P. M Petroff: J. Vac. Sci. Technol. **B9**, 2263 (1991)

2.78 I. Kamiya, D. E. Aspnes, H. Tanaka, L. T. Florez, J. P. Harbison, R. Bhat: J. Vac. Sci. Technol. **B10**, 1716 (1992)

2.79 L. Samuelson, K. Deppert, S. Jeppesen, J. Jönnson, G. Paulsson, P. Schmidt: Crystal Properties and Preparation **32**, 338 (1991)

2.80 L. Samuelson, K. Deppert, S. Jeppesen, J. Jönsson, G. Paulsson, P. Schmidt: J. Cryst. Growth **107**, 68 (1991)

2.81 O. Acher, S. M. Koch, F. Omnes, M. Defour, B. Drevillon, M. Razeghi: *Condensed Systems of Low Dimensionality*, ed. by J. L. Beeby et al., (Plenum Press, New York 1991)

2.82 F. Reinhardt, W. Richter, A. B. Müller, D. Gutsche, P. Kurpas, K. Ploska, K. C. Rose, M. Zorn: J. Vac. Sci. Technol. **B11**, 1427 (1993)

2.83 W. Richter: Phil. Trans. R. Soc. London A **344**, 453 (1993)

2.84 P. Kurpas, J. Jönssson, W. Richter, D. Gutsche, M. Pristovsek, M. Zorn: J. Cryst. Growth **145**, 35 (1994)

2.85 M. Zorn, J. Jönsson, A. Krost, W. Richter, J.-T. Zettler, K. Ploska, F. Reinhardt: J. Cryst. Growth **145**, 53 (1994)

2.86 K. Ploska, J.-T. Zettler, J. Jönsson, F. Reinhardt, M. Zorn, J. Rumberg, M. Pristovsek, W. Richter: J. Cryst. Growth **145**, 44 (1994)

2.87 F. Reinhardt, J. Jönsson, M. Zorn, W. Richter, K. Ploska, J. Rumberg, P. Kurpas: J. Vac. Sci. Technol. **B12**, 2541 (1994)

2.88 S. M. Scholz, A. B. Müller, W. Richter, D. R. T. Zahn, D. I. Westwood, D. A. Woolf, R. H Williams: J. Vac. Sci. Technol. **B10**, 1710 (1992)

2.89 N. Kobayashi, Y. Horikoshi: Jpn. J. Appl. Phys. **28**, L1880 (1989)

2.90 N. Kobayashi, Y. Horikoshi: Jpn. J. Appl. Phys. **30**, L319 (1991)

2.91 T. Makimoto, Y. Yamauchi, N. Kobayashi, Y. Horikoshi: Jpn. J. Appl. Phys. **29**, L645 (1990)

2.92 N. Kobayashi, Y Horikoshi: Jpn. J. Appl. Phys. **29**, L702 (1990)

2.93 N. Kobayashi, Y. Horikoshi: Jpn. J. Appl. Phys. **30**, L1443 (1991)

2.94 K. Hingerl, D. E. Aspnes, I. Kamiya, L. T. Florez: Appl. Phys. Lett. **63**, 885 (1993)

2.95 H. Ibach, D. L. Mills: *Electron Energy Loss Spectroscopy and Surface Vibrations* (Academic Press, New York 1982)

2.96 A. Förster: Ph.D. Thesis RWTH Aachen (1988)

2.97 Y. J. Chabal: Surf. Sci. Reports **8**, 211 (1988)

2.98 R. G. Greenler: J. Chem. Phys. **44**, 310 (1966)

2.99 H. Ibach: Surf. Sci. **66**, 56 (1977)

2.100 M. A. Chesters, A. B. Horn, E. J. C. Kellar, S. F. Parker, R. Raval, in: *Mechanisms of Reaction of Organometallic Compounds with Surfaces*, eds. D. J. Cole-Hamilton, J. O. Williams, NATO ASI Series, Series:B, Physics **198**, Plenum (1989)

2.101 J. D. E. McIntyre, D. E. Aspnes: Surf. Sci. **24**, 417 (1971)

2.102 D. S. Buhaenko, S. M. Francis, P. A. Goulding, M. E. Pemble: J. Cryst. Growth **97**, 591 (1989)

2.103 H. Patel, M. E. Pemble: J. Phys. IV, Colloq. **1**, 167 (1991)

2.104 N. Bloembergen, R. K. Chang, S. S. Jha, C. H. Lee: Phys. Rev. **174**, 813 (1968)

2.105 H. W. K. Tom, T. F. Heinz, Y. R. Shen: Phys. Rev. Lett. **51**, 1983 (1983)

2.106 T. F. Heinz, M. M. T. Loy., W. A. Thompson: Phys. Rev. Lett. **54**, 63 (1985)

2.107 H. W. K Tom., G. D. Aumiller: Phys. Rev. **B33**, 8818 (1986)

2.108 J. F. McGilp , Y. Yeh: Solid State Commun. **59**, 91 (1986)

2.109 J. F. McGilp: Semicond. Sci. Technol. **2**, 102 (1987)

2.110 J. F. McGilp: J. Vac. Sci. Technol. **A5**, 1442 (1987)

2.111 J. F. McGilp: J. of Phys.: Condens. Matter **2**, 7985 (1990)

2.112 D. Guidotti, T. A. Driscoll, H. J. Gerritsen: Solid State Commun. **46**, 337 (1983)

2.113 T. Stehlin, M. Feller, P. Guyot-Sionnest, Y. R. Shen: Opt. Letts. **13**, 389 (1988)

2.114 R. W. J. Hollering, A. J. Hoeven, J. M. Lenssinck: J. Vac. Sci. Technol. **A8**, 3194 (1989)

2.115 M. E. Pemble, D. S. Buhaenko, S. M. Franas, P. A. Goulding, J. T. Allen: J. Cryst. Growth **107**, 37 (1991)

2.116 J. M. Olson, A Kibbler: J. Cryst. Growth **77**, 182 (1986)

2.117 D. J. Robbins, A. J. Pidduck, A. G. Cullis, N. G. Chew, R. W. Hardeman, D. B Gasson, C. Pickering, A. C. Daw, M. Johnson, R. Jones: J. Cryst. Growth **81**, 421 (1987)

2.118 C. Pickering, D. J. Robbins, I. M. Young, J. L. Glasper, M. Johnson, R. Jones: Mater. Res. Soc. Symp. Proc. **94**, 173 (1987)

2.119 A. J. Pidduck, D. J. Robbins, A. G. Cullis, D. B. Glasson, J. L. Glasper: J. Electrochem. Soc. **136**, 3083 (1989)

2.120 A. J. Pidduck, D. J. Robbins, D. B. Glasson, C. Pickering, J. L. Glasper: J. Electrochem. Soc. **136**, 3088 (1989)
2.121 E. L. Church, H. A Jenkinson, J. M. Zavada: Opt. Eng. **18**, 125 (1979)
2.122 G. W. Smith, A. J. Pidduck, C. R. Whitehouse, J. L. Glasper, A. M. Keir, C. Pickering: Appl. Phys. Lett. **59**, 3282 (1991)
2.123 W. Tsang, R. F. Hampson: J. Phys. Chem. Ref. Data **15**, 1087 (1986)
2.124 M. E. Coltrin, R. J. Kee, J. A. Miller: J. Electrochem. Soc. **133**, 1206 (1986)
2.125 M. Tirowidjo, R. Pollard: J. Crystal Growth **93**, 108 (1988)

3.1 J. Jamin: Ann. de chim. et phys. **29**, 263 (1850)
3.2 P. Drude: Ann. d. Phys. Chem. (Leipzig) **34**, 489 (1888)
3.3 D. E. Aspnes, A. A. Studna: Phys. Rev. **B27**, 985 (1983)
3.4 A. Röseler: *Infrared Spectroscopic Ellipsometry* (Akademie Verlag, Berlin, Germany 1990)
3.5 R. M. A. Azzam, N. M. Bashara: *Ellipsometry and Polarized Light* (North-Holland Publishing Company 1977)
3.6 F. L. McCrackin, E. Passaglia, R. R. Stromberg, H. L. Steinberg: J. of Res. Nat. Bur. of Stan. **67A**, 363 (1963)
3.7 D. E. Aspnes: J. Opt. Soc. Am. **64**, 812 (1974)
3.8 D. E. Aspnes, A. A. Studna: Appl. Opt. **14**, 220 (1975)
3.9 P. S. Hauge, F. H. Dill: IBM J. Res. Dev. **17**, 472 (1973)
3.10 S. N. Jasperson, S. E. Schnatterly: Rev. Sci. Instr. **40**, 761 (1969)
3.11 S. N. Jasperson, D. K. Burge, R. C. O'Handley: Surf. Sci. **37**, 548 (1973)
3.12 J. C. Kemp: *Polarized Light and its Interaction with Modulating Devices* (Hinds Int. Inc. 1987)
3.13 H. Mueller: J. Opt. Soc. Am. **38**, 661 (1948)
3.14 C. Pickering, D. J. Robbins, I. M. Young, J. L. Glasper, M. Johnson, R. Jones: Mat. Res. Soc. Symp. Proc. **94**, 173 (1987)
3.15 J. F. Nye: *Physical Properties of Crystals* (Clarendon Press, Oxford 1985)
3.16 M. Born: *Optik* (Springer, Berlin 1985) 2nd edition
3.17 see for example: Hamamatsu Technical Notes TN-106-03 *Super Quiet Xenon Lamps*, August 1984
3.18 E. Hecht, A. Zajac: *Optics* (Addison-Wesley 1974) chapter 8
3.19 D. E. Aspnes: J. Opt. Soc. Am. **64**, 639 (1974)
3.20 N. V. Nguyen, B. S. Pudliner, Ilsin An, R. W. Collins: J. Opt. Soc. Am. **A8**, 919 (1991)
3.21 O. Acher, E. Bigan, B. Drevillon: Rev. Sci. Instr. **60**, 65 (1989)
3.22 B. Drevillon: Thin Solid Films **163**, 157 (1988)
3.23 F. Ferrieu, D. Dutatre: J. Appl. Phys. **68**, 5810 (1990)
3.24 J. Brehmer, O. Hunderi, K. Fanping, T. Skauli, E. Wold: Appl. Optics **31**, 471 (1992)
3.25 K.-L. Barth, D. Böhme, K. Kamaras, F. Keilmann, M. Cardona: Thin Solid Films **234**, 314 (1993)
3.26 R. L. Johnson, J. Barth, M. Cardona, D. Fuchs, A. M. Bradshaw: Rev. Sci. Instr. **60**, 2209 (1989)
3.27 Proceedings of the first conference on spectroscopic ellipsometry, ICSE Paris 1993 in: Thin Solid Films **233/234** (1993)
3.28 R. M. A. Azzam, K. A. Giardina, A. G. Lopez: Optical Engineering **30**, 1583 (1991) and references therein

3.29 P. S. Hauge: Surf. Sci. **96**, 108 (1980)
3.30 J. A. Woollam, P. G. Snyder: J. Appl. Phys. **62**, 4867 (1987)
3.31 R. Calvani, R. Caponi, F. Cisternino: Optics Communication **54**, 63 (1985)
3.32 F. Bassani, G. Pastori Parravicini: *Electronic States and Optical Transitions in Solids* (Pergamon Press, Oxford, 1975)
3.33 M. Cardona: in *Modulation Spectroscopy*, Suppl. **11** of Solid State Physics, edited by F. Seitz, D. Turnbull, and H. Ehrenreich (Academic Press, New York 1969)
3.34 P. Lautenschlager, Ph.D. Thesis, University of Stuttgart 1987
3.35 J. R. Chelikowski, M. L. Cohen: Phys. Rev. **14**, 556 (1976)
3.36 H. Arwin, D. E. Aspnes: J. Vac. Sci. Technol. **A2**, 1316 (1984)
3.37 Landolt-Börnstein, New series, Vol. 15b, Springer, Berlin 1985
3.38 J. H. Weaver, C. Krafka, D. W. Lynch, and E. E. Koch: in *Physik Daten: Optical Properties of Metals*, Nr. 18-1 (Fachinformationszentrum Energie, Physik, Mathematik GmbH, Karlsruhe, 1981), pp. 239 ff.
3.39 *Handbook of Optical Constants of Solids*, edited by E. D. Palik (Academic Press, New York 1985)
3.40 D. E. Aspnes: in *Handbook on Semiconductors*, Vol. 2 ed. M. Balkanski (North Holland, Amsterdam 1980)
3.41 C. C. Kim, J. W. Garland, H. Abad, P. M. Raccah: Phys. Rev. **B45**, 11749 (1992)
3.42 K. Cho: in *Excitons*, edited by K. Cho, Topics in Current Physics (Springer, Berlin, Heidelberg, New York 1979)
3.43 D. E. Aspnes, R. P. H. Chang: Mat. Res. Soc. Symp. Proc. **29**, 217 (1984)
3.44 G. E. Jellison: Optical Materials **1**, 41 (1992)
3.45 D. E. Aspnes, G. P. Schwartz, G. J. Gualtieri, A. A. Studna, B. Schwartz: J. Electrochem. Soc. **128**, 590 (1981)
3.46 L. Viña, M. Cardona: Phys. Rev. **B29**, 6739 (1984)
3.47 B. Drevillon, C. Godet, S. Kumar: Appl. Phys. Lett. **50**, 1651 (1987)
3.48 S. Logothetidis, G. Kiriakidis: J. Appl. Phys. **64**, 2389 (1988)
3.49 L. Viña, S. Logothetidis, M. Cardona: Phys. Rev. **B30**, 1979 (1984)
3.50 D. E. Aspnes, C. E. Bouldin, E. A. Stern: in *Proc. 17th Internat. Conf. Physics of Semiconductors*, ed. J. D. Chadi and W. A. Harrison (Springer, New York 1985), p. 841.
3.51 D. E. Aspnes: *Spectroscopic Ellipsometry of Solids*, in B. O. Seraphin (ed.) *Optical Properties of Solids* (North Holland, Amsterdam 1976), chapter 15
3.52 M. Cardona, D. L. Greenaway: Phys. Rev. **A133**, 1685 (1964)
3.53 U. Rossow, U. Frotscher, N. Esser, U. Resch, Th. Müller, W. Richter, D. A. Woolf, R. H. Williams: Appl. Surf. Sci. **63**, 35 (1993)
3.54 R. Strümpler, H. Lüth: Thin Solid Films **177**, 287 (1989)
3.55 B. J. Schäfer, A. Förster, M. Londschien, A. Tulke, K. Werner, M. Kamp, H. Heinecke, M. Weyers, H. Lüth, P. Balk: Surf. Sci. **204**, 485 (1988)
3.56 O. Hunderi: J. Phys. **F5**, 2214 (1975)
3.57 O. Hunderi, R. Ryberg: J. Phys. **F4**, 2096 (1974)
3.58 D. Y. Smith, E. Shiles, M. Inokuti: in *Handbook of Optical Constants of Solids*, edited by E. D. Palik (Academic, New York, 1985), Table XII
3.59 D. L. Greenaway, G. Harbeke, F. Bassani, E. Tosatti: Phys. Rev. **178**, 1340 (1969)

3.60 H. Arwin, D. E. Aspnes: Thin Solid Films **138**, 193 (1986)

3.61 J. Wagner, P. Lautenschlager: J. Appl. Phys. **59**, 2044 (1986)

3.62 U. Schmid, J. Humlíček, F. Lukes, M. Cardona, H. Presting, H. Kibbel, E. Kasper, K. Eberl, W. Wegscheider, G. Abstreiter: Phys. Rev. **B45**, 6793 (1992)

3.63 S. Ninomiya, S. Adachi: Jpn. J. Appl. Phys. **33**, 2479 (1994)

3.64 S. Zollner, C. Lin, E. Schönherr, A. Böhringer, M. Cardona: J. Appl. Phys. **66**, 383 (1989)

3.65 M. Garriga, P. Lautenschlager, M. Cardona, K. Ploog: Solid State Commun. **61**, 157 (1987)

3.66 D. E. Aspnes, S. M. Kelso, R. A. Logan, R. Bhat: J. Appl. Phys. **60**, 754 (1986)

3.67 H. Burkhard, H. W. Dinges, E. Kuphal: J. Appl. Phys. **53**, 655 (1982)

3.68 S. Logothetidis, J. Petalas, M. Cardona, T. D. Moustakas: Proc. of the EMRS, Strasbourg, France, May 24–27, 1994 in print

3.69 S. Adachi, S. Ozaki: Jpn. J. Appl. Phys. **32**, 4446 (1993)

3.70 M. von der Emde, U. Rossow, G. Kudlek, A. Hoffmann, A. Krost, W. Richter, S. Morley, A. C. Wright, J. O. Williams, D. R. T. Zahn: Proc. of the ICFSI-4 Jülich, 14-18 June 1993, p. 684
eds. B. Lengeler, H. Lüth, W. Mönch, J. Pollmann (World Scientific Press Singapore, New Jersey, London, Hong Kong 1994)

3.71 S. Logothetidis, L. Viña, M. Cardona: Phys. Rev. **B31**, 947 (1985)

3.72 S. Adachi, T. Taguchi: Phys. Rev. **B43**, 9569 (1991)

3.73 M. Aven, D. T. F. Marple, B. Segall: J. Appl. Phys. **32**, 2261 (1961)

3.74 J. L. Freeouf: Phys. Rev. **B7**, 3810 (1973)

3.75 S. Ozaki, S. Adachi: Jpn. J. Appl. Phys. **32**, 5008 (1993)

3.76 M. Cardona, M. Weinstein, G. A. Wolff: Phys. Rev. **140**, A633 (1965)

3.77 S. Adachi: J. Appl. Phys. **68**, 1198 (1990)

3.78 K. Sato, S. Adachi: J. Appl. Phys. **73**, 926 (1993)

3.79 S. Logothetidis, M. Cardona, P. Lautenschlager, M. Garriga: Phys. Rev. **B34**, 2458 (1986)

3.80 S. Adachi, T. Kimura, N. Suzuki: J. Appl. Phys. **74**, 3435 (1993)

3.81 W. H. Weber, J. T. Remillard, J. R. McBride: Phys. Rev. **B46**, 15085 (1992)

3.82 N. Suzuki, S. Adachi: Jpn. J. Appl. Phys. **33**, 193 (1994)

3.83 R. Matz, H. Lüth: Appl. Phys. **18**, 123 (1979)

3.84 M. Altwein, H. Finkenrath, C. Konak, J. Stuke, G. Zimmerer: Phys. Stat. Sol. **29**, 203 (1968)

3.85 S. Logothetidis, P. Lautenschlager, M. Cardona: Phys. Rev. **B33**, 1110 (1986)

3.86 H. J. Trodahl, L. Viña: Phys. Rev. **B27**, 6498 (1983)

3.87 F. Ferrieu, C. Viguier, A. Cros, A. Humbert, O. Thomas, R. Madar, J. P. Senateur: Solid State Commun. **62**, 455 (1987)

3.88 F. Ferrieu, J. H. Lecat: Thin Solid Films **164**, 43 (1988)

3.89 C. Viguier, A. Cros, A. Humbert, C. Ferrieu, O. Thomas, R. Madar, J. P. Senateur: Solid State Commun. **60**, 923 (1986)

3.90 J. R. Jimenez, Z.-C. Wu, L. J. Schowalter, B. D. Hunt, R. W. Fathauer, P. J. Grunthaner, T. L. Lin: J. Appl. Phys. **66**, 2738 (1989)

3.91 H.-W. Chen, J.-T. Lue: J. Appl. Phys. **59**, 2165 (1986)

3.92 P. Chindaudom, K. Vedam: Thin Solid Films **234**, 439 (1993)

3.93 D. E. Aspnes, B. Schwartz, A. A. Studna, L. Derick, L. A. Koszi: J. Appl. Phys. **48**, 3510 (1977)

3.94 I. H. Malitson: J. Opt. Soc. Am. **55**, 1205 (1965)

3.95 L. Pajasova: Czech. J. Phys. **B19**, 1265 (1969)

3.96 H. J. Mattausch, D. E. Aspnes: Phys. Rev. **B23**, 1896 (1981)

3.97 J. Barth, R. L. Johnson, M. Cardona, D. Fuchs, A. M. Bradshaw: Phys. Rev. **B41**, 3291 (1990)

3.98 S. Y. Kim, K. Vedam: Thin Solid Films **166**, 325 (1988)

3.99 G. M. Hale, M. R. Querry: Appl. Opt. **12**, 555 (1973)

3.100 D. E. Aspnes, S. M. Kelso: SPIE Proc. **452**, 79 (1983)

3.101 D. E. Aspnes, H. J. Stocker: J. Vac. Sci. Technol. **21**, 413 (1982)

3.102 B. Drevillon, E. Bertran, P. Alnot, J. Olivier, M. Razeghi: J. Appl. Phys. **60**, 3512 (1986)

3.103 H. W. Dinges, H. Burkhard, R. Lösch, H. Nickel, W. Schlapp: Appl. Surf. Sci. **54**, 477 (1992)

3.104 S. Imai, S. Adachi: Jpn. J. Appl. Phys. **32**, 3860 (1993)

3.105 S. Ozaki, S. Adachi: J. Appl. Phys. **75**, 7470 (1994)

3.106 S. Ozaki, S. Adachi: Jpn. J. Appl. Phys. **32**, 2620 (1993)

3.107 S. Adachi, T. Kimura: Jpn. J. Appl. Phys. **32**, 3496 (1993)

3.108 L. Viña, C. Umbach, M. Cardona, L. Vodopyanov: Phys. Rev. **29**, 6752 (1984)

3.109 P. Lautenschlager, S. Logothetidis, L. Viña, M. Cardona: Phys. Rev. **B32**, 3811 (1985)

3.110 S. M. Kelso, D. E. Aspnes, M. A. Pollack, R. E. Nahory: Phys. Rev. **B26**, 6669 (1982)

3.111 J. Humlíček, E. Schmidt, L. Bočánek, M. Garriga, M. Cardona: Solid State Commun. **73**, 127 (1990)

3.112 S. Adachi, H. Kato, A. Moki, K. Ohtsuka: J. Appl. Phys. **75**, 478 (1994)

3.113 D. E. Aspnes, B. Schwartz, A. A. Studna, L. Derick, L. A. Koszi: J. Appl. Phys. **48**, 3510 (1977)

3.114 W. H. Press, B. P. Flannery, S. A. Teukolsky, W. T. Vetterling: *Numerical Recipes in C: The Art of Scientific Computing* Cambridge University Press, 1988

3.115 J. C. Maxwell-Garnett: Phil. Tr. of the Roy. Soc. of London **203**, 385 (1904) and **205A**, 237 (1906)

3.116 H. Looyenga: Physica **31**, 401 (1965)

3.117 D. A. G. Bruggeman: Ann. Phys. (Leipzig) **24**, 636 (1935)

3.118 D. E. Aspnes: SPIE Proc. **452**, 60 (1983)

3.119 D. Bergman: Phys. Rep. **C43**, 377 (1978)

3.120 D. Bergman: *Bulk physical properties of composite media, Les methodes de l'homogeneisation*, Edition Eyrolles (1985)

3.121 W. Theiß, Ph.D. Thesis, RWTH Aachen 1989

3.122 S. Logothetidis, H. M. Polatoglou, S. Ves: Solid State Commun. **68**, 1075 (1988)

3.123 Y. Cong, R. W. Collins, R. Messier, K. Vedam, G. F. Epps, H. Windischmann: J. Vac. Sci. Techn. **A9**, 1123 (1991)

3.124 S. M. Sze: *VLSI Technology* (McGraw Hill 1988)

3.125 P. Lautenschlager, P. B. Allen, M. Cardona: Phys. Rev. **B31**, 2163 (1985)

3.126 U. Rossow, J. Wagner, W. Richter: unpublished

3.127 R. W. Collins, J. M. Cavese: J. Appl. Phys. **60**, 4169 (1986)

3.128 J. Stuke, G. Zimmerer: Phys. Stat. Sol. **B49**, 513 (1972)

3.129 M. Erman, J. B. Theeten, P. Chambon, S. M. Kelso, D. E. Aspnes: J. Appl. Phys. **56**, 2664 (1984)

3.130 R. E. Williams: *GaAs Processing Technology* (Artech House Inc. 1984)

3.131 M. Erman, J. B. Theeten, P. Frijlink, S. Gaillard, F. J. Hia, C. Alibert: J. Appl. Phys. **56**, 3241 (1984)

3.132 U. Rossow, A. Krost, T. Werninghaus, K. Schatke, W. Richter, A. Hase, H. Künzel, H. Roehle: Thin Solid Films **233**, 180 (1993)

3.133 M. A. Haase, J. Qiu, J. M. DePuydt, H. Cheng: Appl. Phys. Lett. **59**, 1272 (1991)

3.134 S. Yamaga: Jpn. J. Appl. Phys. **30**, 437 (1991)

3.135 D. R. T. Zahn, Ch. Maierhofer, A. Winter, M. Reckzügel, R. Srama, U. Rossow, A. Thomas, K. Horn, W. Richter: Appl. Surf. Sci. **56-58**, 684 (1992)

3.136 D. R. T. Zahn, G. Kudlek, U. Rossow, A. Hoffmann, I. Broser, W. Richter: Adv. Mat. for Opt. and Electr. **3**, 11 (1994)

3.137 T. Matsuno, H. Masato, A. Ryoji, K. Inoue: Proceedings of *Int. Symp. on Gallium arsenide and related compounds*, Karuizawa (Japan), Sept. 1992, T. Ikegami, F. Hasegawa, Y. Takeda eds., Inst. Phys. Conf. Ser. **129**, 729 (1993) Institute of Physics, Bristol (UK)

3.138 A. Adams, E. O'Reilly: Physics World **5**(10), 43 (1992)

3.139 J. Kircher, W. Böhringer, W. Dietrich, H. Hirt, P. Etchegoin, M. Cardona: Rev. Sci. Instr. **63**, 3733 (1992)

3.140 L. T. Canham: Appl. Phys. Lett. **57**, 1046 (1990)

3.141 A. Bsiesy, J. C. Vial, F. Gaspard, R. Herino, M. Ligeon, F. Muller, R. Romestain, A. Wasiela, A. Halimaoui, G. Bomchil: Surf. Sci. **254**, 195 (1991)

3.142 R. T. Carline, C. Pickering, N. S. Garawal, D. Lancefield, L. K. Howard, M. T. Emeny: SPIE proc. **1678**, 285 (1992)

3.143 S. Luryi, E. Suhir: Appl. Phys. Lett. **49**, 140 (1986)

3.144 H. Münder, C. Andrzejak, M. G. Berger, T. Eickhoff, H. Lüth, W. Theiß, U. Rossow, W. Richter, R. Herino, M. Ligeon: Appl. Surf. Sci. **56-58**, 6 (1992)

3.145 V. Lehmann, H. Cerva, U. Gösele: Mat. Res. Soc. Symp. Proc. **256**, 3 (1992) *Light Emission from Silicon*, eds. S. S. Iyer, R. T. Collins, L. T. Canham

3.146 H. Münder, M. G. Berger, H. Lüth, U. Rossow, U. Frotscher, W. Richter, M. Ligeon, R. Herino: Appl. Surf. Sci. **63**, 57 (1993)

3.147 C. Pickering, M. I. J. Beale, D. J. Robbins, P. J. Pearson, R. Greef: J. Phys. **C17**, 6535 (1984)

3.148 H. Münder, M. G. Berger, U. Rossow, U. Frotscher, W. Richter, R. Herino, M. Ligeon: Appl. Surf. Sci. **63**, 57 (1993)

3.149 U. Rossow, H. Münder, M. Thönissen, W. Theiß: J. of Luminescence **57**, 205 (1993)

3.150 P. Roca i Cabarrocas, Satyendra Kumar, B. Drevillon: J. Appl. Phys. **66**, 3236 (1989)

3.151 V. Chu, M. Fang, B. Drevillon: J. Appl. Phys. **69**, 3363 (1991)

3.152 E. A. Irene: Thin Solid Films **233**, 96 (1993)

3.153 E. D. Palik, V. M. Bermudez, O. J. Glembocki: J. Electrochem. Soc. **132**, 871 (1985)

3.154 Y. Demay, D. Arnoult, J. P. Gailliard, P. Medina: J. Vac. Sci. Technol. **A5**, 3139 (1987)

3.155 Y. Demay, J. P. Gailliard, P. Medina: J. Cryst. Growth **81**, 97 (1987)

3.156 G. Laurence, F. Hottier, J. Hallais: J. Cryst. Growth **55**, 198 (1981)

3.157 D. E. Aspnes, W. E. Quinn, M. C. Tamargo, M. A. A. Pudensi, S. A. Schwarz, M. J. S. P. Brasil, R. E. Nahory, S. Gregory: Appl. Phys. Lett. **60**, 1244 (1992)

3.158 R. I. G. Uhrberg, R. D. Bringans, M. A. Olmstead, R. Z. Bachrach, J. E. Northrup: Phys. Rev. **B35**, 3945 (1987)

3.159 S. P. Kowalczyk, D. L. Miller, J. R. Waldrop, P. G. Newman, R. W. Grant: J. Vac. Sci. Technol. **19**, 255 (1981)

3.160 P. Etienne, P. Alnot, J. F. Rochette, J. Massies: J. Vac. Sci. Technol. **B4**, 1301 (1986)

3.161 R. W. Bernstein, A. Borg, H. Husby, B.-O. Fimland, A. P. Grande, J. K. Grepstadt: Appl. Surf. Sci. **56-58**, 74 (1992)

3.162 U. Resch, N. Esser, I. Raptis, J. Waßerfall, A. Förster, D. I. Westwood, W. Richter: Surf. Sci. **269/270**, 797 (1992)

3.163 H. Wilhelm, W. Richter, U. Rossow, D. R. T. Zahn, D. A. Woolf, D. I. Westwood, R. H. Williams: Surf. Sci. **251/252**, 556 (1991)

3.164 R. I. G. Uhrberg, R. D. Bringans, M. A. Olmstead, R. Z. Bachrach: Phys. Rev. **B35**, 3945 (1987)

3.165 D. A. Woolf UWC Cardiff, A. Förster KFA Jülich: private communication

3.166 T. H. Shen, C. C. Matthai: Surf. Sci. **287/288**, 672 (1993)

3.167 S. A. Alterowitz, P. G. Snyder, K. G. Merkel, J. A. Woollam, D. C. Radulescu, L. F. Eastman: J. Appl. Phys. **63**, 5081 (1988)

3.168 J. L. Freeouf: Appl. Phys. Lett. **53**, 2426 (1988)

3.169 M. Erman, C. Alibert, J. B. Theeten, P. Frijlink, B. Catte: J. Appl. Phys. **63**, 465 (1988)

3.170 M. Erman, Doctorat d'Etat thesis, University Pierre and Marie Curie, Paris, 1986

3.171 P. Apell, O. Hunderi: Optical Properties of Superlattices, in *Handbook of Optical Constants of Solids* II (Academic Press 1990)

3.172 K. Vedam, P. J. McMarr, J. Narayan: Appl. Phys. Lett. **47**, 339 (1985)

3.173 K. Vedam, S. So: Surf. Sci. **29**, 379 (1972)

3.174 J. A. Woollam, B. Johs, W. A. McGahan, P. G. Snyder, J. Hale, H. W. Yao: MRS Symp. Proc. **324**, 15 (1994)

3.175 J . C. C. Fan, J. M. Poate (eds.), *Heteroepitaxy on Silicon*, MRS Symp. Proc. **67**; J. C. C. Fan, J. M. Phillips, B. Y. Tsaur (eds.), *Heteroepitaxy on Silicon II*, MRS Symp. Proc. **91**

3.176 D. E. Aspnes: J. Opt. Soc. Am. **A10**, 976 (1993)

3.177 F. H. P. M. Habraken, O. L. J. Gijzeman, G. A. Bootsma: Surf. Sci. **96**, 482 (1980)

3.178 D. E. Aspnes: J. Vac. Sci. Techn. **B3**, 1498 (1985)

3.179 P. Etchegoin, M. Cardona: Thin Solid Films **233**, 137 (1993)

3.180 U. Resch-Esser, N. Blick, N. Esser, Th. Werninghaus, U. Rossow, W. Richter: Proc. of the ICFSI-4 Jülich, 14-18 June 1993, p. 321

eds. B. Lengeler, H. Lüth, W. Mönch, J. Pollmann, World Scientific Press, Singapore, New Jersey, London, Hong Kong 1994

3.181 U. Rossow, Ph.D. Thesis, TU Berlin 1993

4.1 W. Hayes, R. Loudon: *Light Scattering in Solids*, (J. Wiley and Sons, New York 1978)

4.2 W. Richter: in *Springer Tracts in Modern Physics* **78**, Resonant Raman Scattering in Semiconductors, ed. by G. Höhler, (Springer, Berlin, Heidelberg, New York 1976)

4.3 M. Cardona: in *Topics in Applied Physics* **50**, Light Scattering in Solids II, ed. by M. Cardona and G. Güntherodt, (Springer, Berlin, Heidelberg, New York 1982), p. 19

4.4 G. Abstreiter, M. Cardona, A. Pinczuk: in *Topics in Applied Physics* **54**, Light Scattering in Solids IV, ed. by M. Cardona and G. Güntherodt, (Springer, Berlin, Heidelberg, New York 1984), p. 5

4.5 B. Jusserand, M. Cardona: in *Topics in Applied Physics* **66**, Light Scattering in Solids V, ed. by M. Cardona and G. Güntherodt, (Springer, Berlin, Heidelberg, New York 1989) p. 49

4.6 J. Sapriel, B. Djafari Rouhani: Surf. Science Rep. **10**, 189 (1989)

4.7 R. Loudon: Proc. Royal Soc. **A275**, 218 (1963)

4.8 A. Pinczuk, E. Burstein: in *Topics in Applied Physics* **8**, Light Scattering in Solids, ed. by M. Cardona and G. Güntherodt, (Springer, Berlin, Heidelberg, New York 1975), p. 23

4.9 E. O. Kane: Phys. Rev. **178**, 1368 (1969)

4.10 M. Born, K. Huang: *Dynamical Theory of Crystal Lattices*, (Oxford: Clarendon Press, 1954)

4.11 P. Brüesch: in *Springer Series in Solid-State Sciences* **34**, Phonons: Theory and Experiments I, ed. by M. Cardona, P. Fulde, H. J. Queisser (Springer, Berlin, Heidelberg, New York 1982), p. 117

4.12 H. Fröhlich: Adv. Phys. **3**, 325 (1954)

4.13 G. F. Koster, J. O. Dimmock, R. G. Wheeler, H. Statz: *Properties of the thirtytwo point groups*, (M.I.T. Press, Cambridge (Mass.) 1963)

4.14 R. Loudon: Adv. Phys. **13**, 423 (1964)

4.15 E. Hecht, A. Zajac: *Optics* (Addison-Wesley Publ. Comp. 1974)

4.16 R. K. Chang, M. B. Long: in [4.3], p. 179

4.17 J. C. Tsang: in *Topics in Applied Physics* **66**, Light Scattering in Solids V, ed. by M. Cardona and G. Güntherodt, Springer, Berlin, Heidelberg, New York (1989) p. 233

4.18 R. B. Bilhorn, J. V. Sweedler, P. M. Epperson, M. B. Denton: Appl. Spectroscopy **41**, 1114 (1987)

4.19 A. Krost, W. Richter and D. R. T. Zahn: Appl. Surf. Science, **56–58**, 691 (1992)

4.20 V. Wagner, D. Drews, N. Esser, D. R. T. Zahn, J. Geurts, W. Richter: J. of Appl. Phys. **75**, 7330 (1994)

4.21 D. W. Pohl, W. Denk, M. Lanz: Appl. Phys. Lett. **44**, 651 (1984)

4.22 E. L. Buckland, P. J. Moyer, M. A. Paesler: J. Appl. Phys. **73**, 1018 (1993)

4.23 H. F. Hess, E. Betzig, T. D. Harris, L. N. Pfeiffer, K. West: Science **264**, 1740 (1994)

4.24 M. Cardona, L. Ley: in *Topics in Applied Physics* **26**, Photoemission in Solids, ed. by M. Cardona and L. Ley, (Springer, Berlin, Heidelberg, New York 1978), p. 1

4.25 Y. Shirakawa, H. Kukimoto: J. Appl. Phys. **51**, 2014 (1980)

4.26 M. Aven, D. T. F. Marple, B. Segall: J. Appl. Phys. Suppl. **32**, 2261 (1961)

4.27 D. J. Olego, K. Shahzad, J. Petruzzello, D. Cammack: Phys. Rev. **B36**, 7674 (1987)

4.28 M. A. Chesters: Reflection-Absorption Infrared Spectroscopy of Adsorbates on Metal Surfaces, in *Analytical Applications of Spectroscopy*, ed. C. S. Creaser, A. M. C. Davies, Royal Society of Chemistry, London (1988)

4.29 P. Skeath, C. Y. Su, W. A. Harrison, I. Lindau, W. Spicer: Phys. Rev. **B27**, 6246 (1983)

4.30 F. Schäffler, R. Ludeke, A. Taleb-Ibrahimi, G. Hughes, D. Rieger: J. Vac. Sci. Technol. **B5**, 1048 (1987)

4.31 R. D. Bringans: Critical Reviews in Solid State and Material Sciences **17**, 353 (1992)

4.32 W. Richter, N. Esser, A. Kelnberger, M. Köpp: Solid State Commun. **84**, 165 (1992)

4.33 M. Hünermann, J. Geurts, W. Richter: Phys. Rev. Lett. **66**, 640 (1991)

4.34 H. Wilhelm, W. Richter, U. Rossow, D. R. T. Zahn, D. A. Woolf, D. I. Westwood, R. H. Williams: Surface Science **251/252**, 556 (1991)

4.35 R. B. Doak, D. B. Nguyen: Phys. Rev. **B41**, 3578 (1989)

4.36 N. Esser, M. Köpp, P. Haier, W. Richter: Journal of Electron Spectroscopy and Related Phenomena **64/65**, 85 (1993)

4.37 A. V. Nurmikko, R. L. Gunshor, L. A. Kolodziejski: IEEE J. Quantum Electr. **QE-22** 1785 (1986)

4.38 C. B. Duke, A. Paton, W. K. Ford, A. Kahn, J. Carelli: Phys. Rev. **B26**, 803 (1982)

4.39 C. Mailhiot, C. B. Duke, D. J. Chadi: Phys. Rev. **B31**, 2213 (1985)

4.40 P. Martensson, G. V. Hansson, M. Lähdeniemi, K. O. Magnusson, S. Wiklund, J. M. Nicholls: Phys. Rev. **B33**, 7399 (1986)

4.41 P. Martensson, R. M. Feenstra: Phys. Rev. **B39**, 7744 (1989)

4.42 M. Hünermann: Ph.D. Thesis, RWTH Aachen, 1991

4.43 N. Esser, M. Reckzügel, R. Srama, U. Resch, D. R. T. Zahn, W. Richter, C. Stephens, M. Hünermann: J. Vac. Sci. Technol. **B8**, 680 (1990)

4.44 N. Esser: Ph.D. Thesis (Berlin University of Technology, 1991)

4.45 W. Pletschen, N. Esser, H. Münder, D. Zahn, J. Geurts, W. Richter: Surf. Science **178**, 140 (1986)

4.46 M. Hünermann, W. Pletschen, U. Resch, U. Rettweiler, W. Richter, J. Geurts, P. Lautenschlager: Surf. Science **189/190**, 322 (1987)

4.47 J. S. Lannin: Phys. Rev. **B15**, 3863 (1977)

4.48 R. N. Zitter: in *The Physics of Semimetals and Narrow-Gap Semiconductors*, ed. by E. L. Carter, R. T. Bate (Pergamon Press, Oxford 1971), p. 285

4.49 R. I. Sharp, E. Warming: J. Phys. **F1**, 570 (1971)

4.50 U. Resch, N. Esser, W. Richter: Surf. Science **251/252**, 621 (1991)

4.51 N. Esser, M. Hünermann, U. Resch, D. Spaltmann, J. Geurts, D. R. T. Zahn, W. Richter, R. H. Williams: Appl. Surf. Science **41/42**, 169 (1989)

4.52 A. B. McLean, R. M. Feenstra, A. Taleb-Ibrahimi, R. Ludeke: Phys. Rev. **B39**, 12925 (1989)

4.53 T. Guo, R. E. Atkinson, W. K. Ford: Phys. Rev. **B41**, 5138 (1990)

4.54 A. G. Milnes, D. L. Feucht: *Heterojunctions and Metal-Semiconductor Junctions* (Academic Press, New York 1972)

4.55 R. Trommer, M. Cardona: Phys. Rev. **B 17**, 1865 (1978)

4.56 M. Sinyukov, R. Trommer, M. Cardona: Phys. Stat. Sol. (b) **86**, 563 (1978)

4.57 A. Compaan, H. J. Trodahl, Phys. Rev. **B 29**, 793 (1984)

4.58 N. Esser, M. Köpp, P. Haier, W. Richter, J. Electron. Spectrosc. **64/65**, 85 (1993)

4.59 N. Esser, R. Hunger, J. Rumberg, W. Richter, R. Del Sole, A. I. Shkrebtii, Surf. Sci. **307–309**, 1045 (1994)

4.60 W. Mönch, H. Gant: Phys. Rev. Lett. **48**, 512 (1982)

4.61 R. Merlin, A. Pinczuk, W. T. Beard, C. E. E. Wood: J. Vac. Sci. Technol. **21**, 516 (1982)

4.62 H. Brugger, F. Schäffler, G. Abstreiter: Phys. Rev. Lett. **52**, 141 (1984)

4.63 J. G. Brugger: Ph.D. Thesis, (Munich University of Technology, 1987)

4.64 D. R. T. Zahn, Ch. Maierhofer, A. Winter, M. Reckzügel, R. Srama, U. Rossow, A. Thomas, K. Horn, W. Richter: Appl. Surf. Sci. **56-58**, 684 (1992)

4.65 Ch. Maierhofer: Ph.D. Thesis (Technical University of Berlin, 1992)

4.66 K. J. Chang, S. Froyen, M. L. Cohen: Phys. Rev. **B 28**, 4736 (1983)

4.67 *Proc. of the II-VI-Conference Newport 1993*, J. Crystal Growth **138** (1994)

4.68 F. H. Pollak: in *Analytical Raman Spectroscopy*, ed. by J. G. Grasseli and B. J. Bulkin, Chemical Analysis Series, Vol. **114** (1991)

4.69 C. W. Snyder, B. G. Orr, D. Kessler, L. M. Sander: Phys. Rev. Lett. **66** 3032 (1991)

4.70 H. J. van der Merwe: Surf. Science **31**, 198 (1972)

4.71 W. Matthews, A. E. Blakeslee: J. Cryst. Growth **29**, 273 (1975)

4.72 R. People, IEEE J. Quantum Elekctron. **QE-22**,1696 (1986)

4.73 J. F. Nye: *Physical Properties of Crystals, Their Representation by Tensors and Matrices* (Clarendon Press, Oxford 1957)

4.74 E. Anastassakis: in *Physical Problems in Microelectronics*, Proceedings 4th Int. School ISSPPME, Varna (Bulgaria), ed. by J. Kassabov (World Scientific, Singapore (1985), p. 128

4.75 E. Anastassakis: J. Appl. Phys. **68**, 4561 (1990)

4.76 Landolt-Börnstein: *Numerical Data and Functional Relationships in Science and Technology, New. Series, Group III*, Vol. 17a, ed. O. Madelung, (Springer, Berlin, Heidelberg, New York, Tokyo 1983)

4.77 G. Landa, R. Carles, C. Fontaine, E. Bedel, A. Munoz-Yagüe: J. Appl. Phys. **66**, 196 (1988)

4.78 T. Nishioka, Y. Shinoda, Y. Ohmachi: J. Appl. Phys. **57**, 276 (1985)

4.79 K. Brunner, G. Abstreiter, B. O. Kolbesen, H. W. Meul: Appl. Surf. Sci. **39**, 116 (1989)

4.80 G. Abstreiter: Appl. Surf. Sci. **50**, 73 (1991)

4.81 A. Krost, W. Richter, O. Brafman: Appl. Phys. Lett. **56**, 343 (1990)

4.82 O. Brafman, A. Krost, W. Richter: J. Phys. : Condens. Matter **3**, 6203 (1991)

4.83 F. Cerdeira, C. J. Buchenauer, F. H. Pollak, M. Cardona, Phys. Rev. **B 5**, 580 (1972)

4.84 J. C. Tsang, F. H. Dacol, P. Mooney, J. O. Chu, B. S. Meyerson: Appl. Phys. Lett. **62**, 1146 (1993)

4.85 C. Fontaine, H. Benarfa, E. Bedel, A. Munoz-Yague, G. Landa, R. Carles: J. Appl. Phys. **60**, 208 (1986)

4.86 V. Wagner, J. Geurts, M. Eube, J. Woitok: Proc. of the Int. Conf. on Semicond. Interf. 7, Jülich (1993), *Formation of Semicoductor Interfaces*, ed. B. Lengeler, H. Lüth, W. Mönch, J. Pollmann (World Scientific, Singapore 1994), p. 550

4.87 J. Woitok, Ph.D. Thesis, RWTH Aachen (1989)

4.88 R. Beserman, C. Hirlimann, M. Balkanski: Solid State Commun. **20**, 485 (1976)

4.89 B. Jusserand, S. Slempkes: Solid State Commun. **44**, 95 (1984)

4.90 S. Emura, S. Gonda, Y. Matsui, Hayashi: Phys. Rev. **B38**, 3280 (1988)

4.91 X. Wang, X. Zhang: Solid State Commun. **59**, 869 (1986)

4.92 M. A. Renucci, J. B. Renucci, M. Cardona: in *Proc. 2nd Int. Conf. on Light Scattering in Solids*, ed. M. Balkanski (Flammarion, Paris 1971), p. 326

4.93 J. Finders, J. Geurts, A. Kohl, M. Weyers, B. Opitz, O. Kayser, P. Balk: J. Crystal Growth **107**, 151 (1991)

4.94 J. C. Tsang, F. H. Dacol, P. M. Mooney, J. O. Chu, B. S. Meyerson: Appl. Phys. Lett. **62** 1146 (1993)

4.95 P. M. Mooney, F. H. Dacol, J. C. Tsang, J. O. Chu: Appl. Phys. Lett. **62** 2069 (1993)

4.96 R. Schorer, E. Friess, K. Eberl, G. Abstreiter: Phys. Rev. **B44**, 1772 (1991)

4.97 A. Gomyo, T. Suzuki, S. Iijima: Phys. Rev. Lett. **60**, 2645 (1988)

4.98 A. Gomyo, K. Kobayashi, S. Kawata, I. Hino, T. Suzuki: J. Crystal Growth **77**, 367 (1986)

4.99 A. Mascarenhas, S. Kurtz, A. Kibbler, J. M. Olson: Phys. Rev. Lett. **63**, 2108 (1989)

4.100 J. Geurts, J. Finders, O. Kayser, B. Opitz, M. Maassen, R. Westphalen, P. Balk: SPIE Conference Proceedings **1361**, 744 (1991)

4.101 A. Krost, N. Esser, H. Selber, J. Christen, W. Richter, D. Bimberg, L. C. Su, G. B. Stringfellow: J. Vac. Sci. Technol. **B12**, 2558 (1994)

4.102 A. Mascarenhas, S. R. Kurtz, A. Kibbler, J. M. Olson: Phys. Rev. Lett. **63**, 2108 (1989)

4.103 J. C. Tsang, Y. Yokota, R. Matz, G. W. Rubloff: Appl. Phys. Lett. **44**, 430 (1984)

4.104 R. J. Nemanich, R. T. Fulks. , B. L. Stafford, H. A. Vander Plas: Appl. Phys. Lett. **46**, 670 (1985)

4.105 A. Krost, W. Richter, D. R. T. Zahn, K. Hingerl, H. Sitter: Appl. Phys. Lett. **57**, 1981 (1990)

4.106 D. R. T. Zahn, W. Richter, T. Eickhoff, J. Geurts, T. D. Golding, J. H. Dinan, K. J. MacKey, R. H. Williams: Applied Surface Science **41/42**, 497 (1989)

4.107 K. J. MacKey, P. M. G. Allen, W. G. Herrenden-Harker, R. H. Williams: Surf. Sci. **178**, 7 (1986)

4.108 G. P. Schwartz, B. Schwartz, D. Distefano, G. J. Gualtieri, J. E. Griffiths: Appl. Phys. Lett. **34**, 205 (1979)

4.109 R. L. Farrow, R. K. Chang, S. Mroczkowski: Appl. Phys. Lett. **31**, 768 (1977)

4.110 R. L. Farrow, R. K. Chang, S. Mroczkowski, F. H. Pollak: Appl. Phys. Lett. **31**, 768 (1977)

4.111 D. Drews, M. Langer, W. Richter, D. R. T. Zahn: Proc. of the Int. Conf. on Semicond. Interf. 7, Jülich (1993), *Formation of Semicoductor Interfaces*, ed. B. Lengeler, H. Lüth, W. Mönch, J. Pollmann (World Scientific, Singapore 1994), p. 506

4.112 V. Wagner, D. Drews, N. Esser, W. Richter, D. R. T. Zahn, J. Geurts, W. Richter: Proc. of the Int. Conf. on Semicond. Interf. 7, Jülich (1993), *Formation of Semicoductor Interfaces*, ed. B. Lengeler, H. Lüth, W. Mönch, J. Pollmann (World Scientific, Singapore 1994), p. 546

4.113 M. V. Klein: IEEE J. QE-**22**, 1760 (1986)

4.114 B. Jusserand, D. Paquet: in *Semiconductor Heterojunctions and Superlattices*, ed. by G. Allan, G. Bastard, N. Boccara, M. Lannoo, M. Voos, (Springer, Berlin, Heidelberg 1986), p. 108

4.115 M. Cardona: in *Lectures of Surface Science*, ed. by G. R. Castro, M. Cardona, (Springer, Berlin, Heidelberg, New York 1987), p. 2

4.116 R. Enderlein, D. Suisky, J. Röseler, Phys. Stat. Sol. (b) **165**, 9 (1991)

4.117 A. Fasolino, E. Molinari: Surf. Science **228**, 112 (1990)

4.118 B. Jusserand, F. Alexandre, D. Paquet, G. Le Roux: Appl. Phys. Lett. **47**, 301 (1986)

4.119 J. Geurts et al., Phys. Stat. Sol. (a) **152** (1995)

4.120 J. Finders, J. Geurts, Y. Pusep (to be published)

4.121 D. J. Olego, K. Shahzad, D. A. Cammack, H. Cornelissen: Phys. Rev. **38**, 5554 (1988)

4.122 M. K. Jackson, R. H. Miles, T. C. McGill, J. P. Faurie: Appl. Phys. Lett. **55**, 786 (1989)

4.123 R. Merlin, C. Colvard, M. V. Klein, H. Morkoc, A. Y. Cho, A. C. Gossard: Appl. Phys. Lett. **36**, 43 (1980)

4.124 A. K. Sood, J. Menendez, M. Cardona, K. Ploog, Phys. Rev. Lett. **54**, 2111 (1985)

4.125 R. E. Camley, D. L. Mills: Phys. Rev. **29**, 1695 (1984)

4.126 Akhilesh K. Arora, A. K. Ramdas, M. R. Melloch, N. Otsuka: Phys. Rev. **B36**, 1021 (1987)

4.127 M. V. Klein: in *Light Scattering in Solids*, ed. M. Cardona (Springer, Heidelberg 1975)

4.128 J. Wagner, M. Ramsteiner, H. Seelewind, J. Clarc: J. Appl. Phys. **64**, 802 (1988)

4.129 D. J. Olego, T. Marshall, J. Gaines, and K. Shahzad: Phys. Rev. **B42**, 9067 (1990)

4.130 D. J. Olego, T. Marshall, D. Cammack, K. Shahzad, and J. Petruzzello: Appl. Phys. Lett. **58**, 2654 (1991)

4.131 D. J. Olego, J. Petruzello, T. Marshall, and D. Cammack: Appl. Phys. Lett. **59**, 961 (1991)

4.132 A. A. Gogolin, E. I. Rashba: Solid State Commun. **19**, 1177 (1976)

4.133 A. A. Gogolin, E. I. Rashba: in *Proc. 13th Int. Conf. on the Physics of Semiconductors*, ed. by F. G. Fumi (Tipografia Marves, Rome, 1976), p. 231

4.134 R. Trommer: Ph.D. Thesis, University of Stuttgart, 1977

4.135 D. E. Aspnes: in *Handbook on Semiconductors* **Vol. 2**, ed. M. Balkanski (North Holland Publishing Company 1980)

4.136 J. Menendez, M. Cardona: Phys. Rev. **B31**, 3696 (1985)

4.137 A. Pinczuk, G. Abstreiter: in *Light Scattering in Solids V*, ed. M. Cardona and G. Güntherodt (Springer, Berlin)

4.138 B. B. Varga: Phys. Rev. **A137**, 1896 (1965)

4.139 E. Burstein, A. Pinczuk, S. Iwasa: Phys. Rev. **157**, 611 (1967)

4.140 P. Grosse: *Freie Elektronen in Festkörpern*, (Springer, Berlin, Heidelberg, New York 1979)

4.141 W. Richter, U. Nowak, A. Stahl: Proc. 15th Int. Conf. Physics of Semiconductors, Kyoto, 1980, J. Phys. Soc. Japan **49**, Suppl. A, 703 (1980)

4.142 E. Burstein, A. Pinczuk, S. Buchner: in *Physics of Semiconductors 1978*, ed. by B. L. H. Wilson, The Institute of Physics, London (1979), p. 1231

4.143 U. Nowak, W. Richter, G. Sachs: Phys. stat. sol. (b) **108**, 131 (1981)

4.144 W. Richter, U. Nowak, H. Jürgensen, U. Rössler: Solid State Commun. **67**, 199 (1988)

4.145 B. Boudart, B. Prévot, C. Schwab, Appl. Surf. Sci. **50**, 295 (1991)

4.146 U. Resch, N. Esser, Y. S. Raptis, W. Richter, J. Wasserfall, A. Förster, D. I. Westwood: Surf. Sci. **269/270**, 797 (1992)

4.147 A. Mooradian, A. L. McWhorter: Phys. Rev. Lett. **19**, 849 (1967)

4.148 A. Pinczuk, S. Schmitt-Rink, G. Danan, J. P. Valladares, L. N. Pfeiffer, K. W. West: Phys. Rev. Lett. **63**, 1633 (1989)

4.149 J. M. Worlock. (ed.): *Proc. 7th Conf. Electronic Properties of Two Dimensional Systems*, Surface Sci. **196** (1988)

4.150 T. Ando, A. B. Fowler, F. Stern: Rev. Mod. Phys. **54**, 437 (1982)

4.151 J. Wagner: *Proc. of the SPIE* **1678**, New Jersey (1992), p. 110

4.152 D. Olego, A. Pinczuk, A. C. Gossard, W. Wiegmann: Phys. Rev. **B25**, 7867 (1982)

4.153 A. Nurmikko, A. Pinczuk: in Physics Today **6**, 24 (1993)

4.154 G. Y. Robinson: in *Physics and Chemistry of III-V Semiconductor Interfaces*, ed. C. F. Wilmsen, (Plenum Press, New York 1985), p. 73

4.155 W. Mönch: in *Advances in Solid State Physics*, **XXVI**, ed. P. Grosse (Vieweg, Braunschweig 1986), p. 67

4.156 E. H. Rhoderick, R. H. Williams: *Metal Semiconductor Contacts* (Clarendon, Oxford 1988)

4.157 W. Mönch: Rep. Prog. Phys. **53**, 221 (1990)

4.158 W. Mönch: *Semiconductor Surfaces and Interfaces* (Springer, Berlin, Heidelberg, New York 1993)

4.159 W. Schottky: Zeitschrift f. Physik **118**, 539 (1942)

4.160 L. Ley, M. Cardona, F. H. Pollak: in *Topics in Applied Physics* **27**, Photoemission in Solids II, ed. by M. Cardona and L. Ley (Springer, Berlin, Heidelberg, New York 1978), p. 11

4.161 F. Schäffler, G. Abstreiter: Phys. Rev. B **34** 4017 (1986)

4.162 A. Pinczuk, A. A. Ballman, R. E. Nahory, M. A. Pollack, J. M. Worlock: J. Vac. Sci. Technol. **16** 1168 (1979)

4.163 L. A. Farrow, C. J. Sandroff, M. C. Tamargo: Appl. Phys. Lett. **51**, 1931 (1987)

4.164 R. E. Viturro, J. L. Shaw, C. Mailhiot, L. J. Brillson, N. Tache, J. McKinley, G. Margaritondo, J. M. Woodall, R. D. Kirchner, G. D. Petit, S. L. Wright: Appl. Phys. Lett. **52**, 2052 (1988)
4.165 G. P. Schwartz, G. J. Gualtieri: J. Electrochem. Soc. **133**, 1266 (1986)
4.166 D. J. Olego: J. Vac. Sci. Technol. **B6**, 1193 (1988)
4.167 E. T. Yu, T. C. McGill: Appl. Phys. Lett. **53**, 60 (1988)
4.168 D. J. Olego: Appl. Phys. Lett. **51**, 1422 (1987)
4.169 D. J. Olego: Phys. Rev. **B39**, 12743 (1989)
4.170 W. Franz: Z. Naturforsch. **13a**, 484 (1958)
4.171 L. V. Keldysh: Soviet Phys. JETP **34**, 788 (1958)
4.172 J. G. Gay, J. D. Dow, E. Burstein, A. Pinczuk: in *Light Scattering in Solids*, ed. by M. Balkanski (Flammarion, Paris 1971), p. 33
4.173 W. Richter, R. Zeyher, M. Cardona: Phys. Rev. **B18**, 4312 (1978)
4.174 W. R. Pletschen: Ph.D. Thesis (RWTH Aachen, 1986)
4.175 A. Huijser, J. van Laar, T. L. van Rooy: Surf. Sci. **62**, 472 (1977)
4.176 G. M. Guichard, C. A. Sebenne, C. D. Thualt: J. Vac. Sci. Technol. **16**, 1212 (1979)
4.177 L. J. Brillson, E. Burstein: Phys. Rev. Lett. **27**, 808 (1971)
4.178 H. J. Stolz, G. Abstreiter: J. Vac. Sci. Technol. **19**, 380 (1981)
4.179 M. Mattern-Klosson, H. Lüth: Solid State Commun. **56**, 1001 (1985)
4.180 R. H. Williams, D. R. T. Zahn, N. Esser, W. Richter: J. Vac. Sci. Technol. **B7**, 997 (1989)
4.181 T. Kendelewicz, K. Miyano, R. Cao, J. C. Woicik, I. Lindau, W. E. Spicer: Surf. Sci. **220**, L726 (1989)
4.182 F. Schäffler, R. Ludeke, A. Taleb-Ibrahimi, G. Hughes, D. Rieger: Phys. Rev. **B36**, 1328 (1987)
4.183 G. Annovi, M. -G. Betti, U. del Pennino, C. Mariani: Phys. Rev. **B41**, 11978 (1990)
4.184 C. K. Shih, R. M. Feenstra, P. Martensson: J. Vac. Sci. Technol. **A8**, 3379 (1990)
4.185 A. Kumar, O. P. Katyal: J. Mater. Sci. **24**, 4037 (1989)
4.186 H. Brugger, G. Abstreiter: in *Semiconductor Quantum Well structures and Superlattices*, ed. by K. Ploog and N. T. Linh (Editions de Physique, Les Ulis (1985), p. 209
4.187 H. J. Stolz, G. Abstreiter: J. Phys. Soc. Jpn. **49** Suppl. A, 1101 (1980)
4.188 K. Smit, L. Koenders, W. Mönch: J. Vac. Sci. Technol. **B7**, 888 (1989)
4.189 T. U. Kampen, D. Troost, X. Y. Hou, L. Koenders, W. Mönch: J. Vac. Sci. Technol. **B9**, 2095 (1991)
4.190 C. Trallero-Giner, A. Cantarero, M. Cardona, M. Mora: Phys. Rev. **B 45**, 6601 (1992)
4.191 M. Ramsteiner, J. Wagner, P. Hiesinger, K. Köhler, U. Rössler: J. Appl. Phys. **73**, 5023 (1993)
4.192 J. Geurts: Surf. Sci. Rep. **18**, 1 (1993)
5.1 R. J. Bell: *Introduction to Fourier Transform Spectroscopy* (Academic Press, New York 1972)
5.2 P. R. Griffiths, J. A. de Haseth: *Fourier Transform Infrared Spectrometry* (John Wiley & Sons, New York 1986)
5.3 R. Geick: *Topics in Current Chemistry* **58** (Springer, Berlin 1975), p. 73

5.4 A. G. Marshall, F. R. Verdun: *Fourier Transforms in NMR, Optical, and Mass Spectrometry* (Elsevier, Amsterdam 1990)
5.5 P. Appel, O. Hunderi: in *Optical Properties of Superlattices*, ed. E. D. Palik, Academic Press (Boston, 1991), p. 97
5.6 T. Dumelow, T. J. Parker, S. R. P. Smith, D. R. Tilley, Surface Science Reports **17**, 151 (1993)
5.7 L. D. Landau, E. M. Lifshitz: *Electrodynamics of Continuous Media* (Pergamon, Oxford 1960)
5.8 E. E. Bell: *Encyclopedia of Physics* **XXV/2** ed. by L. Genzel, (Springer, Berlin 1967), p. 1
5.9 J. D. Jackson: *Classical Electrodynamics*, (John Wiley, New York 1975)
5.10 D. Palik: *Handbook of Optical Constants of Solids* II (New York, Academic 1991)
5.11 H. A. Kramers: Estratto dagli Atti del Congresso Internazionale, de Fisici Como **2**, 545 (1927)
5.12 R. de L. Kronig: J. Opt. Soc. Am. **12**, 547 (1926)
5.13 P. Grosse, V. Offermann: Appl. Phys. **A52**, 138 (1991)
5.14 M. G. Sceats, G. C. Morris: Phys. Stat. Sol. (a) **14**, 643 (1972)
5.15 C. W. Peterson, B. W. Knight: J. Opt. Soc. Am. **63**, 1238 (1973)
5.16 B. Harbecke: Appl. Phys. **A40**, 154 (1986)
5.17 B. Harbecke: Appl. Phys. **B39**, 165 (1986)
5.18 Z. Knittel: *Optics of Thin Films* (John Wiley, London 1976)
5.19 P. Grosse: *Freie Elektronen in Festkörpern* (Springer, Berlin 1979)
5.20 A. F. Terzis, X. C. Liu, A. Petrou, B. D. McCombe, M. Dutta, H. Shen, D. D. Smith, M. W. Cole, M. Maysing-Lara, P. G. Newman: J. Appl. Phys. **67**, 2501 (1990)
5.21 D. W. Berreman: Phys. Rev. **130**, 2193 (1963)
5.22 D. W. Berreman: Proc. Intern. Conf. Lattice Dynamics Copenhagen, ed. by R. F. Wallis (Pergamon, Oxford 1963), p. 397
5.23 B. Harbecke, B. Heinz, P. Grosse: Appl. Phys. **A38**, 263 (1985)
5.24 R. Brendel: Appl. Phys. **A50**, 587 (1990)
5.25 M. A. Chesters: in *Analytical Applications of Spectroscopy*, ed. by C. S. Creaser, A. M. C. Davies (Roy. Soc. of Chemistry, London 1988)
5.26 N. J. Harrick: *Internal Reflection Spectroscopy* (Wiley, New York 1967), p. 138
5.27 E. Kretschmann: Z. Physik **241**, 313 (1971)
5.28 A. Otto: Z. Physik **216**, 398 (1968)
5.29 V. M. Agranovich, D. L. Mills (ed.), *Surface Polaritons* (North-Holland, Amsterdam 1982)
5.30 N. Wiener: Act. Math. Stockholm **55**, 117 (1930)
5.31 A. Khintchine: Math. Ann. **109**, 604 (1934)
5.32 J. D. Saalmüller: Ph.D. Thesis, RWTH Aachen (1987)
5.33 K. Krishnan, P. J. Stout, M. Watanabe: *Practical Fourier Transform Infrared Spectroscopy*, ed. by J. R. Ferraro, K. Krishnan, (Academic Press, San Diego 1990), p. 286
5.34 H. R. Chandrasekhar, A. K. Ramdas: Phys. Rev. **B21**, 1511 (1980)
5.35 U. Kreibig, C. v. Fragstein: Z. Physik **224**, 307 (1969)

5.36 A. Petrou, B. D. McCombe: in *Landau Level Spectroscopy*, ed. by G. Landwehr, E. I. Rashba (Elsevier Science Publisher, Amsterdam, 1990), p. 679

5.37 T. Duffield, R. Bhat, M. Koza, D. De Rosa, D. M. Hwang, P. Grabbe, S. J. Allen: Phys. Rev. Lett. **56**, 2724 (1986)

5.38 T. Ando, A. B. Fowler, F. Stern: Rev. Mod. Phys. **54**, 437 (1982)

5.39 Special issue on QW's and superlattices: IEEE J. Quantum Electron. **QE 22** (1986),

5.40 Special issue on QW's and superlattices: IEEE J. Quantum Electron. **QE 24** (1988),

5.41 D. Heitmann: in *Physics and Applications of Quantum Wells and Superlattices*, ed. by E. E. Mendez, K. v. Klitzing, (Plenum Press, New York 1987), p. 317

5.42 D. Heitmann, T. Demel, P. Grambow, K. Ploog: in *Festkörperprobleme/Advances in Solid State Physics* **29**, ed. by U. Rössler, (Vieweg, Braunschweig 1989), p. 285

5.43 D. Heitmann, U. Mackens: Phys. Rev. **B33**, 8269 (1986)

5.44 E. Gornik: in *Landau Level Spectroscopy*, ed. by G. Landwehr, E. I. Rashba, (North Holland, Elsevier, Amsterdam, The Netherlands, 1991), p. 911

5.45 E. Batke: in *Festkörperprobleme/Advances in Solid State Physics* **31**, ed. by U. Rössler (Vieweg, Braunschweig 1992), p. 297

5.46 S. J. Allen Jr. , D. C. Tsui, B. Vinter: Solid State Commun. **20**, 425 (1976)

5.47 T. Ando: Solid State Commun. **21**, 133 (1977)

5.48 W. L. Bloss: J. Appl. Phys. **66**, 3639 (1989)

5.49 M. Helm: in *Intersubband Transitions in Quantum Wells*, ed. by E. Rosencher, (Plenum Press, New York 1992), p. 151

5.50 M. Helm, W. Hilber, T. Fromherz, F. M. Peeters, K. Alavi, R. N. Pathak: Phys. Rev. **B48**, 1601 (1993)

5.51 J. Faist, F. Capasso, D. L. Sivco, C. Sirtori, A. L. Hutchinson, A. Y. Cho: Science **264**, 553 (1994)

5.52 B. F. Levine: J. Appl. Phys. **74**, R1 (1993)

5.53 H. Hertle, G. Schuberth, E. Gornik, G. Abstreiter, F. Schäffler: Appl. Phys. Lett. **59**, 2977 (1991)

5.54 T. Fromherz, E. Koppensteiner, M. Helm, G. Bauer, J. Nützel, G. Abstreiter: Phys. Rev. **B50**, 15073 (1994)

5.55 T. Fromherz, E. Koppensteiner, M. Helm, G. Bauer, J. Nützel, G. Abstreiter: Phys. Rev. **B50**, 15073 (1994)

5.56 P. S. Zory: *Quantum Well Lasers* (Academic Press, Boston 1993)

5.57 S. Yuan, H. Krenn, G. Springholz, G. Bauer, M. Kriechbaum: Appl. Phys. Lett. **62**, 885 (1993)

5.58 S. Yuan, N. Frank, G. Bauer, M. Kriechbaum: Phys. Rev. **B50**, 5286 (1994)

5.59 M. M. Pradhan, R. K. Garg, M. Arora: Infrared Phys. **27**, 25 (1987)

5.60 A. S. Oates, W. Lin: J. Cryst. Growth **89**, 117 (1988)

5.61 F 123-91: ASTM - American Society for Testing and Materials, 1916 Race Street, Philadelphia, PA 19103-1187, USA

5.62 DIN 50 438, part 2 in DIN, Beuth Verlag GmbH, Berlin, Wien, Zürich (1982)

5.63 DIN 50 438, part 1 in DIN, Beuth Verlag GmbH, Berlin, Wien, Zürich (1990)

5.64 A. Baghdadi, N. M. Bullis, M. C. Croarkin, Y. Z. Li, R. I. Scace, R. W. Series, P. Stallhofer, M. Watanabe: J. Electrochem. Soc. **136**, 2015 (1989)

5.65 P. Wagner: Appl. Phys. A**53**, 20 (1991)

5.66 A. Borghesi, M. Geddo, B. Pivac: J. Appl. Phys. **69**, 7251 (1991)

5.67 M. Geddo, B. Pivac, A. Borghesi, A. Stella: Appl. Phys. Lett. **58**, 370 (1991)

5.68 A. V. Annapragada, F. F. Jensen, T. F. Kuech: J. Cryst. Growth **107**, 248 (1991)

5.69 A. K. Ramdas, S. Rodriguez: Rep. Prog. Phys. **44**, 1297 (1981)

5.70 F. Bassani, G. Pastore-Parravicini: *Eletronic States and Optical Transitions in Solids* (Pergamon Press,Oxford, 1975)

5.71 M. Altarelli, F. Bassani: in *Handbook of Semiconductors* Vol. 1, ed. by W. Paul, (North Holland, Amsterdam, 1980), p. 269

5.72 W. Zawadzki: in *Landau Level Spectroscopy*, ed. by G. Landwehr, E. I. Rashba, (North Holland-Elsevier, Amsterdam, 1991), p. 1305

5.73 B. O. Kolbesen: Appl. Phys. Lett. **27**, 353 (1975)

5.74 E. E. Haller, H. Navarro, F. Keilmann: Proc. Int. Conf. Phys. Semicond., Stockholm 1986 (World Scientific, Singapore 1987), p. 837

5.75 C. Jagannath, Z. W. Grabowski, A. K. Ramdas: Solid State Commun. **29**, 355 (1979)

5.76 G. Bastard: Phys. Rev. **B24**, 4714 (1981)

5.77 G. Bastard: *Wave Mechanics Applied to Heterostructures* (Editions de Physique, Les Ulis 1989)

5.78 C. Mailhiot, Yia-Chung Chang, T. C. McGill: Phys. Rev. **B26**, 4449 (1982)

5.79 R. Greene, K. K. Bajaj: Phys. Rev. **B31**, 913 (1985)

5.80 P. Lane, R. L. Greene: Phys. Rev. **B33**, 5871 (1986)

5.81 A. A. Reeder, J. M. Mercy, B. D. McCombe: IEEE J. Quant. Electron. , **QE24**, 1690 (1988)

5.82 T. W. Masselink, Y. C. Chang, M. Morkoc: Phys. Rev. **B28**, 7373 (1983)

5.83 T. W. Masselink, Y. C. Chang, M. Morkoc: Phys. Rev. **B32**, 5190 (1985)

5.84 L. T. Canham: Appl. Phys. Lett. **57**, 1046 (1990)

5.85 A. Halimaoui, C. Oules, G. Bomchil, A. Bsiesy, F. Gaspard, R. Herino, M. Ligeon, F. Muller: Appl. Phys. Lett. **59**, 304 (1991)

5.86 A. Gee: J. Electrochem. Soc. **107**, 787 (1960)

5.87 D. C. Bensahel, L. T. Canham, S. Ossicini. *Optical Properties of Low Dimensional Silicon Structures*, NATO ASI Series E: Applied Sciences **244** (1993)

5.88 S. S. Iyer, L. T. Canham, R. T. Collins: *Light Emission from Silicon*, Proceedings of the MRS Fall Meeting (Boston 1991)

5.89 A. G. Cullis: unpublished

5.90 A. Halimaoui: in *Optical Properties of Low Dimensional Silicon Structures*, ed. by D. C. Bensahel, L. T. Canham, S. Ossicini, (Kluwer Academic Publ., Dordrecht, Boston, London 1993), p. 11

5.91 J. Fricke (ed.): Journal of Non-Crystalline Solids **145** (1992)

5.92 M. Stutzmann, J. Weber, M. S. Brandt, H. D. Fuchs, M. Rosenbauer, P. Deak, A. Höpfner, A. Breitschwerdt: in *Festkörperprobleme/Advances in Solid State Physics* **32**, 179 (1992)

5.93 S. Frohnhoff: in *Berichte des Forschungszentrums Jülich* (Jül-2765), ISSN 0944-2952 (1993)

5.94 H. Münder, M. G. Berger, S. Frohnhoff, M. Thönissen, H. Lüth, W. Theiß, L. Küpper: in *Optical Properties of Low Dimensional Silicon Structures*, ed. by D. C. Bensahel, L. T. Canham, S. Ossicini, (Kluwer Academic Publ., Dordrecht, Boston, London 1993), p. 75

5.95 M. H. Berger, C. Dieker, M. Thönissen, L. Vescan, H. Lüth, H. Münder: J. Phys. D **27**, 1333 (1994)

5.96 K. H. Beckmann: Surf. Sci. **3**, 314 (1965)

5.97 T. Unagami: Jpn. J. Appl. Phys. **19**, 231 (1980)

5.98 Y. Kato, T. Ito, A. Hiraki: Jpn. J. Appl. Phys. **27**, 1406 (1988)

5.99 W. Theiß, P. Grosse, H. Münder, H. Lüth, R. Herino, M. Ligeon: Mat. Res. Soc. Symp. Proc. **238**, 215 (1993)

5.100 W. Theiß, P. Grosse, H. Münder, H. Lüth, R. Herino, M. Ligeon: Applied Surface Science **63**, 240 (1993)

5.101 W. Theiß, in *Festkörperprobleme/Advances in Solid State Physics* **33**, ed. by R. Helbig (Vieweg, Braunschweig, Wiesbaden 1994), p. 149

5.102 J. C. Maxwell Garnett: Philos. Trans. R. Soc. London **203**, 385 (1904)

5.103 D. A. G. Bruggeman: Ann. Phys. (Leipzig) **24**, 636 (1935)

5.104 D. J. Bergman: Phys. Rep. **C 43**, 377 (1978)

5.105 D. J. Bergman, D. Stroud: Solid State Phys., **46**, p. 147, eds. H. Ehrenreich and D. Turnbull (Academic Press, Boston 1992),

5.106 M. Evenschor, P. Grosse, W. Theiß: Vibrational Spectroscopy **1**, 173 (1990)

5.107 M. Hornfeck, R. Clasen, W. Theiß: J. Non-Cryst. Solids **145**, 154 (1992)

5.108 H. Münder, C. Andrzejak, M. G. Berger, U. Klemradt, H. Lüth, R. Herino, M. Ligeon: Thin Solid Films **221**, 27 (1992)

5.109 P. Grosse: Vibrational Spectroscopy **1**, 187 (1990)

6.1 A. Segmüller, M. Murakami in: Thin Films from Free Atoms and Particles,

6.2 B.M. Paine: MRS Symp. Proc. **69**, 39 (1986)

6.3 A. Segmüller, I.C. Noyan, V.S. Speriosu: Progr. Crystal Growth and Charact. **18**, 21 (1989)

6.4 A. Segmüller: J.Vac.Sci.Technol. **A9**, 2477 (1991)

6.5 C. Schiller, G. Martin, W.W. v.d. Hoogenhof, J. Corno: Philips J.Res. **47**, 217 (1993)

6.6 B.K. Tanner: Advances in X-Ray Analysis **33**, 1 (1990)

6.7 B.K. Tanner in: Analysis in Microelectronic Materials and Devices, ed. by M. Grasserbauer and H.W. Werner, (J. Wiley, New York), p. 609 (1991)

6.8 M.A.G. Halliwell: Prog. Crystal Growth and Charact. **19**, 249 (1989)

6.9 P.F. Fewster: J. Appl. Cryst. **24**, 178 (1991)

6.10 P.F. Fewster: Appl. Surf. Sci. **50**, 9 (1991)

6.11 P.F. Fewster: Semicond. Sci. Technol. **8**, 1915 (1993)

6.12 T. Picraux, B.L. Doyle, J.Y. Tsao in: Semiconductors and Semimetals, ed. by T.P. Pearsall, (Academic Press, N.Y.), p.139-220 (1991)

6.13 T.W. Ryan, M. Halliwell, S. Bates, I. Bassignana: Materials Research Society, Short Course on Characterisation of Compound Semiconductors by High Resolution X-Ray Diffraction 1990 and 1991

6.14 C.R. Wie: Materials Science and Engineering **R13**, No. 1, (1994)

6.15 E.J. Fantner, K. Lischka (eds.): Proc. High Resolution X-Ray Diffraction Workshop Aigen 1992, Appl. Phys. A **58**, No 3 (1994)

6.16 Proc. Int. Conf. on High Resolution X-Ray Diffraction and Topography, published in J. Phys. D (Appl. Phys.) **26**, No 4A (1993)
6.17 K. Kohra: J. Phys. Soc. Japan **30**, 1136 (1971)
6.18 R. Köhler: Appl. Phys. **A58**, 149 (1994)
6.19 C. Malgrange, D. Ferret: Nuclear Instruments and Methods in Physics Research **A314**, 285 (1992)
6.20 W. L. Bragg: Proc. Cambridge Phil. Soc. **17**, 43 (1913)
6.21 A. Segmüller: Advances in X-Ray Analysis **29**, 353 (1986)
6.22 M. Hart: J. Crystal Growth **55**, 409 (1981)
6.23 B. Davis, W. M. Stempel: Phys. Rev. **17**, 526 (1921)
6.24 W. Ehrenberg, H. Mark: Z. Physik **42**, 807 (1927)
6.25 J. W. M. DuMond: Phys. Rev. **52**, 872 (1937)
6.26 R. Bubakova in: Brümmer and Stephanik, loc. cit. [6.27], 148 (1976)
6.27 O. Brümmer, H. Stephanik (eds.): *Dynamische Interferenztheorie*, (Akad. Verlagsgesellschaft, Leipzig) 1976
6.28 A. Fingerland: in Brümmer and Stephanik, loc. cit. [6.27], 159 (1976)
6.29 K. J. Godwod: in Brümmer and Stephanik, loc. cit. [6.27], 165 (1976)
6.30 M. M. Schwarzschild: Phys. Rev. **32**, 162 (1928)
6.31 H. W. Schnopper: J. Appl. Phys. **36**, 1415 (1965)
6.32 J. H. Beaumont, M. Hart: J. Phys. **E7**, 823 (1974)
6.33 W. J. Bartels: J. Vac. Sci. Technol. **B1**, 338 (1983)
6.34 W. L. Bond: Acta Cryst. **13**, 814 (1960)
6.35 P. van der Sluis: J. Appl. Cryst. **27**, 50 (1994)
6.36 B. K. Tanner, D. K. Bowen: J. Cryst. Growth **126**,1 (1993)
6.37 M. Renninger: Z. Naturforschung **16a**, 1110 (1961)
6.38 K. Kohra: J. Phys. Soc. Japan **17**, 589 (1962)
6.39 M. Renninger: Z. Kristallogr. **99**, 181 (1938)
6.40 M. Renninger: Acta Cryst. **A24**, 143 (1968)
6.41 M. Lefeld-Sosnowska in: Brümmer and Stephanik, loc. cit. [6.27], 148 (1976)
6.42 T. W. Ryan, P. D. Hatton, S. Bates, M. Watt, C. M. Sotomayor Torres, P. A. Claxton, J. S. Roberts: Semicond. Sci. Technol. **2**, 241 (1987)
6.43 E. Koppensteiner, T. Ryan, M. Heuken, J. Söllner: J. Phys. D **26**, A35 (1993)
6.44 P. van der Sluis: J. Phys. D **26**, A188 (1993)
6.45 P. Zaumseil, U. Winter, F. Cembali, M. Servidori, Z. Sorek: Phys. Stat Sol. (a) **100**, 95 (1987)
6.46 R. Thompson, B. L. Doyle: Mat. Res. Proc. EA- **18**, 141 (1988)
6.47 A. McL. Mathieson: Acta Cryst. **A38**, 378 (1982)
6.48 R. L. Thompson, G. J. Collins, B. L. Doyle, J. A. Knapp: J. Appl. Phys. **70**, 4760 (1991)
6.49 T. Picraux T, B. L. Doyle, J. Y. Tsao: Mat. Sci. Technology **33**, 139 (1991)
6.50 N. Itoh, K. Okamoto: J. Appl. Phys. **63**, 1486 (1988)
6.51 M. Renninger: Z. Physik **106**, 141 (1937)
6.52 B. Post: J. Appl. Crystallogr. **8**, 452 (1975)
6.53 B. Post, P. P. Gong, L. Kern, J. Ladell: Acta Crystallogr. **A42**, 178 (1986)
6.54 B. Greenberg, J. Ladell: Appl. Phys. Lett. **50**, 436 (1987)
6.55 S. L. Morelhao, L. P. Cardoso, J. M. Sasaki, M. M. G. de Carvalho: J. Appl. Phys. **70**, 2589 (1991)

6.56 S. L. Morelhao, L. P. Cardoso: J. Appl. Phys. **73**, 4218 (1993)

6.57 Z. G. Pinsker: *Dynamical Scattering of X-Rays in Crystals*, Springer Verlag, Berlin Heidelberg New York 1978

6.58 P. F. Fewster: J. Appl. Cryst. **22**, 64 (1989)

6.59 P. F. Fewster: Electrochem. Soc. Symp. Proc. **89**-5, 278 (1989)

6.60 T. W. Ryan: Ph.D. Thesis, University of Edinburgh, 1986

6.61 C. G. Darwin C. G: Philos. Mag. **27**, 315 and 675 (1914)

6.62 P. P. Ewald: Ann. Physik **54**, 519 (1917)

6.63 M. von Laue: Ergebnisse d. exakt. Naturwiss. **10**, 133 (1931)

6.64 N. Kato, A. R. Lang: Acta Cryst. **12**, 787 (1959)

6.65 B. W. Batterman, G. Hildebrandt: Acta Cryst. **A24**, 150 (1968)

6.66 J. A. Prins: Zeit. f. Physik **63**, 477 (1930)

6.67 W. H. Zachariasen: *Theory of X-Ray Diffractions in Crystals*, (Wiley, New York 1945)

6.68 S. Takagi: Acta Cryst. **15**, 1311 (1962)

6.69 S. Takagi: J. Phys. Soc. Japan **26**, 1239 (1969)

6.70 D. Taupin: Bull. Soc. Fr. Mineral. Crystallogr. **87**, 469 (1964)

6.71 W. J. Bartels, J. Hornstra, D. J. W. Lobeek: Acta Cryst. **A42**, 539 (1986)

6.72 R. Zaus, M. Schuster, H. Göbel, J.-P. Reithmaier: Appl. Surf. Sci. **50**, 92 (1991)

6.73 M. Servidori, F. Cembali, R. Fabri, A. Zani: J. Appl. Cryst. **25**, 46 (1992)

6.74 M. O. Möller: Thesis, University of Würzburg, Germany

6.75 R. Zaus: J. Appl. Cryst. **26**, 801 (1993)

6.76 Y. C. Chen, P. K. Bhattacharya: J. Appl. Phys. **73**, 7389 (1993)

6.77 R. W. James: *The Optical Principles of the Diffraction of X-Rays, The Crystalline State-Vol* II, ed. by L. Bragg (G. Bell and Sons Ltd) (1962)

6.78 P. V. Petrashen: Sov. Phys. Sol. St. **16**, 1417 (1975)

6.79 P. V. Petrashen: Sov. Phys. Sol. St. **17**, 1882 (1976)

6.80 L. Tapfer, K. Ploog: Phys. Rev. **B33**, 5565 (1986)

6.81 L. Tapfer, K. Ploog: Phys. Rev. **B40**, 9802 (1989)

6.82 A. Segmüller, A. E. Blakeslee: J. Appl. Cryst. **6**, 19 (1973)

6.83 R. M. Fleming, D. B. Mc Whan, A. C. Gossard, W. Wiegemann, R. A. Logan: J. Appl. Phys. **51**, 357 (1980)

6.84 V. S. Speriosu, T. Vreeland Jr.: J. Appl. Phys. **56**, 1591 (1984)

6.85 V. S. Speriosu: J. Appl. Phys. **52**, 6094 (1981)

6.86 U. Lienert: Thesis, Technical University of Berlin 1989, unpublished

6.87 P. F. Fewster, C. J. Curling: J. Appl. Phys. **62**, 4154 (1987)

6.88 L. Tapfer, Phys. Scr.: **T25**, 6094 (1989)

6.89 H. Holloway: J. Appl. Phys. **67**, 6229 (1990)

6.90 C. R. Wie, H. M. Kim: J. Appl. Phys. **69**, 6406 and 6412 (1991)

6.91 A. T. Macrander, E. R. Minami, D. W. Berreman: J. Appl. Phys. **60**, 1364 (1986)

6.92 F. Abelès: Ann. de Physique **5**, 596 and 706 (1955)

6.93 L. Tapfer, M. Ospelt, H. von Känel: J. Appl. Phys. **67**, 1298 (1990)

6.94 D. M. Vardanyan, H. M. Manoukyan, H. M. Petrosyan: Acta Cryst. **A 41**, 212 and 218 (1985)

6.95 C. R. Wie: J. Appl. Phys. **65**, 1036 and 2267 (1989)

6.96 A. Caticha: Phys. Rev. **B49**, 33 (1994)

6.97 B. D. Cullity: *Elements of X-ray diffraction*, Addison-Wesley, Reading, Mass., (1956)

6.98 H. Meyerheim: Thesis, Ludwig-Maximilians University of Munich, 1985, unpublished

6.99 A. Segmüller, M. Murakami in: *Analytical Techniques for Thin Films*, ed. by K. N. Tu and R. Rosenberg, (Academic Press, New York 1988)

6.100 J. F. Nye: *Physical Properties of Crystals: Their Representation by Tensors and Matrices*, (Oxford 1957)

6.101 Y. Kawamura, H. Okamoto: J. Appl. Phys. **50**, 4457 (1979)

6.102 J. Hornstra, W. J. Bartels: J. Cryst. Growth **44**, 513 (1978)

6.103 B. Ortner: Advances in X-Ray Analysis **29**, 387 (1986)

6.104 E. Anastassakis: J. Appl. Phys. **68**, 4561 (1990)

6.105 M. Grundmann, U. Lienert, D. Bimberg, A. Fischer-Colbrie, J. N. Miller: Appl. Phys. Lett. **55**, 1765 (1989)

6.106 C. Giannini, L. De Caro, L. Tapfer: Solid State Commun. **91**, 635 (1994)

6.107 B. R. Bennett, J. A. del Alamo: J. Electron. Mater. **20**, 1075 (1991)

6.108 B. R. Bennett, J. A. del Alamo: Materials Research Society Proceedings (MRS, Pittsburgh, PA) **240**, 153 (1992)

6.109 W. J. Bartels, W. Nijman: J. Cryst. Growth **44**, 518 (1978)

6.110 J. W. Matthews in: *Epitaxial Growth B*, ed. by J. W. Matthews, Academic Press, New York 1975, p. 560

6.111 H. J. van der Merwe: J. Appl. Phys. **34**, 117 (1963)

6.112 H. J. van der Merwe, W. A. Jesser: J. Appl. Phys. **64**, 4968 (1988)

6.113 M. A. G. Halliwell, M. H. Lyons, M. J. Hill: J. Crystal Growth **68**, 523 (1984)

6.114 C. R. Wie, T. A. Tombrello, T. Vreeland: J. Appl. Phys. **59**, 3743 (1986)

6.115 B. M. Paine, V. S. Speriosu: J. Appl. Phys. **62**, 1704 (1987)

6.116 S. Bensoussan, C. Malgrange, M. Sauvage-Simkin: J. Appl. Cryst. **20**, 222 (1987)

6.117 H. Nagai: J. Appl. Phys. **43**, 4254 (1972)

6.118 H. Nagai: J. Appl. Phys. **45**, 3789 (1974)

6.119 P. Auvray, M. Baudet, A. Regreny: J. Cryst. Growth **95**, 228 (1989)

6.120 P. Auvray, A. Poudoulec, M. Baudet, B. Guenais, A. Regreny, C. d'Anterroches, J. Massies: Appl. Surf. Sci. **50**, 109 (1991)

6.121 D. A. Neumann, H. Zabel, H. Morkoc: J. Appl. Phys. **64**, 3024 (1988)

6.122 A. Pesek, K. Hingerl, F. Riesz, K. Lischka: Semicond. Sci. Technol. **6**, 705 (1991)

6.123 A. Pesek: Thesis, University of Linz, (1993)

6.124 A. Leiberich, J. Levkoff: Mat. Res. Symp. **159**, 101 (1990)

6.125 M. Quillec, L. Goldstein, G. LeRoux, J. Burgeat, J. Primot: J. Appl. Phys. **55**, 2904 (1984)

6.126 K. Nakashima: J. Appl. Phys. **71**, 1189 (1992)

6.127 P. van der Sluis: Appl. Phys. Lett. **62**, 1898 (1993)

6.128 E. Koppensteiner, G. Springholz, P. Hamberger, G. Bauer: J. Appl. Phys. **74**, 6062 (1993)

6.129 J. M. Vandenberg, M. B. Panish, H. Temkin, R. A. Hamm: Appl. Phys. Lett. **53**, 1920 (1988)

6.130 J. M. Vandenberg, A. T. Macrander, R. A. Hamm, M. B. Panish: Phys. Rev. **B44**, 3991 (1991)

6.131 R. Meyer, M. Hollfelder, H. Hardtdegen, B. Lengeler, H. Lüth: J. Cryst. Growth **124**, 583 (1992)

6.132 A. Krost, J. Böhrer, H. Roehle, G. Bauer: Appl. Phys. Lett. **64**, 469 (1994)

6.133 U. Rossow, A. Krost, T. Werninghaus, K. Schatke, W. Richter, A. Hase, H. Künzel, H. Roehle: Thin Solid Films, **233**, 180 (1993)

6.134 X. G. He, M. Erdtmann, R. Williams, S. Kim, M. Razeghi: Appl. Phys. Lett., **65**, 2812 (1994)

6.135 N. Herres, G. Bender, G. Neumann: Appl. Surf. Sci. **50**, 97 (1991)

6.136 A. Segmüller, P. Krishna, L. Esaki: J. Appl. Cryst. **10**, 1 (1977)

6.137 J. Kervarac, M. Baudet, J. Caulet, P. Auvray, Y. Y. Emery, A. Regreny: J. Appl. Cryst. **17**, 196 (1984)

6.138 A. Powell, R. Kubiak, E. Parker, K. Bowen, M. Polcarova: Mater. Res. Symp. Proc. Anaheim, 1991

6.139 D. B. McWhan in: *Synthetic Modulated Structures*, ed. by L. L. Chang and B. C. Giessen, (Academic Press, N. Y. 1985)

6.140 D. B. McWhan in: *Physics, Fabrication and Applications of Multilayered Structures*, ed. by P. Dhez and C. Weisbuch, (Plenum Press, N. Y.), p. 67 (1988)

6.141 D. K. Arch, J. P. Faurie, J.-L. Staudenmann, M. Hibbs-Brenner, P. Chow: J. Vac. Sci. Technology **A4**, 2101 (1986)

6.142 J. H. C. Hogg, D. Shaw, M. Staudte: Appl. Surf. Sci. **50**, 87 (1991)

6.143 H. Krenn, A. Holzinger, A. Voiticek, G. Bauer, H. Clemens: J. Appl. Phys. **72**, 97 (1992)

6.144 Y. Kim, A. Ourmazd, M. Bode, R. Feldman: Phys. Rev. Lett. **63**, 636 (1989)

6.145 P. F. Fewster: J. Appl. Cryst. **21**, 524 (1988)

6.146 D. E. Savage, J. Kleiner, N. Schimke, Y.-H. Phang, T. Jankowski, J. Jacobs, R. Kariotis, M. G. Lagally: J. Appl. Phys. **69**, 1411 (1991)

6.147 Y. H. Phang, D. E. Savage, T. F. Kuech, M. G. Lagally, J. S. Park, K. L. Wang: Appl. Phys. Lett **60**, 2986 (1992)

6.148 V. Holý, J. Kubena, I. Ohlidal, K. Ploog: Superlattices and Microstructures **12**, 25 (1992)

6.149 P. F. Fewster: Philips J. Res. **41**, 268 (1986)

6.150 W. J. Bartels in: *Thin Film Growth Techniques for Low-Dimensional Structures*, ed by R. F. C. Farrow et al., Nato ASI Series **163**, Plenum Press, (1987), p. 441

6.151 S. J. Barnett, G. T. Brown, D. C. Houghton, J. M. Baribeau: Appl. Phys. Lett **54**, 1781 (1989)

6.152 L. Hart, M. R. Fahy, R. C. Newman, P. F. Fewster: Appl. Phys. Lett. **62**, 2218 (1993)

6.153 M. A. Hollanders, B. J. Thijsse: J. Appl. Phys. **70**, 1270 (1991)

6.154 E. E. Fullerton, I. K. Schuller, H. Vanderstraeten, Y. Bruynserade: Phys. Rev. **B45**, 9292 (1992)

6.155 P. van der Sluis: Philips J. Research **47**, 203 (1993)

6.156 V. Holý, J. Kubena: Phys. Stat. Sol. (b) **170**, 9 (1992)

6.157 V. Holý, J. Kubena, E. Abramof, K. Lischka, A. Pesek, E. Koppensteiner: J. Appl. Phys. **74**, 1736 (1993)

6.158 P. F. Fewster: J. Appl. Cryst. **25**, 714 (1992)

6.159 P. Ofner, H. Krenn, S. Bates, R. A. Cowley, H. Clemens, G. Bauer: *Proc. Int. Conf. Phys. Semicond. Warszawa* (Polish Academy of Sciences Warszawa 1988), p. 483

6.160 A. M. Keir, S. J. Barnett, J. Fiess, T. D. Walsh, M. G. Astles: Appl. Surf. Sci. **50** 103 (1991)

6.161 E. Koppensteiner, P. Hamberger, G. Bauer, A. Pesek, H. Kibbel, H. Presting, E. Kasper: Appl. Phys. Lett. **62**, 1783 (1993)

6.162 E. Koppensteiner, G. Bauer, H. Kibbel, E. Kasper: J. Appl. Phys. **76**, 3489 (1994)

6.163 E. Koppensteiner, P. Hamberger, G. Bauer, V. Holý, E. Kasper: Appl. Phys. Lett. **64**, 172 (1994)

6.164 H. Heinke, M. O. Möller, D. Hommel, G. Landwehr: J. Crystal Growth **135**, 41 (1994)

6.165 G. Bauer, E. Koppensteiner, P. Hamberger, J. Nützel, G. Abstreiter, H. Kibbel, H. Presting, E. Kasper: Acta Physica Polonica A **84**, 475 (1993)

6.166 A. T. Macrander, S. E. G. Slusky: Appl. Phys. Lett. **56**, 443 (1990)

6.167 A. T. Macrander, S. Lau, K. Strege, S. N. G. Chu: Appl. Phys. Lett. **52**, 1985 (1988)

6.168 V. Holý: Appl. Phys. **A58**, 173 (1994)

6.169 L. Tapfer, P. Grambow: Appl. Phys. **A50**, 3 (1990)

6.170 L. Tapfer, G. C. LaRocca, H. Lage, O. Brandt, D. Heitmann, K. Ploog: Appl. Surf. Sci. **60/61**, 517 (1992)

6.171 R. Cingolani, H. Lage, L. Tapfer, H. Kalt, D. Heitmann, K. Ploog: Phys. Rev. Lett. **67**, 891 (1991)

6.172 L. De Caro, P. Sciacovelli, L. Tapfer: Appl. Phys. Lett. **64**, 34 (1994)

6.173 M. Gailhanou, T. Baumbach, U. Marti, P. C. Silva, F. K. Reinhart, M. Ilegems: Appl. Phys. Lett. **62**, 1623 (1993)

6.174 P. van der Sluis, J. J. M. Binnsma, T. van Dongen: Appl. Phys. Lett. **62**, 3186 (1993)

6.175 V. Holý, L. Tapfer, E. Koppensteiner, G. Bauer, H. Lage, O. Brandt, K. Ploog: Appl. Phys. Lett. **63**, 3140 (1993)

6.176 T. Fukui, H. Saito: Appl. Phys. Lett. **50**, 824 (1987)

6.177 O. Brandt, L. Tapfer, K. Ploog, R. Bierwolf, M. Hohenstein, F. Phillip, H. Lage, A. Heberle: Phys. Rev. **B44**, 8043 (1991)

6.178 A. A. Darhuber, E. Koppensteiner, G. Bauer, P. D. Wang, Y.P. Song, C.M. Sotomayor Torres, M.C. Holland: Appl. Phys. Lett. **66**, No. 8, 20 February 1995

6.179 I. K. Schuller, M. Grimsditch, F. Chambers, G. Devane, H. Vanderstraeten, D. Neerinck, J. P. Locquet, Y. Bruynseraede: Phys. Rev. Lett. **65**, 1235 (1990)

6.180 P. F. Miceli in: *Semiconductor Interfaces, Microstructures and Devices: Properties and Applications*, ed. by Z. C. Feng (Adam Hilger IOP Publishing Ltd, Bristol 1992), p. 87

6.181 J. M. Baribeau: J. Appl. Phys. **72**, 4452 (1992)

6.182 S. K. Sinha, E. B. Sirota, S. Garoff, H. B. Stanley: Phys. Rev. **B38**, 2297 (1988)

6.183 S. Yasuami, K. Ohshima, S. Sasaki, M. Ando: J. Appl. Cryst. **25**, 514 (1992)

6.184 J. M. Cowley: J. Appl. Phys. **21**, 24 (1950)

6.185 T. Tsuchiya, T. Taniwatari, K. Uomi, T. Kawano, Y. Ono: *Proc. 4th InP and Related Materials Conference*, Newport, Rhode Island (1992)

6.186 W. Lowe, R. A. MacHarrie, J. C. Bean, L. Peticolas, R. Clarke, W. Dos Passos, C. Brizard, B. Rodricks: Phys. Rev. Lett. **67**, 2513 (1991)

6.187 R. Feidenhans'l: Surf. Sci. Rep. **10**, 105 (1989)

6.188 P. H. Fuoss, S. Brennan: Ann. Rev. Mater. Sci. **20**, 365 (1990)

6.189 I. K. Robinson, D. J. Tweet: Reports on Progress in Phys. **55**, 599 (1992)

6.190 M. Bienfait, J. M. Gay (eds.): *X-Ray and Neutron Scattering from Surfaces and Thin Films*, Colloque de Physique **C7**, Supp. 10, Tome 50, Marseille, France 1989

6.191 H. Zabel, J. K. Robinson (eds.): *Surface X-Ray and Neutron Scattering*, Springer Proceedings in Physics, Vol. **61**, (Springer, Berlin, Heidelberg, New York 1991)

6.192 H. Zabel: Appl. Phys. **A58**, 159 (1994)

6.193 M. Born, E. Wolf: *Principles of Optics* (Pergamon Press, Third Ed.) 1965

6.194 A. H. Compton, S. K. Allison: *X-Rays in Theorie and Experiment*, D. van Nostrand Company, Inc. Princeton, New Jersey, Second Edition, 674 (1935)

6.195 D. T. Cromer, D. Liberman: J. Chem. Phys. **53**, 1891 (1970)

6.196 W. J. Veigele in: *Handbook of Spectroscopy*, Vol. 1, ed. by J. W. Robinson (CRC Press, Cleveland, Ohio 1974)

6.197 A. H. Compton: Philos. Mag. **2**, 897 (1923)

6.198 B. Lengeler in: *Synchrotronstrahlung in der Festkörperphysik*, 18. IFF Ferienkurs, March 16-27, Jülich (1987)

6.199 L. G. Parrat: Phys. Rev. **95**, 359 (1954)

6.200 G. H. Vineyard: Phys. Rev. **B26**, 4146 (1982)

6.201 J. A. Prins: Z. Physik **47**, 4791 (1928)

6.202 H. Kiessig: Ann. Phys. **10**, 715 (1931)

6.203 F. Stanglmeier: Report JÜL-2346, Januar 1990, ISSN 0366-0885

6.204 H. Kiessig: Ann. Phys. **10**, 769 (1931)

6.205 D. G. Stearns: J. Appl. Phys. **71**, 4286 (1992)

6.206 W. Weber, B. Lengeler: Phys. Rev. **B46**, 7953 (1992)

6.207 V. Holý, J. Kubena, I. Ohlodal, K. Lischka, W. Plotz: Phys. Rev. **B47**, 15896 (1993)

6.208 B. Vidal, P. Vincent: Appl. Optics **23**, 1794 (1984)

6.209 Y. Yoneda: Phys. Rev. **131**, 2010 (1963)

6.210 B. E. Warren, J. S. Clarke: J. Appl. Phys. **36**, 324 (1965)

6.211 O. J. Guentert: Phys. Rev. **138**, A732 (1965)

6.212 D. E. Savage, N. Schimke, Y.-H. Phang, M. G. Lagally: J. Appl. Phys. **71**, 3283 (1992)

6.213 Y.-H. Phang, R. Cariotis, D. E. Savage, M. G. Lagally, J. Appl. Phys. **72**, 4627 (1992)

6.214 D. Bar, W. Press, R. Jebasinski, S. Mantel: Phys. Rev. **B47**, 4385 (1993)

6.215 V. Holý, T. Baumbach: Phys. Rev. **B49**, 10668 (1994)

6.216 L. L. Chang, A. Segmüller, L. Esaki: Appl. Phys. Lett. **28**, 39 (1976)

6.217 A. R. Powell, J. Bradler, C. R. Thomas, R. A. Kubiak, K. D. Bowen, M. Wormington, J. M. Hudson: Mater. Res. Symp. Proc. (Boston), 1991

6.218 W. Spirkl: J. Appl. Phys. **74**, 1776 (1993)

6.219 K. Sakurai, A. Iida: Jpn. J. Appl. Phys. **31**, L113 (1992)
6.220 A. Król, H. Resat H, C. J. Sher, S. C. Woronick, W. Ng, Y. H. Kao, T. L. Cole, A. K. Green, W. Lowe-Ma, V. Rehn: J. Appl. Phys. **69**, 949 (1990)
6.221 W. F. J. Slijkerman, J. M. Gay, P. M. Zagwijn, J. F. van der Veen, J. E. Macdonald, A. A. Williams, D. J. Gravesteijn, G. F. A. van de Walle: J. Appl. Phys. **68**, 5105 (1990)
6.222 J. M. Baribeau: Appl. Phys. Lett. **57**, 1748 (1990)
6.223 J. M. Baribeau: J. Appl. Phys. **70**, 5710 (1991)
6.224 P. F. Miceli, D. A. Neumann, H. Zabel: Appl. Phys. Lett. **48**, 24 (1986)
6.225 M. Pomerantz: Thin Solid Films **152**, 165 (1987)
6.226 A. Braslau, P. S. Pershan, G. Swislow, B. M. Ocko, J. Als-Nielsen: Phys. Rev. **A38**, 2457 (1988)
6.227 J. J. Benattar, J. Daillant, L. Bosio, L. Leger: Colloque de Physique **C7**, Tome 50, Suppl. 10, ed. by M. Bienfait, J. M. Gay, Marseille, France (1989)
6.228 A. Król, C. J. Sher, Y. H. Kao: Phys. Rev. **B38**, 8579 (1988)
6.229 U. Weisbrod, R. Gutschke, J. Knoth, H. Schwenke: Appl. Phys. **A53**, 449 (1991)
6.230 W. C. Marra, P. Eisenberger, A. Y. Cho: J. Appl. Phys. **50**, 6927 (1979)
6.231 P. Farwig, H. W. Schürmann: Z. Physik **204**, 489 (1967)
6.232 S. Dietrich, H. Wagner: Phys. Rev. Lett. **51**, 1469 (1983)
6.233 S. Dietrich, H. Wagner: Z. Phys. B -Condensed Matter **56**, 207 (1984)
6.234 A. M. Afanas'ev, M. K. Melkonyan: Acta. Cryst. **A39**, 207 (1983)
6.235 P. L. Cowan: Phys. Rev. **B32**, 5437 (1985)
6.236 H. Zabel: in *Festkörperprobleme XXX - Advances in Solid State* Physics, ed. by U. Rössler (Vieweg Braunschweig, Wiesbaden 1990), p. 197
6.237 H. Dosch: *Critical Phenomena at Surfaces and Interfaces, Springer Tracts in Modern Physics*, **126**, (Springer, Berlin, Heidelberg, New York 1992)
6.238 H. Dosch, B. W. Batterman, D. C. Wack: Phys. Rev. Lett. **56**, 1144 (1986)
6.239 H. Dosch: Phys. Rev. **B35**, 2137 (1987)
6.240 R. S. Becker, J. A. Golovchenko, J. R. Patel: Phys. Rev. Lett. **50**, 153 (1983)
6.241 N. Bernhard N, E. Burkel, G. Gompper, H. Metzger, J. Peisl, H. Wagner, G. Wallner: Z. Phys. B - Condensed Matter **69**, 3031 (1987)
6.242 T. Jach, P. L. Cowan, Q. Shen, M. J. Bedzyk: Phys. Rev. **B39**, 5739 (1989)
6.243 P. A. Aleksandrov, A. M. Afanasiev, M. K. Melkonyan, S. A. Stepanov: Phys. Stat. Sol.(a) **81**, 47 (1984)
6.244 S. A. Stepanov: Phys. Stat. Sol. (a) **126**, K15 (1991)
6.245 A. L. Golovin, R. M. Imamov: Phys. Stat. Sol. (a) **77**, K91 (1983)
6.246 H. Rhan, U. Pietsch: Phys. Stat. Sol. (a) **107**, K93 (1988)
6.247 H. Rhan, U. Pietsch: Z. Phys. B - Condensed Matter **80**, 347 (1990)
6.248 H. Munekata, A. Segmüller, L. L. Chang: Appl. Phys. Lett. **51**, 587 (1987)
6.249 P. H. Fuoss, D. W. Kisker, S. Brennan, J. L. Kahn, G. Renaud, K. L. Tokuda in: *Heteroepitaxial Approaches in Semiconductors - Lattice Mismatch and its Consequences*, ed. by A. T. Macrander and T. J. Drummond, p. 159 (The Electrochemical Society, Pennington NJ) (1989)
6.250 D. W Kisker, P. H. Fuoss, S. Brennan, G. Renaud, K. L. Tokuda, J. L. Kahn: J. Cryst. Growth **101**, 42 (1990)
6.251 D. W Kisker, G. B. Stephenson, P. H. Fuoss, F. J. Lamelas, S. Brennan, P. Imperatori: J. Cryst. Growth **124**, 1 (1992)

6.252 F. J. Lamelas, P. H. Fuoss, D. W. Kisker, G. B. Stephenson, P. Imperatori, S. Brennan: Phys. Rev. **B49**, 1957 (1994)

Subject Index

Ergebnisse der Mathematik und ihrer Grenzgebiete, 3. Folge

A Series of Modern Surveys in Mathematics

Volume 1: **A. Fröhlich**

Galois Module Structure of Algebraic Integers

1983. X, 262 pp. ISBN 3-540-11920-5

Volume 2: **W. Fulton**

Intersection Theory

1984. XI, 470 pp. ISBN 3-540-12176-5

Volume 3: **J. C. Jantzen**

Einhüllende Algebren halbeinfacher Lie-Algebren

1983. V, 298 pp. ISBN 3-540-12178-1

Volume 4: **W. Barth, C. Peters. A van de Ven**

Compact Complex Surfaces

1984. X, 304 pp. ISBN 3-540-12172-2

Volume 5: **K. Strebel**

Quadratic Differentials

1984. XII, 184 pp. 74 figs. ISBN 3-540-13035-7

Volume 6: **M. J. Beeson**

Foundations of Constructive Mathematics

Metamathematical Studies

1985. XXIII, 466 pp. ISBN 3-540-12173-0

Volume 8: **R. Mañé**

Ergodic Theory and Differentiable Dynamics

Translated from the Portuguese by Silvio Levy

1987. XII, 317 pp. 32 figs. ISBN 3-540-15278-4

Volume 9: **M. Gromov**

Partial Differential Relations

1986. IX, 363 pp. ISBN 3-540-12177-4

Volume 10: **A. L. Besse**

Einstein Manifolds

1986. XII, 510 pp. 22 figs. ISBN 3-540-15279-2

Volume 11: **M. D. Fried, M. Jarden**

Field Arithmetic

1986. XVII, 458 pp. ISBN 3-540-16640-8

Volume 12: **J. Bochnak, M. Coste, M.-F. Roy**

Géométrie algébrique réelle

1987. X, 373 pp. 44 figs. ISBN 3-540-16951-2

Volume 13: **E. Freitag, R. Kiehl**

Etale Cohomology and the Weil Conjecture

With an Historical Introduction by J. A. Dieudonné

1987. XVIII, 317 pp. ISBN 3-540-12175-7

Volume 14: **M. R. Goresky, R. D. MacPherson**

Stratified Morse Theory

1988. XIV, 272 pp. 84 figs. ISBN 3-540-17300-5

Volume 15: **T. Oda**

Convex Bodies and Algebraic Geometry

An Introduction to the Theory of Toric Varieties

1987. VIII, 212 pp. 42 figs. ISBN 3-540-17600-4

Volume 16: **G. van der Geer**

Hilbert Modular Surfaces

1988. IX, 291 pp. ISBN 3-540-17601-2

Springer

Springer-Verlag, Postfach 31 13 40, D-10643 Berlin, Fax 0 30 / 82 07 - 3 01 / 4 48, e-mail: orders@springer.de BA95.10.18

Ergebnisse der Mathematik und ihrer Grenzgebiete, 3. Folge

A Series of Modern Surveys in Mathematics

Ed.-in-chief: **R. Remmert.** Eds.: **E. Bombieri, S. Feferman, M. Gromov, H. W. Lenstra, P-L. Lions, W. Schmid, J-P. Serre, J. Tits**

Volume 17: **G. A. Margulis**

Discrete Subgroups of Semisimple Lie Groups

1990. IX, 388 pp. ISBN 3-540-12179-X

Volume 18: **A. E. Brouwer, A. M. Cohen, A. Neumaier**

Distance-Regular Graphs

1989. XVII, 495 pp. ISBN 3-540-50619-5

Volume 19: **I. Ekeland**

Convexity Methods in Hamiltonian Mechanics

1990. X, 247 pp. 4 figs. ISBN 3-540-50613-6

Volume 20: **A. I. Kostrikin**

Around Burnside

1990. XII, 255 pp. ISBN 3-540-50602-0

Volume 21: **S. Bosch, W. Lütkebohmert, M. Raynaud**

Néron Models

1990. X, 325 pp. 4 figs. ISBN 3-540-11920-5

Volume 22: **G. Faltings, C.-L. Chai**

Degeneration of Abelian Varieties

1990. XII, 316 pp. ISBN 3-540-52015-5

Volume 23: **M. Ledoux, M. Talagrand**

Probability in Banach Spaces

Isoperimetry and Processes

1991. XII, 480 pp. 1 fig. ISBN 3-540-52013-9

Volume 24: **V. F. Lazutkin**

KAM Theory and Semiclassical Approximations to Eigenfunctions

Appendix by A. I. Shnirelman

1993. IX, 387 pp. 66 figs. ISBN 3-540-53389-3

Volume 25: **W. de Melo, S. van Strien**

One-Dimensional Dynamics

1993. XIII, 605 pp. 89 figs. ISBN 3-540-11920-5

Volume 26: **S. Rickman**

Quasiregular Mappings

1993. X, 213 pp. 5 figs. ISBN 3-540-11920-5

Volume 27: **R. Friedman, J. W. Morgan**

Smooth Four-Manifolds and Complex Surfaces

1994. X, 520 pp. 17 figs. ISBN 3-540-11920-5

Volume 28: **V. Havin, B. Jöricke**

The Uncertainty Principle in Harmonic Analysis

1994. XII, 543 pp. ISBN 3-540-56991-X

Volume 29: **A. Joseph**

Quantum Groups and Their Primitive Ideals

1995. X, 383 pp. ISBN 3-540-57057-8

Volume 30: **E. Viehweg**

Quasi-projective Moduli for Polarized Manifolds

1995. VI, 320 pp. ISBN 3-540-59255-5

Springer

Springer-Verlag, Postfach 31 13 40, D-10643 Berlin, Fax 0 30 / 82 07 - 3 01 / 4 48, e-mail: orders@springer.de BA95.10.18